

Curso 2009/10
CIENCIAS Y TECNOLOGÍAS/39
I.S.B.N.: 978-84-7756-985-5

VALERIA BUENROSTRO-LEITER

**The Evolution of Disk Galaxies:
Nature or Nurture?**

Directores

**JOHN E. BECKMAN ABRAMSON
EMILIO CASUSO ROMATE**



SOPORTES AUDIOVISUALES E INFORMÁTICOS
Serie Tesis Doctorales

Agradecimientos

Primero que nada, quiero agradecer a mis padres, Waltraud y Marco, por todo el apoyo que me han dado, por creer en mí y alimentar mi curiosidad por el Universo desde pequeña. Es gracias a ustedes que estoy aquí y les estoy eternamente agradecida.

Por supuesto, el mérito es más que compartido con mi asesor, John Beckman, quien supo guiar mi tesis de manera extraordinaria. Pero además ha sido un gran amigo para mí, alguien que me ha apoyado en momentos sumamente difíciles. John, eres un ser humano maravilloso, y un excelente astrónomo, que más puede pedir una doctoranda :) De la misma manera quiero agradecer a Emilio Casuso por haber coasesorado esta tesis y por haberme apoyado a lo largo de ella.

Gran parte de mi tesis se ha llevado a cabo con el apoyo de quienes yo llamo mis coasesores. Aunque no figuren oficialmente, de alguna manera lo son. Elias Brinks, otro ser humano maravilloso y excelente astrónomo, gracias por todo lo que me has enseñado, no tengo palabras para agradecerte todo el conocimiento que he adquirido gracias a tí. Miguel de Avillez, muito obrigada por tudo! Pela sua paciência e por compartilhar sua sabedoria! Tenho saudades daqueles dias quentes em Évora. Jay Lockman, another amazing astronomer who has guided me in this marvelous trip through the astronomical world, in such a beautiful place as it is Green Bank. Thank you so much!

Quiero dar un agradecimiento muy especial a Maurizio, quien me ha acompañaado en vida y en muerte durante mis arduos días de trabajo. Este mérito también es tuyo Mau, no sabes cuánto te extraño. Y por supuesto, otro agradecimiento sin palabras a Patrizia, que me ha apoyado tanto, que siempre ha estado ahí para mí y la persona a la que le debo el haberme alimentado durante los últimos días del desarrollo de esta tesis cuando no tenía tiempo ni para cocinar. A mia madre italiana, grazie mille per tutto :)

Quiero agradecer a todos mis amigos por tantísimos buenos momentos que hemos pasado compartiendo este camino de la astronomía, Carlos, Kerttu, Nieves, Carmen, Ruth, Nayra, Luis, Alex, Mirjana, Ingrid, uff son tantos que seguro me olvido de nombres, pero todos están en mi corazón.

Leonel Gutiérrez, no sé cómo has logrado tener tiempo de terminar tu tesis y ayudarme con la mía, muchísimas gracias! Ha sido maravilloso compartir este viaje contigo.

Miguel A. Yañez, me has apoyado tanto que no sé como agradecerte todo, incluyendo las largas horas de trabajo, tu paciencia y empeño en que entendiera los conceptos necesarios. Tienes un lugar muy especial en mi corazón. Cuánto me alegro de que hayas aparecido en mi vida.

David, otra persona especial en mi vida a la que le debo tantas cosas. Gracias por existir y gracias por todo el apoyo que me diste.

Chucho, siempre creíste en mí, gracias por ayudarme a mudarme a esta isla tan maravillosa y por transmitirme tu confianza constante en mí.

Otra persona a la que quiero darle mi más sincero agradecimiento es a Johan Knapen, por haber hecho de mi asesor cuando John no podía. Tus comentarios han sido maravillosos para el mejoramiento de esta tesis, te estoy muy agradecida por ello.

Otro agradecimiento especial se lo quiero dar a Anders, quien me ha dado un empujoncito cuando lo necesitaba para poder sacar este trabajo adelante. Tack så mycket min kärlek!

Nahui, Damiana, Balam, Sifaw, Schatzy e Iziri, gracias por brindarme momentos de tranquilidad en los tiempos más estresantes y ronronearme hasta que quedara dormida. No sé que hubiera hecho sin ustedes.

Quiero agradecer al Instituto de Astrofísica de Canarias por haberme dado la oportunidad de realizar uno de mis sueños en tan maravillosas instalaciones y con investigadores de tan alta profesionalidad.

Un último agradecimiento a todas aquellas personas que de alguna manera u otra han ayudado en la realización de esta tesis, muchísimas gracias.

Index

0.1	Acreción de Gas en Galaxias de Disco	vi
0.2	El Complejo H, una HVC en la Vía Láctea	vii
0.3	HVCs en THINGS	viii
0.4	Modelo Teórico del Impacto de una HVC con el Disco Galáctico	viii
0.5	Conclusiones	ix
0.6	Trabajo Futuro	xi
1	Introduction	1
1.1	Gas Accretion In Galaxy Disks	1
1.1.1	Continuous Gas Infall Into the Disk	2
1.1.2	Dynamics	2
1.1.3	Summary: Importance Of Gas Accretion	5
1.2	What are HVCs?	6
1.2.1	Distances and Abundancies	6
1.2.2	Possible Origins	7
1.3	Objectives and organization of this work	8
2	Complex H, A High velocity Cloud in the Milky Way	11
2.1	Introduction	11
2.2	Observations	12
2.3	Data Reduction	13
2.4	The Observed Properties of the Complex	13
2.4.1	Distance and Orbit	13
2.4.2	Size and Mass	17
2.4.3	Moment Maps	18
2.5	Discussion and Conclusions	27
3	HVCs in THINGS	31
3.1	Introduction	31
3.2	Search For HVCs In THINGS	32
3.2.1	Observations	32
3.2.2	Detectability of HVCs	35
3.3	Results	38
3.3.1	HVC candidates	38

3.3.2	Mass estimate	38
3.4	Discussion	46
3.4.1	HVCs in and outside our Galaxy	46
3.4.2	Can we detect Galactic HVC Complex C in THINGS?	46
3.4.3	Expected and actual HVC detections in the THINGS galaxies	48
4	Theoretical Modelling of the Impact of HVCs with the Galactic Disk	51
4.1	Introduction	51
4.2	A Review of Numerical Simulations of HVCs	52
4.2.1	Hydrodynamical Simulations	52
4.2.2	Magnetohydrodynamical Simulations	53
4.2.3	Smooth Particle Hydrodynamics Tree Codes	56
4.2.4	Summary	57
4.3	Dynamics of an infalling HVC	57
4.4	Triggering of Cloud Collapse in a Galactic Disk by Infall of a High-Velocity Cloud	67
4.4.1	Infinite thickness and uniform rotation	67
4.4.2	Shearing Box and Infinite Thickness	68
4.4.3	Infinite thickness and a shearing box with magnetic field	77
4.4.4	Conclusions	80
5	Summary and Conclusions	83
A	Calculation of HI masses	89
B	Python Boxcar	93
C	Perpendicular Acceleration	103
D	Small Perturbations Analysis For An Infinite Thick Disk With Uniform Rotation	105
E	Small Perturbations Analysis For A Thick Disk With Magnetic Fields	107
F	Bibliography	111

Resumen

0.1 Acreción de Gas en Galaxias de Disco

La acreción de gas en discos galácticos es un fenómeno físico necesario en las teorías de formación galáctica, ya que de acuerdo a las teorías cosmológicas o modelos de materia oscura fría (CDM), el escenario de formación galáctica característico es el jerárquico (Navarro, Frenk & White 1995).

Hay varios procesos dinámicos en las galaxias que pueden ser explicados de manera natural si tomamos en cuenta la acreción de gas externo. Grandes cantidades significativas de gas pueden ser acretadas en el tiempo de vida de una galaxia, y es posible que la masa de una galaxia se duplique en unos Gyrs. La presencia de alabeos gaseosos en prácticamente cada galaxia espiral ha sido interpretada como señal de que una galaxia espiral acreta material y momento angular, al mismo tiempo que puede invertir su evolución y experimentar varios episodios de barras nuevas mientras que también logra mantener su onda de densidad espiral. De la misma forma, se ha visto que la tasa de formación estelar en la galaxia se ha mantenido constante y hasta muestra un pequeño incremento en el tiempo de escala del disco. Esto puede ser entendido si añadimos material gaseoso acretado al disco desde el exterior. Son varios los procesos dinámicos que son explicados en este escenario, por lo que nos parece importante estudiar el efecto de la caída de gas en el disco Galáctico, en nuestro caso el efecto específico de nubes de alta velocidad y su posible impacto en la formación estelar en el disco gaseoso.

Las nubes de alta velocidad (HVCs por sus siglas en inglés) son candidatos por excelencia de una fracción significativa de material que llena el espacio intergaláctico y que según algunos autores (Blitz et al. 1999; Braun & Burton 1999; López -Corredoira et al. 1999; Wakker et al. 1999), es acretado por las galaxias del Grupo Local. Podrían ser las nubes remanentes de la formación Galáctica, ya que su metalicidad y distribución de densidad columnar son muy parecidos a los del bosque de Lyman alfa por un lado, y por otro, si pensamos que la tasa de caída de gas de baja metalicidad en el disco es constante durante su tiempo de vida, entonces por lo menos la mitad de la masa del Grupo Local debe consistir en nubes de alta velocidad. De la misma manera, las nubes de alta velocidad pueden explicar la evolución de los elementos ligeros en la Galaxia y el problema de las enanas G y K. Además, las estimaciones de la tasa de masa que llega al disco gracias a las HVCs son consistentes con las estimaciones de las tasas continuas de formación estelar.

Las HVCs fueron descubiertas por primera vez por Muller et al. (1963). Son nubes compuestas principalmente por hidrógeno neutro moviéndose a altas velocidades excediendo los 90 km s^{-1} en dirección de o en sentido contrario del sistema local de referencia (LSR por sus siglas en inglés), y se desvían de la velocidad de rotación del disco hasta en unos 300 km s^{-1} . Por lo tanto, estas nubes de gas deben de estar moviéndose de manera independiente del disco, y sus velocidades no pueden ser explicadas por modelos de rotación Galáctica simples (Wakker 1991). No muestran una contraparte óptica y su naturaleza ha permanecido controversial.

Su emisión se observa principalmente en la longitud de onda de 21 cm, aunque también han sido estudiadas en emisiones y absorciones en $\text{H}\alpha$. Exhiben una gran variedad en tamaño, morfología y velocidad, con los más grandes complejos ocupando varios grados en

el cielo, y los más pequeños, o nubes de alta velocidad compactos (CHVCs por sus siglas en Inglés), ocupando pequeñas extensiones angulares ($\sim 2^\circ$).

Sus densidades columnares, velocidades y metalicidades son asequibles. Sin embargo, las distancias son difíciles de determinar para nubes compuestas principalmente de hidrógeno neutro. Esto es un problema, ya que muchos parámetros fundamentales de la nube, como su tamaño y densidad, requieren que se conozca la distancia. Además, la distancia y distribución de masa de estas nubes son elementos fundamentales para poder conocer su formación.

Las HVCs forman parte del gas extraplanar en nuestra Galaxia, por lo que el estudio de su origen y dinámica nos pueden ayudar a entender mejor la formación y estructura de las galaxias espirales en el Universo.

0.2 El Complejo H, una HVC en la Vía Láctea

Nuevas observaciones del Complejo H, una conocida HVC en nuestra Galaxia, fueron hechas durante los años 2003-2004, y nuevamente en 2008-2009. Estas observaciones fueron reducidas y analizadas, y han producido las observaciones de resolución en HI más altas jamás tomadas del Complejo H. Calculamos la velocidad del complejo proyectada al LSR en términos de ϕ , el ángulo de la órbita, la cual se incrementa en una órbita retrógrada alrededor de la Galaxia, y de i , el ángulo de inclinación de la órbita con respecto al plano Galáctico. Actualmente ϕ es igual a cero ya que el complejo se encuentra cruzando el plano Galáctico, e $i = 50^\circ$.

Encontramos que la masa del complejo tiene una magnitud mayor que la masa encontrada en estudios previos, con $M_{\text{HI}} = 4.6 \times 10^7 M_\odot$. Esto se debe a que las nuevas observaciones tienen una resolución angular que nos ha permitido separar claramente el gas que compone la HVC de el gas del disco, y esto nos ha permitido incluir más gas del complejo en el análisis, gas que pertenece específicamente a la cola del complejo.

Con las nuevas observaciones y cálculos realizados en este trabajo hemos confirmado que el Complejo H se mueve a una velocidad promedio de -200 km s^{-1} en dirección sureste, pero con un ángulo de inclinación hacia nosotros, dejando atrás grandes cantidades de gas a medida que interacciona con el gas del disco de la Vía Láctea. La parte frontal, o la cabeza de la nube, está sufriendo una desaceleración a medida que cruza el disco Galáctico, y este proceso está dejando zonas de turbulencia a lo largo de la nube, en las zonas más densas y en la cola. Las nuevas observaciones también muestran que justo detrás del cuerpo principal del complejo parece haber una cola más. También muestran puentes cinemáticos entre la nube y la emisión Galáctica que no han sido observados antes, y que probablemente son material arrancado de la nube o de la misma Vía Láctea debido a la interacción. Interpretamos esto como evidencia de que está habiendo una interacción entre el complejo y el halo Galáctico. Además, la parte externa de la Vía Láctea parece estar siendo perturbada por la interacción. Esto nos sugiere que el Complejo H se desplomó en las partes externas de nuestra Galaxia y aceleró material previamente presente, por lo que los puentes cinemáticos observados pertenecen probablemente a gas Galáctico.

0.3 HVCs en THINGS

Buscamos análogos de las HVCs de nuestra Galaxia en otras galaxias, específicamente en el estudio llamado THINGS, con el que se mapeó 34 galaxias con distancias de entre 1 a 15 Mpc de nuestra Galaxia, utilizando el VLA. THINGS tiene características únicas en cuanto a la profundidad de las observaciones en HI, por lo que es la primera vez que se logra hacer una búsqueda como la nuestra. Hicimos cortes en los cubos de datos de 33 de las galaxias, ignorando a M81 por las características distintas de sus observaciones, buscando candidatos de HVCs en sus respectivos mapas de posición-velocidad. Para separar emisión genuina de ruido, consideramos regiones que sólo mostraban emisiones en dos canales consecutivos con 3σ , o tres canales consecutivos con 2σ , donde σ está relacionado con el FWHM característico del instrumento.

De entre las 33 galaxias de THINGS, encontramos un candidato que cumple perfectamente bien con nuestras condiciones establecidas, y 3 candidatos que están al límite de nuestro criterio de selección. Calculamos sus masas, las cuales variaron entre 10^5 a $10^6 M_{\odot}$. También encontramos otro objeto bastante masivo en la galaxia NGC 3621, la cual parece presentar propiedades de una galaxia enana. Su mapa de velocidad muestra cinemática galáctica típica de una galaxia enana. Su radio y velocidad circular calculados corresponden a una masa dinámica mínima de $\sim 4.54 \times 10^8 M_{\odot}$, mientras que su flujo esta asociado a una masa estimada de $\sim 7.96 \times 10^7 M_{\odot}$. Ambos valores corresponden con la masa de HI esperada en galaxias espirales enanas. Debido a que la nube se encuentra proyectada cerca de (o está encima de, así que en la línea de visión de) NGC 3621, no es posible identificar una contraparte óptica en la obtención de imágenes en el óptico.

Después calculamos qué porcentaje de un complejo masivo de nuestra Galaxia podría ser visible en la galaxia más cercana y más lejana de THINGS, para poder hacer una estimación de qué tan realista era la cantidad de objetos que estábamos detectando, y que tipo de objetos estábamos perdiendo. Tomamos como muestra un complejo del tamaño del Complejo C, pero con una masa un poco mayor como la del Complejo A, para mejorar las probabilidades de detección. Encontramos que en la galaxia más cercana de THINGS, NGC 1569 con una distancia de 1.95 Mpc, podemos observar alrededor del $\sim 26\%$ de la masa total de nuestro análogo al Complejo C, mientras que en la galaxia más lejana, NGC 7331 con una distancia de 14.72 Mpc, no podemos detectar nada. Esto nos indicó que en galaxias a grandes distancias nuestros instrumentos actuales no son capaces de detectar HVCs como las que hay en nuestra Galaxia, y también nos hizo esperar el poder encontrar un candidato de entre cada 33 galaxias por factores de probabilidad. Sorprendentemente, si no tomamos en cuenta nuestras detecciones en el límite de nuestro criterio de selección, esto fue justamente lo que encontramos.

0.4 Modelo Teórico del Impacto de una HVC con el Disco Galáctico

Llevamos a cabo un estudio analítico de la interacción HVC-disco, con el propósito de entender la trayectoria asociada a la nube y cómo esta interacción cambia en respuesta a diferentes fenómenos ocurriendo en el medio interestelar (ISM por sus siglas en Inglés). Nuestro primer paso fue seguir una capa de material que ha sido eyectado por el medio, en un escenario de fuente Galáctica, llegando a la atmósfera Galáctica, enfriándose y después

lloviendo hacia el disco nuevamente. La trayectoria que tal material sigue en su camino hacia el disco puede ser aplicado a una HVC de origen extragaláctico, cuya trayectoria es cizallada.

Después dirijimos nuestros cálculos al análisis de la estabilidad del disco gaseoso cuando es expuesto a perturbaciones provenientes del intercambio de momento ejercido por una HVC. Realizamos varios análisis de perturbaciones infinitesimales incluyendo distintos fenómenos físicos para poder encontrar si la interacción puede llevar a pequeñas regiones del disco al borde de una inestabilidad gravitacional. Esto nos ayudó a tener una imagen de cómo podría suceder el proceso de formación estelar debido a la interacción de una HVC con el disco gaseoso Galáctico.

Primero incluimos rotación y después cizallamiento al sistema de ecuaciones que describen tal interacción. El análisis de estabilidad mostró que siempre hay una longitud de onda que lleva el sistema a la inestabilidad, y que la rotación y el cizallamiento tan sólo modifican el criterio clásico de Jeans. En este escenario de interacción, las nubes moleculares que se encuentran ya al borde de una inestabilidad gravitacional no son cizalladas o desbaratadas por el impacto de la HVC, y pueden seguir siendo comprimidas. Finalmente, incluimos campos magnéticos a nuestro sistema y comprobamos nuevamente que incluso los campos no pueden impedir a la HVC de comprimir el medio al borde de una inestabilidad gravitacional.

0.5 Conclusiones

Sabemos que hay varios procesos dinámicos en la Galaxia que pueden ser explicados con acreción de gas al disco Galáctico. Por ello hemos decidido investigar concretamente a las nubes de alta velocidad, o HVCs. Al estudiar al Complejo H, una nube en nuestra propia Galaxia que parece estar interaccionando con el disco Galáctico, encontramos que la nube es mucho más masiva de lo que se pensaba, y las implicaciones de dicho descubrimiento forman parte de nuestro plan de trabajo a futuro, pero mencionamos brevemente algunas. Creemos que el complejo no forma parte de una fuente Gaáctica, ya que se encuentra en el plano Galáctico pero con una velocidad negativa muy alta, que no podría lograrse si proveniese de una fuente. Además, la cantidad de masa contenida en el complejo H es demasiado grande como para provenir de una condensación de la fuente.

La aparente carencia de estrellas en su interior pone al Complejo H como una de las nubes conocidas más masivas de hidrógeno neutro, y tiene la masa y extensión física consistente con galaxias del Grupo Local, por lo que se ha sugerido anteriormente que el complejo es en realidad una galaxia de materia oscura. Pero hay algunos problemas con esta teoría y es que el complejo no parece tener rotación, lo cual dificulta medir cuánta materia oscura podría tener por un lado, y por otro, sería muy extraño tener una galaxia sin rotación.

Otra posible explicación del origen de una nube tan masiva es que podría ser el resultado de la suma de varias HVCs que han colisionado. Pero esto es poco probable ya que no observamos ondas de choque fuertes o ningún tipo de interacción a su interior. Puede ser que el Complejo H es simplemente otra HVCs como las demás observadas en nuestra Galaxia, que por alguna razón tiene una cantidad de gas muy grande.

Cuando buscamos HVCs en otras galaxias, en nuestra muestra de 33 galaxias distintas, encontramos una HVC que cumplía con nuestro criterio de selección, y esto era justamente

lo que esperábamos. Pero parece extraño que el objeto que encontramos se encontrase en una de las galaxias más lejanas, y no en una de las más cercanas, como era de esperarse. Una posible implicación de este resultado es que los grandes complejos no son tan comunes en otras galaxias, o que nuestras observaciones aún no son lo suficientemente buenas para detectarlas y que el objeto que encontramos en realidad es un objeto mucho más masivo, posiblemente el resultado de una interacción de marea con galaxias satélites o enanas. Sin embargo, esto parecería poco probable ya que la mayoría de las galaxias observadas con THINGS son galaxias solitarias, aun así es posible. Una prueba de ello es la galaxia enana que encontramos en NGC 3621.

Si tomásemos en cuenta nuestras otras tres detecciones, entonces el número total de candidatos es mayor al que esperábamos y las implicaciones son completamente diferentes. Podríamos entonces decir que las HVCs grandes y masivas son más comunes de lo que pensábamos y que nuestra Galaxia carece de grandes HVCs después de todo. Otra posibilidad es que lo que hemos detectado, nuevamente, no son HVCs, sino sistemas más grandes, como galaxias enanas que nuestra Galaxia no tiene. Esto, sin embargo, tiene nuevamente el contraargumento de que la mayoría de las galaxias en THINGS son galaxias que parecen carecer de compañeros, a diferencia de otros sistemas como M81. Pero sigue siendo una posibilidad.

Determinar el origen de los candidatos encontrados es difícil, pero nos podemos guiar en lo que sabemos de ellos, como su posición con respecto a su galaxia padre. Los candidatos con distancias mayores a 10kpc sobre el disco dudosamente provienen de fuentes galácticas. Lo mismo aplica a HVCs muy masivas, ya que los cascarones más grandes observados en las regiones más prominentes de H_{II} son del orden de $10^5 M_{\odot}$. Algunos de los candidatos más masivos pueden ser flujos de gas arrancados de satélites que han interactuado con la galaxia anfitriona. Otros podrían estar constituidos de gas condensado en el halo cuando se encuentran cerca del disco. Los candidatos más lejanos de todos pueden ser nubes extragalácticas de diverso origen, pero sin medidas de su metalicidad es difícil saber.

El único de nuestros candidatos que encontramos que tenía una masa total de $10^7 M_{\odot}$ como el Complejo H, resultó ser una galaxia enana debido a su velocidad de rotación. Podríamos entonces pensar que el Complejo H es también una galaxia. Aún así, el Complejo H no muestra ningún tipo de velocidad de rotación y esto lo convertiría en una rareza entre las galaxias.

Nuestras observaciones están de acuerdo con el trabajo numérico realizado por Rand & Stone (1996) and Santillan et al. (2004), en donde la interacción nube-disco produce un supercascarón, como hemos visto en las observaciones del Complejo H, donde parte del material Galáctico parece haber sido arrastrado por él a su paso.

Al hacer un estudio analítico de la interacción nube-disco, encontramos que en todos los procesos que consideramos, hay siempre presente un modo de propagación de onda que lleva al sistema a la inestabilidad gravitacional, y tales estudios nos proveen con una versión modificada del criterio clásico de Jeans. Esta interacción puede provocar el proceso de formación estelar e incrementa la tasa de formación estelar en el disco. Debido a estos resultados, creemos que las HVCs pueden tener amplias implicaciones en la evolución de la Galaxia, lo cual está de acuerdo con nuestra suposición principal en la que la caída de gas resuelve el problema de la evolución y el enriquecimiento químico en la Vía Láctea.

0.6 Trabajo Futuro

Para el Complejo H nos gustaría trabajar más en su origen, ya que es un objeto sumamente masivo que aparentemente no contiene ninguna estrella y es tentador pensar que tiene un origen extragaláctico, incluso que es una galaxia de materia oscura. Pero hay muchos factores en pro y en contra de estas suposiciones por las que deseamos estudiarlo más a detalle.

Tenemos la intención de estudiar mejor a la galaxia enana encontrada en NGC 3621 y saber un poco más sobre su naturaleza. También nos gustaría averiguar como es que un objeto creado por interacción de mareas, como el Río de Magallanes, se vería en una de las galaxias de THINGS, como hemos hecho con el análogo al Complejo C, ya que nos podría dar más indicios sobre si los candidatos encontrados tienen probabilidades de ser HVCs con este origen, o si por el contrario su origen es distinto. También quisieramos probar cómo se vería un objeto como el Complejo C en una de las galaxias de distancia intermedia en nuestro muestreo de THINGS, como lo sería una galaxia a 7 Mpc.

Finalmente, quisieramos aplicar los resultados de nuestro estudio analítico a simulaciones numéricas, específicamente utilizando el código numérico creado por Aveliz & Breitschwerdt (2004, 2005, 2007), el cual parece ser el más apropiado para el tipo de estudios que queremos hacer: seguir la colisión de las HVCs con el disco Galáctico.

1

Introduction

1.1 Gas Accretion In Galaxy Disks

Gas accretion in galactic disks is a physical phenomenon needed in galactic formation theories, since cold dark matter (CDM) models state that the characteristic formation scenario is a hierarchical one (Navarro, Frenk & White 1995). In it, primordial baryons were heated by shock waves from the collapse and exchanged energy through collisions until they reached hydrostatic equilibrium. They first formed small systems, which then merged to form bigger systems. In this model, the densest regions took the form of a filamentary net, where the first systems, the protogalaxies, were formed in the nodes of these filaments. In these protogalaxies the first stars were formed as well.

Eventually, protogalaxies relaxed and in a similar way, they merged to form galaxies, and the galaxies gathered to form galaxy clusters. Density found its higher value in the smallest regions since small-scale fluctuations impose over big-scale ones. But up to our days, this accretion seems to continue in the form of gas clouds with sub-galactic mass that is still being accreted to the disks. It is easy to understand this if we think that a gas rich galaxy has a very big effective cross-section of cloud accretion, which increases as it accretes more gas, and at the same time increases its size.

It is widely thought that the majority of baryons, at least in the local Universe, are located in the intergalactic medium (White & Frenk 1991; Fukugita & Peebles 2004; Sommer-Larsen 2006). Otherwise galaxies are thought to nourish through accretion events, such as mergers and the cannibalism of dwarf galaxies and gas clouds, which is more preponderant at low redshifts (Bond et al. 1991; Lacey & Cole 1993). Recent hydrodynamical models (Bland-Hawthorn 2009) and numerical work (Dekel & Birnboim 2006) show the existence of two accretion processes: hot accretion, more usual in large and dense structures, and cold accretion which is associated with galaxies with lower halo masses, which in turn are associated with the class of galaxies that have an active star formation. This train of thought leads to a situation in which the rate of gas accretion is related to their star-forming rate (Kere et al. 2005).

1.1.1 Continuous Gas Infall Into the Disk

Understanding the life cycle of a galaxy is no easy task, since it involves physics at very different scales, from the cosmological evolution of the entire Universe down to the formation of just one star. This makes it difficult to find realistic models of stellar formation deduced from observations of the dynamics of observed galaxies. One of the most appropriate ways of understanding hierarchical formation is through numerical simulations, since simple mathematical relations are not enough. In these sceneries we can see several important phenomena that take place: high frequency of bars and spirals, and high frequency of perturbations like warps, observations that are not easy to reproduce in the simulations without including gas accretion, as discussed in detail in the following sections.

This “cosmic infall” idea has been previously considered in the CDM theory, and the theories of galactic formation require it. There is also strong observational support of the scenario of gas infall as an essential element in the chemical evolution of galaxies (see Phookun et al. 1993 and Meyer et al. 1994). Ryden & Gunn (1987) showed that in the last third of Hubble time there was a contribution of the order of half of the angular momentum in a galaxy because of material that fell into it, and several observations show that there should be in fact an infall of material in galaxies. An example of this is the study by Binney (2000) where Local Group members are getting close to one another. There are also studies by Blitz et al. (1999) and Braun & Burton (1999) where they argue that high velocity clouds (HVCs) around the galaxy with net negative average velocities have a primordial origin.

Specifically in our Galaxy we can see that the estimations for the orbital decay of the Large Magellanic Cloud (Tremaine 1976), the existence of the Magellanic Stream (Lin & Lynden-Bell 1977), and the tidal perturbation of the Sagittarius Dwarf (Ibata et al. 1994), suggest accretion events that are happening and that will happen.

We may also ask ourselves if this accreted material stays in the halo of the galaxies, if it goes directly to the disk, or if it stays in both. Some authors support the first option (Binney et al. 1998; Jiang & Binney 1999). But chemical evolution observations directly support the second option (Ostriker & Binney 1989; López-Corredoira et al. 1999). On the other hand, non-baryonic material can escape or be captured by the halo, but baryonic matter tends to be directly accreted by the disk, since the baryonic density of the halo is very low and tends to trap accreted material with a low efficiency.

1.1.2 Dynamics

There are several dynamical processes in galaxies that can be explained in a natural way if we take into account the external gas accretion. Such processes include the chemical evolution of the Galaxy, warps, bars and spiral structure, as well as star formation rates. Observations by Wakker, van Woerden, & Gibson (1999) indicate a material infall rate on the disk in the range of $0.5\text{--}5 M_{\odot}/\text{yr}$, while Sancisi et al. (2008) infer a mean “visible” accretion rate of cold gas in galaxies of at least $0.2 M_{\odot}/\text{yr}$.

On the other hand, chemical evolution models in the solar vicinity show an average accretion rate of approximately $2 M_{\odot}/\text{yr}$. In these models the evolution in time of the most observed metals are studied, such as iron and oxygen/iron rates (Nissen et al. 1994; Rebolo

& Perez del Taoro 1995; Israelian et al. 1998; García López et al. 2001), as well as lighter elements (Casuso & Beckman 1997, 1999, 2000, 2003).

The ram pressure effect is another possible mechanism of material infall in galactic disks, which consists on galaxies sweeping material as they move in their equivalent of our Local Group. Some predictions of net accretion rates have been made of a few solar masses per year in the disk, using observations of the relative velocity of the Galaxy and the gas (Hunt & Sciamia 1972, Tinsley 1977).

Another accretion method is the collisions with other galaxies, like for example satellites. But massive collisions tend to heat the stellar component of galaxies and form spheroids when increasing the central bulge mass, or transform the system into a giant elliptical, while what accretion does is replenish the galactic disk and rejuvenate spiral waves or bars, and at the same time they can reduce the disk–bulge ratio (Bournaud & Combes 2002).

HVCs are excellent candidates of a significant amount of material that fills intergalactic space and that according to some authors (Blitz et al. 1999; Braun & Burton 1999; López - Corredoira et al. 1999; Wakker et al. 1999), is accreted by the Local Group galaxies. They could be remanent clouds of the galactic formation, since their metallicity and column density distributions are very similar to the Lyman-alpha forest on one side, and on the other side, if we think that the gas infall rate of low metallicity gas in the disk is constant over a galaxy's lifetime, then at least half of the Local Group mass must consist of HVCs. This hypothesis is supported even more by the observational evidence that its kinematic center is located on the Local Group baricenter (Blitz et al. 1999).

In the same way, HVCs can explain the evolution of the light elements in the Galaxy and the G and K dwarf problem (Lockman et al. 2008). The estimates of the mass rate that falls into the disk thanks to HVCs seem to be consistent with the estimates of continuous star formation rates. Some of these processes will be explained in the next sections.

Star Formation Rates

Interestingly enough, some studies show that stellar formation rates in our Galaxy have maintained the same order of magnitude during the Galaxy's life time (Rana & Wilkinson 1986, Binney et al. 2000), though some temporal fluctuations can be identified (Rocha-Pinto et al. 2000). Kennicutt (1983) and Kennicutt et al. (1994) sustain that this is the general result for spiral galaxies in the middle of Hubble's sequence.

In a closed box model, where there is no gas infall from the exterior, we would expect a natural decrease in the stellar formation rate through time as a result of the HI being consumed. But Barry (1988) and Rocha-Pinto et al. (2000) find that the stellar formation rate in the last 5 Gyr has been constant as a function of time, where some variations of considerable amplitude are superposed. In order to maintain the same order of magnitude for the stellar formation rate, external gas accretion is needed, since an isolated galaxy should have an exponentially decreasing stellar formation rate, even if we take into account the stellar mass loss.

The stellar formation rate seems to oscillate with a higher amplitude in a time scale of one Gyr, which would be plausible if we incorporate into the evolutionary models two additional effects, which are the gas flux to the solar vicinity from within the Galactic plane disk, and whose amplitude is the result of a density wave pattern, and the flux of gas

that comes from the intergalactic medium (Casuso & Beckman 2001). Probably the best candidates for external flux are once again hydrogen and metal poor HVCs. We should also mention the work done by Casuso & Beckman (2006), who suggest that the infall of HVCs in the disk could be responsible for the oscillation observed in the rotation curve on the outskirts of our Galaxy, when provoking strong fluctuations in the stellar formation rates with time.

G and K Dwarf Problem

Another considerable piece of evidence for gas accretion might be the chemical evolution of the Galaxy. This scenario can be inferred by the local distribution of the stars. Present models seem to indicate that the first stars were very massive and luminous, and that the way they were formed was an event that changed in a fundamental way the subsequent evolution. They altered the dynamics of the cosmos by heating and ionizing the gases that surrounded them. They produced and dispersed the first heavy elements, and one would expect that with time more and more heavy elements would be produced increasing the metallicity levels in star-rich galaxies.

But according to the studies made by Carney, Latham, & Laird (1990) and by Rocha-Pinto & Maciel (1996), the metallicity of most of the old stars in the solar neighbourhood is in the relatively narrow range of $-0.6 < [Fe/H] < +0.2$. This is known as the G dwarf problem, and the same happens with the K dwarfs, which give a more precise record of the chemical history of the Galactic disk (Flynn & Morell 1997; Favata et al. 1997; Kotoneva et al. 2002).

Present metal abundances seem to require a continuous infall of gas with metallicities of 0.1 times that of the solar value. Other abundance problems require also an infall rate integrated over the entire disk of a few solar masses per year, like the ones described by Casuso & Beckman (2001), where gas infall dilutes the enrichment of the heavy element production in stars. This would explain the Fe constancy (Twarog 1986; Meusinger et al. 1991) and the light element presence, like deuterium, which tends to be destroyed in stars, yet is observed in the solar vicinity (Hébrard et al. 2002; Wood et al. 2002; Lehner et al. 2002; Lemoine et al. 2002; Sonneborn et al. 2002; Friedman et al. 2002; Kruk et al. 2002; Moos et al. 2002) and close to the Galactic center (Audouze et al. 1976; Jacq et al. 1999; Lubowich et al. 2000; Polehampton et al. 2002). Casuso & Beckman (2001) presented evolution models for the heavy element abundances of Be and B, according to the halo and disk evolution, in which constant infall of gas plays an important role.

The observed chemical evolution tells us that a big amount of gas accretion is needed by the disk in order to justify stellar formation, the distribution of observed metallicities, and the constant metallicity in disk stars during the last 5 Gyr (Feltzing et al. 2001).

Nevertheless, there are other authors, like Dalcanton (2006), who believe otherwise. They presented a series of calculations that showed that only gas-rich systems with low star formation rates are capable of producing and maintaining low effective metallicities. They finally conclude that gas infall produces little noticeable change in a galaxy's metallicity. The subject is still debated.

Warps

For several years, authors like Kahn & Woltjer (1959); Sancisi (1983); Binney & May (1986); Ostriker & Binney (1989); Briggs (1990); Jiang & Binney (1999); and López-Corredoira et al. (2002), have proposed that intergalactic flux accretion might be a possible explanation to several of the observed warps in galaxies. López-Corredoira et al. (2002) affirm that the flux accretion to a disk, with velocities of 100 km s^{-1} and baryonic density of $10 - 25 \text{ kg m}^{-3}$ could generate the observed warps in galaxies like our own, due to the torque it creates when the flux collides with the disk, transmitting its angular momentum to it. Many galaxies seem to show warps (Sanchez-Saavedra et al. 1990; Reshetnikov & Combes 1998), and perhaps their formation is not always due to the same phenomenon, but gas accretion is one of the possible explanations for a few of them. (For a recent review see López-Corredoira et al. 2008).

Bars

Gas accretion can also replenish the young disk in spiral galaxies and rejuvenate spiral waves or bars (Bournaud & Combes 2002). The thickness of a galactic disk and its skill in maintaining its spiral structure and asymmetries is a good tracer of its history in terms of interactions or gas accretion. The constant presence of spiral structure in most galaxies could mean that galaxies have enough gas to be accreted into their external parts, in order to constantly renew the disk instability, even in the presence of a hot stellar disk and a growing bulge mass.

Bournaud & Combes (2002) made some numerical simulations where they studied the formation, destruction and reformation of bars, while the ratio between disk and bulge varied. They took into account external gas accretion in the dynamics of the spiral galaxies. Their results show that there is a big difference in the evolution of galaxies when they have or don't have significant accretion. The simulations where no accretion was used showed that bars were eventually destroyed, while the simulations with accretion showed that a galaxy can revert that evolution and even have several episodes of new bars, increasing the pattern speed (a very nice discussion about this can be found in Elmegreen 2007). This also indicates that it wouldn't be valid to measure the age of a galaxy from the velocity pattern of a bar.

1.1.3 Summary: Importance Of Gas Accretion

Big quantities of gas can be accreted through the lifetime of a galaxy, and it would be possible that the mass of a galaxy may duplicate in a few Gyrs. The presence of gaseous warps in practically every spiral galaxy has been interpreted as a sign that a spiral galaxy accretes material and angular momentum, while at the same time it can invert its evolution, experiment several episodes of new bars, and keep its spiral density wave. The chemical evolution of the Galaxy also seems to require some form of gas accretion in order to explain the metallicity levels observed. Similarly, it has been shown that the star formation rate in our Galaxy seems to be constant and shows a small increment in the time scale of the disk. This can be understood if we add gaseous material to the interior of the disk from the exterior. There are several dynamical processes that can be explained within this scenario,

and it is for this reason that we believe it is important to study the effect of gas infall in galactic disks.

1.2 What are HVCs?

HVCs were first discovered by Muller et al. (1963). They are clouds mostly composed of neutral hydrogen moving at velocities exceeding 90 km s^{-1} towards or away from the local standard of rest frame (LSR), and deviating from the disk velocity by up to 300 km s^{-1} . As such, these clouds of gas must be moving independently of the galactic disk, and their velocities cannot be explained by simple Galactic rotation models (Wakker 1991). They show no optical counterpart and their nature has remained controversial.

Their emissions are for the most part observed in the 21 cm wavelength, although they have also been extensively studied in H α emission and absorption. They exhibit a tremendous variation in size, morphology and velocity, with the largest complexes spanning many degrees on the sky with complicated spatial structure, and the smaller ones, or compact high-velocity clouds (CHVCs; Braun & Burton 1999) having a small angular extent ($\sim 2^\circ$).

Column densities, velocities and metallicities are readily attainable, however, distances are difficult to determine for clouds of primarily neutral hydrogen. This poses a problem, as many fundamental parameters of the cloud, such as the size and density, require the distance of the clouds to be known, and distance and mass distributions provide fundamental demarcations for the formation scenarios.

HVCs form part of the extraplanar gas of our own Galaxy, so the study of their origin and dynamics can help us gain a better understanding of the formation and structure of spiral galaxies in the Universe.

1.2.1 Distances and Abundancies

At the beginning the hypotheses about the origins of HVC's were abundant, and each predicted different distances, from a few to several hundreds of kiloparsecs. It was clear that a more exact distance and metallicity determinations were needed. A good method to determine distances is to use absorption lines with high resolution in not so bright stars in the background, whose distance is already known. This gives us an upper limit to the distance of the cloud. The first attempt was made in 1967 by Prata & Wallerstein, using the CaII K and Na ID lines, which unfortunately are very faint in HVCs. This led the researchers to think that these clouds were basically composed by primordial gas and that they could have an extragalactic origin.

Without knowing the distances, it is hard to understand the radial velocity distribution of HVCs, but even so, kinematics and dynamics can be used (see Lockman 2003 for an example). Kaebler et al. (1985) found that the vertical as well as the radial infall of clouds, together with a slower rotation than the rest of the disk are kinematic characteristics of most HVCs.

During the 90's there was an explosion of studies of absorption lines of HVCs based mostly on data from space observatories, like the International Ultraviolet Explorer (IUE) and the Hubble Space Telescope (HST). Some first limits to distances were derived, like



Figure 1.1: Artistic illustration of a HVC falling towards a spiral galaxy. Credit: Valeria Buenrostro-Leiter

4.5 kpc for the M III cloud (Danly et al. 1993), 2 kpc to complex C (de Boer et al. 1994) and 5 kpc to complex H (Wakker et al. 1998). Some metallicities were also obtained, like 0.1 times solar for complex C, a result obtained by Wakker (1998) and which remains as the present value. This was a conclusive result that indicated that the complex does not have a Galactic origin. (Complex C now has a limit distance of 10 kpc, Thom et al. 2008, and Complex H 33 kpc, Lockman 2003). For a further review about both complexes, please see Chapter 3 and Chapter 2, respectively.

Studies in other spectral ranges have also been made, like in the far ultraviolet. Using the Far Ultraviolet Spectroscopic Explorer (FUSE), it was found that some HVCs are highly ionized. Molecules of H_2 were also found in some HVCs, and in several clouds of intermediate velocities (IVCs).

1.2.2 Possible Origins

HVCs were discovered more than 40 years ago, but the nature of these distinguished objects is still a mystery. The first hypotheses about their origin were advanced by Oort (1966), who proposed several possibilities. Among them the possibility of them being intergalactic gas accreted by the Galaxy, gas condensation in a gaseous corona at high temperatures, tidal debris from the Magellanic Clouds, and clouds expelled from the disk. He argued that the formation of galaxies is still an ongoing process and HVCs represent primordial clouds that are currently accreted by the Milky Way.

More than a decade later, Bregman (1980) made an analysis about the possibility that HVCs are gas flows enriched by heavy elements, thrown up into the lower halo as hot gas ($T > 10^6$ K) as a result of massive stellar formation and their consequent supernovae explosions

in the disk. When the gas arrives at the halo, it cools down and condenses, to then fall back into the Galactic disk as observable HI (Shapiro & Field 1976; Bregman 1980). This is a very popular proposal and is widely known as the Galactic Fountain model.

During the 80's little progress was made in the theoretical understanding of HVCs. Some new hypotheses were proposed, but finally rejected. Nowadays, these clouds are still being studied in order to obtain more appropriate hypotheses, and some interesting proposals have arisen, like models which point to an extragalactical origin. The Magellanic Stream was explained as a tidal bridge and a gas tail produced by the interaction of the Magellanic Clouds with the Milky Way (Mirabel 1981). Blitz et al. (1999) suggested that HVCs are the residual of the hierarchical formation scenario of structures in the Local Group, composed by dark matter mini-halos. This last proposal, together with the galactic fountain scenarios, past tidal debris interactions like the Magellanic Stream (see Westmeier & Koribalski 2008 for more recent studies), and dwarf galaxies accreted to the Galaxy like the Sagittarius Dwarf (see Putman et al. 2004), are currently the most popular. It is most possible that all these ideas are valid, and distinguishing between them depends mostly on determining the distance, metallicity and dynamical condition of the clouds.

For further reading, we recommend an outstanding contribution regarding the structure and distribution of HVCs on large scales by Wakker & van Woerden (1991). Another important review can be found in volume 312 of the Astrophysics and Space Science Library, dedicated to the HVC phenomenon (van Woerden et al. 2004).

1.3 Objectives and organization of this work

In this work, we will focus on the infall of HVCs and their possible impact on star formation in the disk. To do this, we first study in great detail the infall of one of the most massive HVCs in our own disk, complex H, previously studied by Lockman (2003), and now with the highest-resolution HI observation of Complex H ever (Chapter 2).

But HVCs are difficult to study in the Milky Way, especially when it comes to determining their distances, from which many of their fundamental parameters are determined, such as size and density. This is why we searched for HVC-like objects around other galaxies. Chapter 3 deals with the search and study of HVCs in other galaxies, using The HI Nearby Galaxy Survey (THINGS), one of the most complete HI surveys, consisting on 34 nearby galaxies.

Still, current data isn't conclusive. We know there is gas infall near galaxies, but we don't know what happens if indeed such tidal material hits the disk. It is very hard to observe stellar formation in a galactic disk by the impacts of HVCs for several reasons. One has to first find the interphase of the cloud-disk interaction and see if there is stellar formation there, separate that stellar formation from disk phenomena (stellar formation of OB groups, SNe, spiral arms, etc), and then see if this formation could be explained by the mass and energy transferred from the HVC to the medium. Such a study depends deeply on a HVC-disk interaction theory, so one has to do an analytical analysis in any case.

For this reason, in Chapter 4 we present such an analytical study of the possible stellar formation due to the perturbation of an infalling HVC. We follow a gas element in its journey towards the galactic atmosphere, and its trajectory perturbation when it falls over the disk, taking into account several conditions of the interstellar medium, like rotation,

thickness of the disk, and a magnetized medium. Our aim is to determine under which conditions a high velocity cloud would trigger a gravitational instability with the purpose of acknowledging if the interaction is able to trigger star formation, or on the contrary, the high velocity cloud will diffuse in the medium without any other consequences. This analysis has the purpose of giving us a first order idea of the results of such a collision in a realistic context that should guide future numeric simulations. Our final conclusions are presented in Chapter 5.

2

Complex H, A High velocity Cloud in the Milky Way

2.1 Introduction

Complex H is a large neutral atomic hydrogen cloud, one of the most massive of such clouds having no evidence of stars within it in the Milky Way. Its central cloud, HVC 131 + 1200, was discovered by Hulsbosch (1971) and independently by Dieter (1971). After mapping the area, Wakker and van Woerden (1991) found that it contains a multiple set of associated clouds, which they named Complex H, after Hulsbosch.

The complex covers some 478 deg^2 (Wakker & van Woerden 1991) at a low galactic latitude, and has a velocity with respect to the local standard of rest of $V_{\text{LSR}} \approx -195 \text{ km s}^{-1}$. This V_{LSR} is at least 35 km s^{-1} more negative than that permitted for an object in circular Galactic rotation at any distance, and approximately 100 km s^{-1} more negative than the minimum velocity observed for the HI in the Galactic disk. This value gives Complex H the status of a high velocity cloud (HVC).

Some detailed studies have been made of Complex H. Wakker et al. (1998) derived a lower limit of 3.4 kpc to the distance of Complex H by using 17 OB stars. They found no absorption detections in the spectra, and argued that the HVC is probably behind the stars. In their study they discard the possibility that the complex is part of a superbubble (among various reasons, no OB stars are found inside or behind it, as one would expect at superbubble distances). They also discard the possibility that the complex is a dwarf irregular satellite of our Galaxy because of its observed velocity field, which does not match those of irregular galaxies. And if it belonged to the intergalactic clouds in the Local Group, it would exceed the mass of every galaxy in the Local Group. Wakker et al. (1998) thus propose that its origin is an unusual Galactic fountain cloud or an infalling extragalactic cloud.

Morras, Bajaja, & Arnal (1998) observed a region of the complex with the 100 m Effelsberg telescope and presented arguments suggesting that the complex collided with the Galactic HI producing a shell catalogued by Heiles (1979) and which is consistent in size and position with the collision. Morras et al. (1998) find the hole to be at a distance of

22 kpc from the galactic center.

However, Blitz et al. (1999) argue that the complex has a minimum distance of 40 kpc from the Galactic center. They state that if it was closer, its orbit would take it within the gaseous disk of the Galaxy producing a huge region of highly shocked gas, and the energy of this collision would be equivalent to the energy of 10^3 supernovae (SNe), something that is not observed. Therefore, Blitz et al. (1999) argue that the coincidence between the complex and the shell is not possible, adding that the shell has no evidence of expansion, which should be present in this type of interaction. They also state that Complex H must be closer than 50 kpc, or else it would have an unreasonable HI which would make the cloud tidally unstable.

Lockman (2003; thereafter JL03), on the other hand, makes the important statement that this would be true only for prograde orbits. In 2002 he observed a small fraction of the complex at 21 cm with the Green Bank Telescope (GBT), and introduced a model in which the complex had a retrograde orbit (allowing it to have a smaller distance from the galactic center than previously stated by Blitz et al. 1999), with an inclination of $i = 230^\circ$, and a distance from the Galactic center of $R = 33$ kpc. In his conclusions Lockman (2003) proposed that the complex is interacting with the Milky Way, since HI was found at velocities between the cloud and the disk velocities.

Simon et al. (2006) observed mid-infrared sources in the direction of Complex H and searched the 2MASS database for evidence of any dwarf galaxy-like stellar population in the direction of the complex, looking for evidence of current star formation or an evolved population. They found none and concluded that the complex did not have properties similar to those of known dwarf galaxies, placing the complex as one of the most massive HVCs in our Galaxy with no stars. They argued that this would position the complex as one of the few known dark galaxy candidates.

In 2003, Lockman observed a much larger fraction of the complex, in the zone $108^\circ \leq l \leq 138^\circ$ and $-11^\circ \leq b \leq 11^\circ$. Further observations were done in 2003-2004 and again in 2008-2009, which have produced the highest-resolution HI observations of Complex H ever. The present work describes these observations, their corresponding reduction and calibration, and a final analysis. Section 2.2 and 2.3 deal with the observations and data reduction respectively. In Section 2.4, a detailed description of the properties of Complex H is given, and finally in Section 2.5 a discussion and conclusions are presented.

2.2 Observations

Observations were done with the 100 m diameter “Robert C. Byrd Green Bank Telescope” (GBT) in the National Radio Astronomy Observatory (NRAO). The angular resolution of the telescope at the 21 cm wavelength is of $9.1'$ (FWHM). The receiver detected both linear polarizations and had a system temperature of about 18 K at zenith. The detector for most spectra was the GBT Spectral Processor, which has a velocity coverage of $\pm 250 \text{ km s}^{-1}$ centred on -75 km s^{-1} in 512 channels, each with 3 seconds of integration, except in the central regions where it went up to 10 seconds per pixel. Spectra taken in 2008 and 2009 used the GBT Spectrometer which has 16k channels over 12.5 MHz, allowing greater velocity coverage and in-band frequency switching, which effectively doubled the integration times.

2.3 Data Reduction

The spectra were reduced and calibrated using the GBTIDL software package, specific to GBT data. The instrumental base lines were subtracted from each individual spectrum using a second order polynomial fit. Spectra were assembled in a data cube using the AIPS software package, using interpolation functions to the mesh in order to minimize the resolution loss. Data from the Spectral Processor and Spectrometer were placed on a uniform velocity scale with a channel spacing of 1.03 km s^{-1} and an effective channel width of 1.25 km s^{-1} . The analysis of the data cube was performed using the software packages AIPS++ and KARMA. Figure 2.1 shows a channel map of the resulting HI data cube of Complex H at a velocity of -200 km s^{-1} , and a contour map of the complex at -197.5 km s^{-1} is present in Fig. 2.2.

Some specific problems arose during the processing of the data. The first was that some of the data suffered an anomalous velocity shift with respect to the majority, due to calibration problems with the telescope at the time, and the second was that in a small region of the map anomalously high intensities appeared. These problems were corrected by doing new observations in those areas, yielding, finally, a uniform data cube.

2.4 The Observed Properties of the Complex

2.4.1 Distance and Orbit

The distance to Complex H was previously calculated by JL03 by proposing a model where Complex H moves in a circular retrograde orbit around the Galactic center. For this, JL03 used the velocity of an object projected to the LSR by adding the velocity components in the plane to the component in z . The velocity in the plane consists of the azimuthal velocity and the radial velocity, which in terms of l , b and θ can be written as:

$$V_{\text{LSRplane}} = \left[R_0 \sin l \left(\frac{V_\theta}{R} - \frac{V_0}{R_0} \right) - V_R \cos(\theta + l) \right] \cos b \quad (2.1)$$

where R_0 and R are the distances from the Galactic plane to the Sun and to the complex, respectively, l and b are the Galactic longitude and latitude, respectively, z is the altitude towards the north Galactic pole, θ runs in the direction of the Galactic rotation from the Sun-center line on the plane, V_θ is azimuthal velocity on the plane, V_0 is the Sun's angular velocity around the Galactic center, and V_R is the radial velocity of the complex. On the other hand, the component in z for the LSR is simply:

$$V_{\text{LSRz}} = V_z \sin b \quad (2.2)$$

where V_z is the velocity component in z . The sum of both equations gives us the velocity of the complex projected to the LSR:

$$V_{\text{LSR}} = \left[R_0 \sin l \left(\frac{V_\theta}{R} - \frac{V_0}{R_0} \right) - V_R \cos(l + \theta) \right] \cos b + V_z \sin b \quad (2.3)$$

Taking into account that the rotation curve is almost flat over many dozens of kiloparsecs from the Galactic center, and assuming a constant circular velocity of 220 km s^{-1} , LJ03

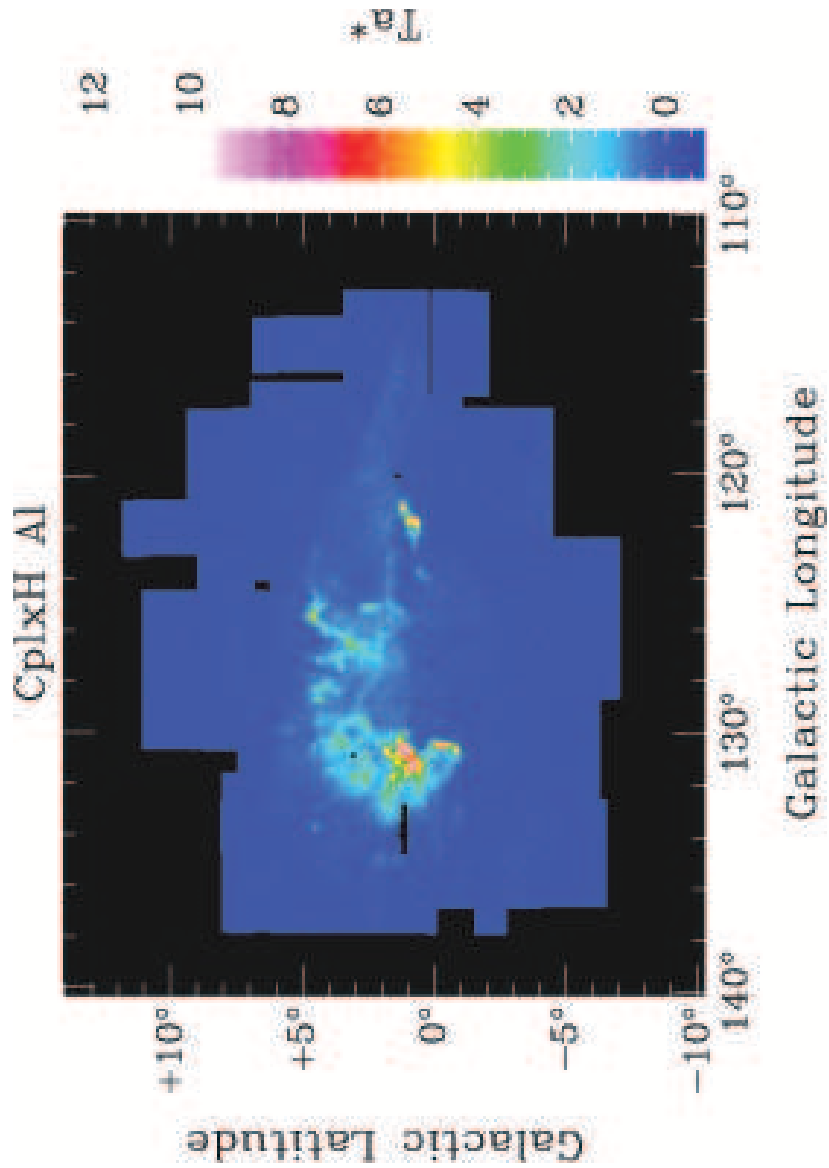


Figure 2.1: Complex H at -200 km s^{-1} . The area in blue is the area of the sky observed with the GBT.

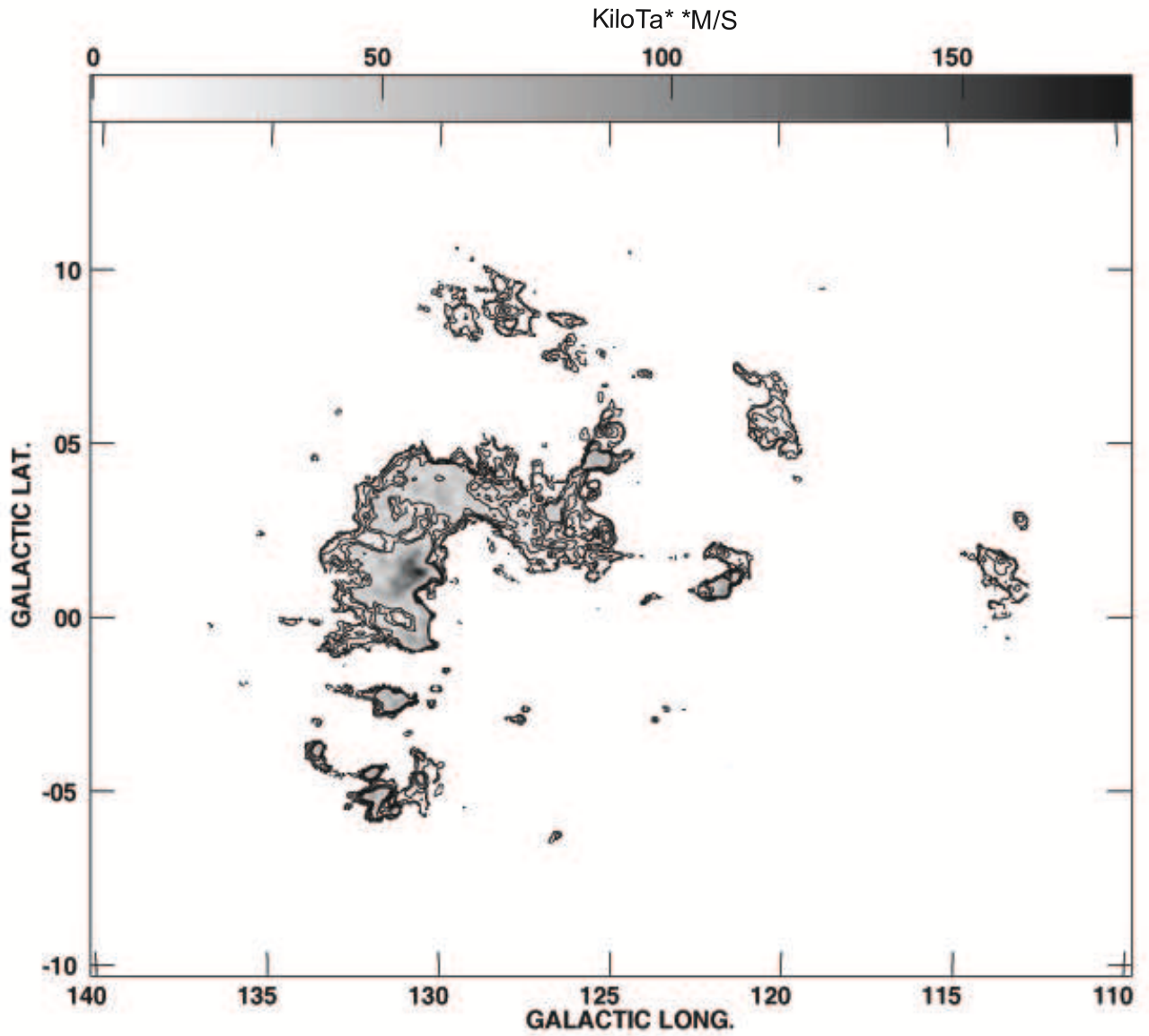


Figure 2.2: Contour map of Complex H at -197.5 km s^{-1} , with levels of 2σ , 3σ , 5σ , 10σ , 15σ , and 20σ , where σ is the sensitivity measured.

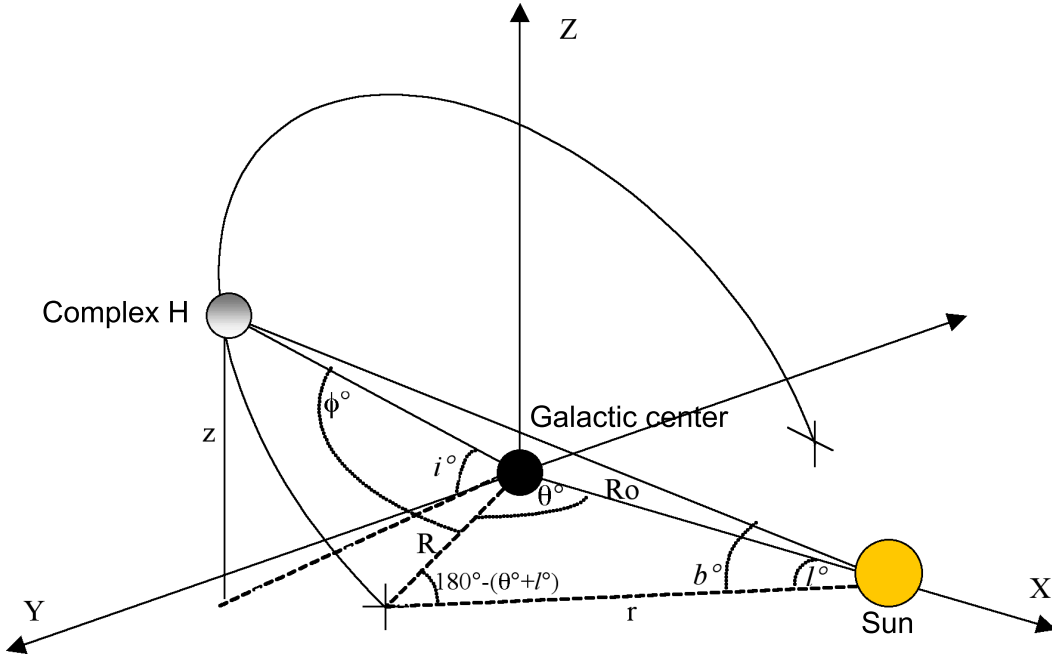


Figure 2.3: The circular orbit of Complex H around the Galactic center. The inclination of the orbit to the Galactic plane is i , the angle of the orbit itself is ϕ , starting on the Galactic plane where the Complex crosses the plane, θ runs in the direction of the Galactic rotation from the Sun-center line on the plane to the complex, l and b are the Galactic longitude and latitude, respectively, and z is the altitude towards the north Galactic pole. R_0 , R , and r are the distances between the Galactic center and the Sun, between the Galactic center and the complex, and between the Sun and the complex, respectively. Important note: the orbit's inclination angle with respect to the Galactic plane, i , is equal to $i - 180$ in JL03's definition.

obtained a distance of Complex H from the Galactic center of $R = 33$ kpc. The corresponding orbital inclination is $i = 230^\circ$, where $i = 0^\circ$ is prograde in the plane, and positive towards the north Galactic pole. With these assumptions, the complex crosses the Galactic plane at $\theta = 38^\circ \pm 5^\circ$ and lies at a distance from the Sun of $r = 27 \pm 9$ kpc. Fig. 2.3 shows the orbit proposed by JL03 for the complex.

We now calculate the orbit of the cloud as a function of the angle of the orbit, ϕ . This angle is equal to zero when crossing the Galactic plane and increases in a retrograde orbit, that is, counterclockwise. For simplicity and illustrative purposes, we will now use a different inclination angle with respect to the Galactic plane, i , which is equal to $i - 180$ in JL03's definition (see Fig. 2.3). We can see that ϕ is oblique and not parallel at all to the $x - y$ axis, since it has a projection in the $x - z$ axis direction, and another projection in the $x - y$ plane.

If we now want to know the velocity of the complex projected on the Galactic plane in the LSR and in terms of the orbit angle and the inclination of the orbit angle (note that in Eq. 2.3 it is in terms of l and b), we do the following. We first need to project ϕ onto the plane. When the complex is on the plane, the distance from the Galactic center to the complex is simply R , but when the complex is above or below the plane, the distance from the Galactic center to the projection of the complex on the plane is $R \cos \phi \cos i$, which is the same as $R_0 \sin l$ (see Fig. 2.4). Therefore we have found the first term of Eq. 2.3.

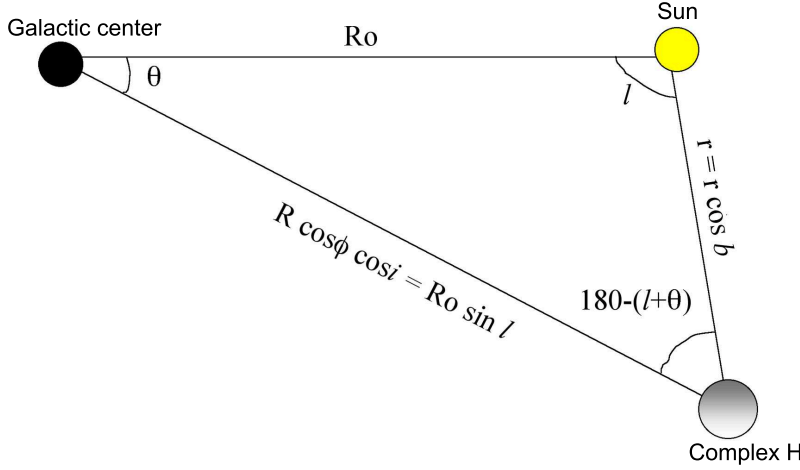


Figure 2.4: Projection of the circular orbit of Complex H around the Galactic center on the Galactic plane. See Sect. 2.4.1 for a description.

We can also notice that $-Vr \cos(l + \theta) = \frac{R}{r} V_R \cos \phi \cos i$ (or $\cos(l + \theta) = \frac{R}{r} \cos \phi \cos i$), and this is the second term of Eq. 2.3. From Fig. 2.3 we can see that b and i start both at the Galactic plane and go up to where the complex is. This means that at all times, b and i are pointing to the same altitude over the plane. In other words: $\sin b = \sin i$, or what is the same, $V_z \sin b = V_z \sin i$, which corresponds to the last term of Eq. 2.3. Finally, we need to substitute the $\cos b$ term by multiplying part of the velocity plane component. From Fig. 2.4 we can see that $\cos(180 - (l + \theta)) = \frac{r \cos b}{R \cos \phi \cos i}$, which gives us $\cos b = -\frac{R}{r} \cos(l + \theta) \cos \phi \cos i$. We finally obtain:

$$V_{\text{LSR}} = - \left[R \cos \phi \cos i \left(\frac{V_\theta}{R} - \frac{V_0}{R_0} \right) + V_R \frac{R \cos \phi \cos i}{r} \right] \left(\frac{R}{r} \cos \phi \cos i \right)^2 + V_z \sin i. \quad (2.4)$$

2.4.2 Size and Mass

We calculated the mass by using the column density contributed by the emission line at the specific velocity range of -150 to -240 km s^{-1} , where the cloud is best seen without the contribution of Galactic gas (a detailed explanation of how to calculate column densities and total masses can be viewed in Appendix A). The column density is given by:

$$\langle N_{\text{HI}} \rangle = 1.82 \times 10^{18} \Sigma T \Delta v \quad \text{cm}^{-2} = 3.64 \times 10^{19} \quad \text{cm}^{-2} \quad (2.5)$$

where a correction for the main beam efficiency was done, by simply dividing T_{a^*} by 0.88 in order to obtain the true brightness temperature. We then multiply it by the area and the distance squared, which gives us the total number of hydrogen atoms that are then converted to solar masses, as:

$$M_{\text{HI}} = \langle N_{\text{HI}} \rangle_{\text{cm}^{-2}} A \text{ deg}^2 \left(\frac{\pi}{180} \right)^2 \left[\frac{\text{str}}{\text{deg}^2} \right] D_{\text{kpc}^2}^2 (3.09 \times 10^{21})^2 \left[\frac{\text{cm}^2}{\text{kpc}^2} \right] \\ 1.67 \times 10^{-24} \left[\frac{\text{gm}}{\text{m}_\text{H}} \right] 0.5 \times 10^{-33} \left[\frac{M_\odot}{\text{gm}} \right] \quad (2.6)$$

Each pixel has an area of $3.5' \times 3.5'$, and we have 215,040 pixels in total in the map, so this gives us a total area of 731.13 deg^2 . Using a distance from the Complex to the Sun of 27 kpc, we have a total mass of:

$$M_{\text{HI}} = 4.6 \times 10^7 M_\odot \quad (2.7)$$

This mass is an order of magnitude higher than that calculated by JL03, which was $6.4 \times 10^6 M_\odot$. This is to be expected with so much higher resolution Hi observations. The higher angular resolution allows us to make a better separation between the Complex and the disk gas, and thus include more gas of Complex H in the analysis by including a lower velocity limit in the integration. This allowed us to map the tail of the complex as well, which was not done before by JL03.

2.4.3 Moment Maps

Generating moments of a specific axis can be very useful in a data cube for data extraction and spectrum analysis. What we really do is collapse an axis (the moment axis) into one pixel, and give the value of that pixel for all the other non collapsed axes to something computed by the values of the data along the moment axis, which will depend on the moment we want to get. An example is the integrated value of pixels in a spectrum. The zero-th moment map gives us precisely that, the integrated intensity of the spectrum, described by:

$$M_0 = \Delta v \Sigma T_i \quad (2.8)$$

where Δv and T_i are the velocity and temperature at the i th pixel, respectively.

Moment 1 is the coordinate weighted by intensity (temperature), used to find the velocity field, described by:

$$M_1 = \frac{\Sigma T_i v_i}{M_0} \quad (2.9)$$

Moment 2, on the other hand, shows us the dispersion of the coordinate weighted by intensity (temperature), used to get the velocity dispersion fields. This is described by:

$$M_2 = \sqrt{\frac{\Sigma T_i (v_i - M_1)^2}{M_0}} \quad (2.10)$$

Moment maps zero, one, and two of Complex H can be seen in Figs. 2.5, 2.6, and 2.7, respectively.

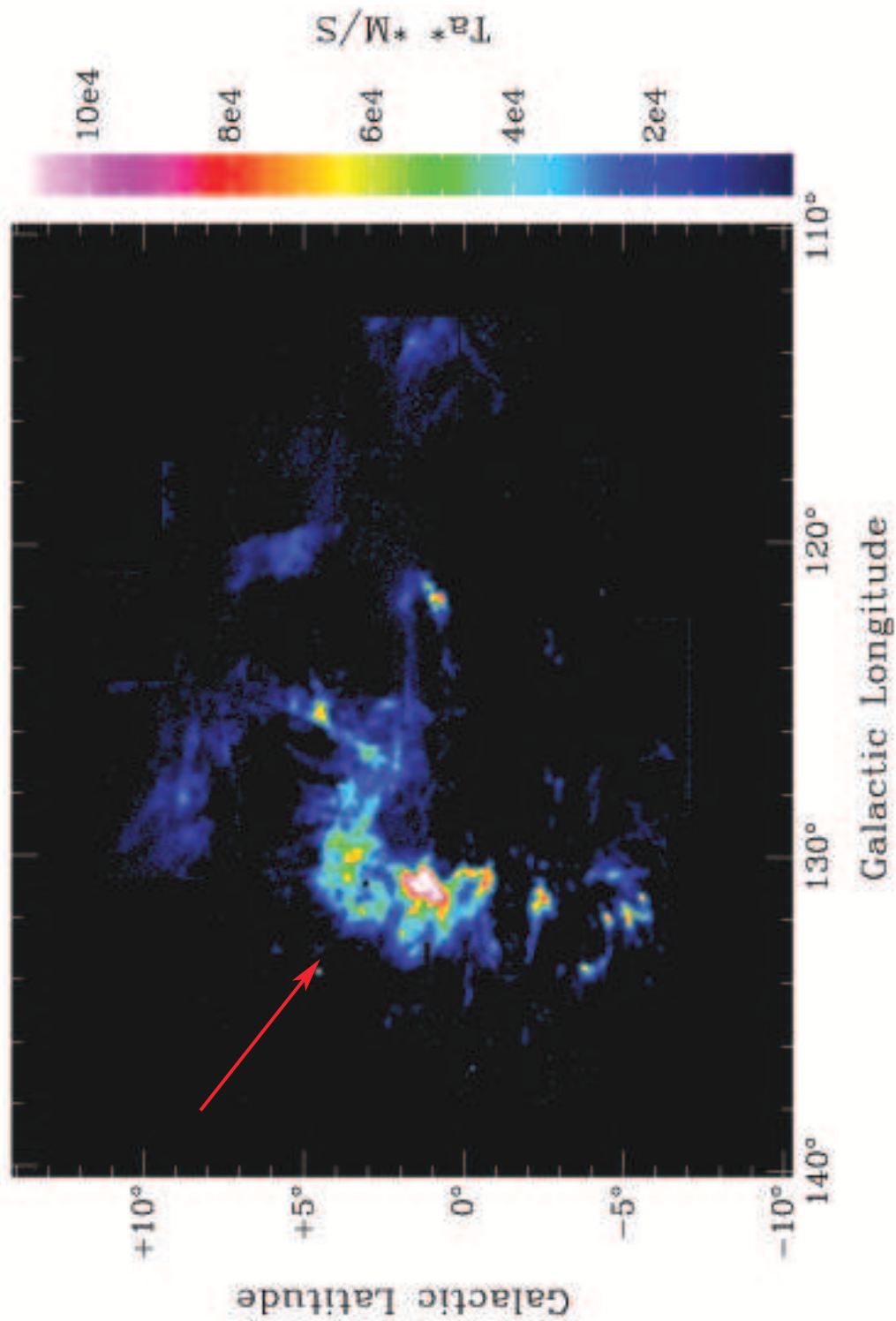


Figure 2.5: Intensity map, or zero moment map of Complex H. The red arrow points to the main body of the complex, while the rest of HI on the upper right of the map belongs to the tail.

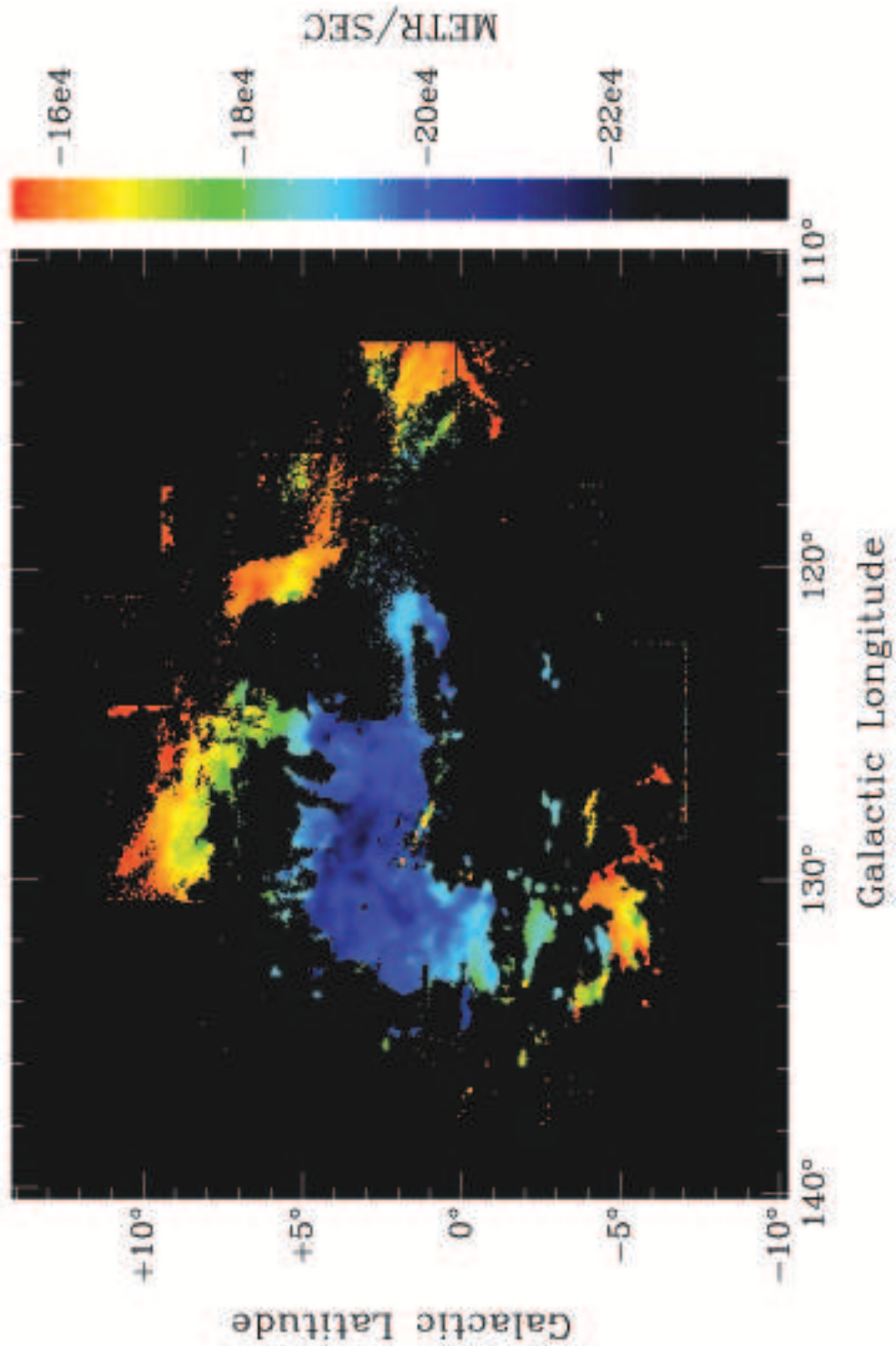


Figure 2.6: Velocity distribution map, or first moment map of Complex H.

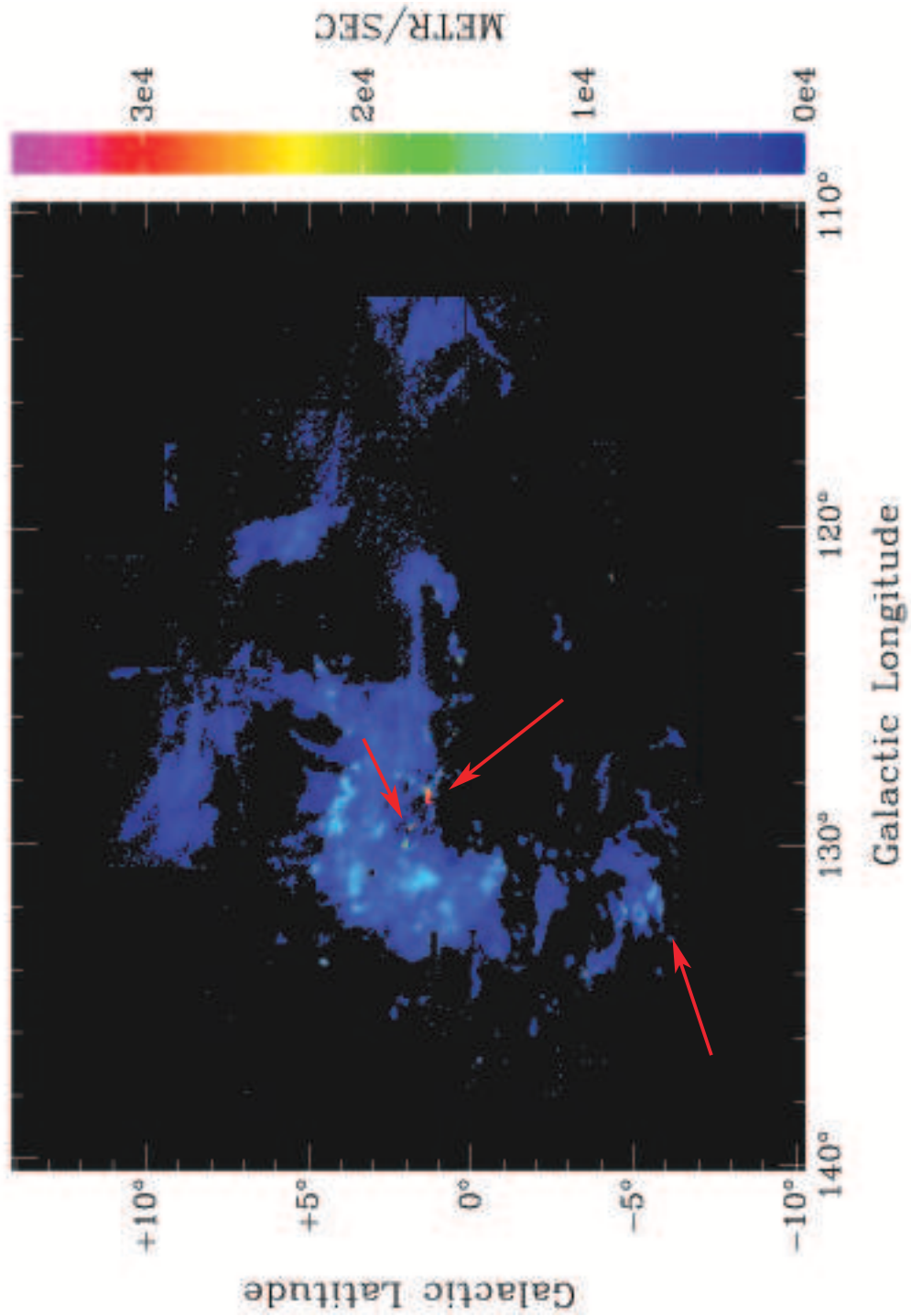


Figure 2.7: Velocity dispersion map, or second moment map of Complex H. The red arrows indicate apparent regions of increased internal turbulence, as discussed in Sect. 2.4.3

The intensity or zero moment map shows the typical head-tail structure found in many HVC complexes (Brüns et al. 2000). It shows a bright core between $-1^\circ \lesssim l \lesssim 5^\circ$ and a tail between $5^\circ \lesssim l \lesssim 11^\circ$. Velocity and brightness are largest near the center and show a rather regular drop toward the edges, possible evidence of its interaction with the interstellar medium.

In the first moment map (Fig. 2.6) it can be appreciated that the head structure of the complex, which lies at about 5° below the Galactic plane, has a decelerating velocity. Fig. 2.8, part 1, shows a cut through the velocity map in the top part of the head of the complex, which seems to have kinematic bridges between the cloud and the Galactic emission, this is, several clumps moving at different velocities which correspond to gaps in the cloud. Three areas of the head are pointed out with red circles. The middle area, b, is the fastest moving, at a speed of $-188 \pm 5 \text{ km s}^{-1}$, while the left area, a, moves at $-173 \pm 5 \text{ km s}^{-1}$, and the right area, c, moves at $-160 \pm 5 \text{ km s}^{-1}$. The same kinematic bridges have been previously observed in Smith's Cloud as well (Lockman 2008). These clumps are likely material stripped from the cloud or the Galaxy itself by the interaction with the disk.

The lowest area though, (part 2 in Fig. 2.8) seems to be moving at a constant and lower speed than the rest of the complex. The deceleration of the head structure is a probable indicator that it might be interacting with the interstellar medium of the Galaxy and therefore slowing down. A further analysis of the second moment map (Fig. 2.7) shows a slight increase in internal turbulence (see bottom red arrow), which would be expected in shocked layers. It is possible to assume that the HVC hit the Galactic disk sideways, penetrated and accelerated previously present material, as already proposed by Wakker et al. (1998). The complex seems to be moving slightly inclined towards us, its tip closer to us than its tail.

The velocity dispersion map (Fig. 2.7), shows several turbulent regions over the complex. Because of perspective reasons, it is hard to tell if these regions are on the inside or outside of the cloud, but one can assume that if the cloud is indeed interacting with the interstellar medium, friction would be responsible for turbulent regions on the outer layers of the cloud. On the other hand, a very strong turbulent region (which we named T₁) can be clearly observed in the second moment map near position $l \sim 128.44^\circ$, $b \sim 1.3^\circ$. A further analysis shows that the velocity in this region ranges from -170 to -232 km s^{-1} (see Fig. 2.9). There also seems to be a kinematic bridge present. At a slightly higher latitude, there seems to be a smaller turbulent region (named T₂) with velocity ranges around -164 to -210 km s^{-1} (see Fig. 2.10). Both images (Fig. 2.9 and Fig. 2.10) show two distinct bridges between the cloud and the Galaxy, which we will call B₁ and B₂. The bridge to the right, B₁, belongs to the visible tail zone, while the bridge on the left, B₂, seems to belong to a tail that hides behind the cloud core itself. Furthermore, they correspond well to the range of velocities of the visible tails, which are around -160 to -209 km s^{-1} . This might be a strong indication that the turbulent regions are not in fact turbulent, but just a superposition of the cloud core over a hidden tail, thus causing the strong visible velocity jumps, which is most likely material which has been ram-pressure stripped from either the complex or the Galaxy by the cloud-disk interaction.

The clearest image of bridge B₂ is shown in Fig. 2.11. The V shape of this bridge has its highest velocity at -218 km s^{-1} and has the lower velocities in the zone of the

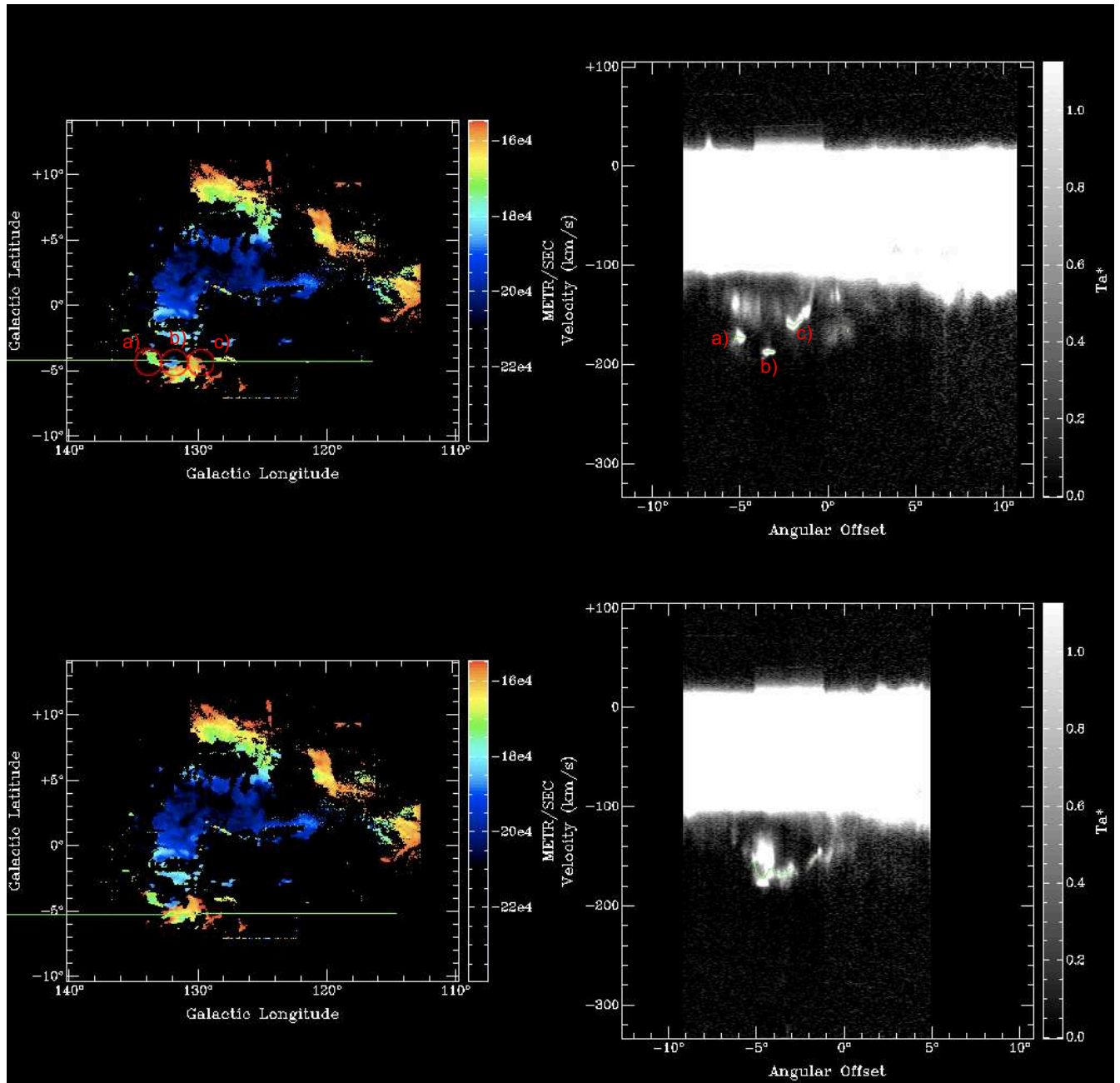


Figure 2.8: Cuts through the first moment map of Complex H at the head position (left), and their corresponding position–Velocity diagrams (right). 1) Cut through higher part of the head where 3 structures are visible inside red circles, called a), b) and c). 2) Cut through lower part of the head.

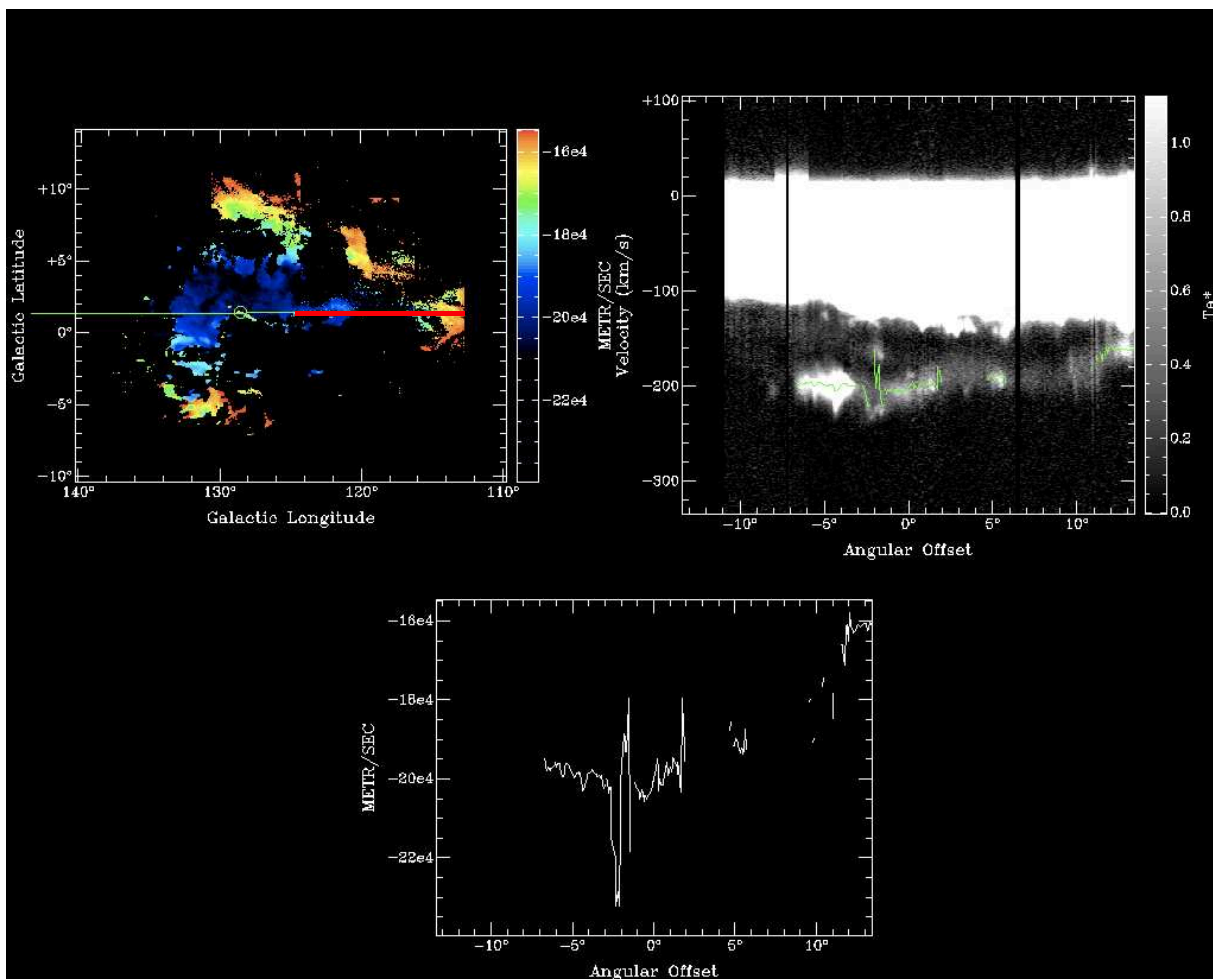


Figure 2.9: Cut through second moment map of Complex H where a turbulent region (which we named T_1) seems to be present (left). The green circle corresponds to the turbulent region described in Sect. 2.4.3. The red line on the cut indicates the tail zone bridge (which we named B_1) seen on the right panel, which is its pV diagram. The bottom panel shows a closer look at the turbulent zone in the pV diagram.

visible tail (which reaches Galactic velocities). This is probably due to the superposition of the complex main body over the hidden tail. Interestingly enough, Figures 2.10 and 2.11 also show a change in the Galactic disk gas where the complex begins to lose velocity. It seems very likely that this interaction is indeed disturbing the outer part of the Milky Way. Finding regions of star formation due to this interaction is a difficult task for we would need to separate that stellar formation from disk phenomena (such as stellar formation of OB groups, SNe, etc), and then see if this formation could be explained by the mass and energy transferred from the HVC to the medium. Such a study depends deeply on a HVC–disk interaction theory, so an analytical analysis must be done in any case. But the perturbation of the gas component hints us that some form of perturbation is indeed going on in the Milky Way due to the interaction.

The velocity distribution map (Fig. 2.6) shows how the tail of Complex H has lower

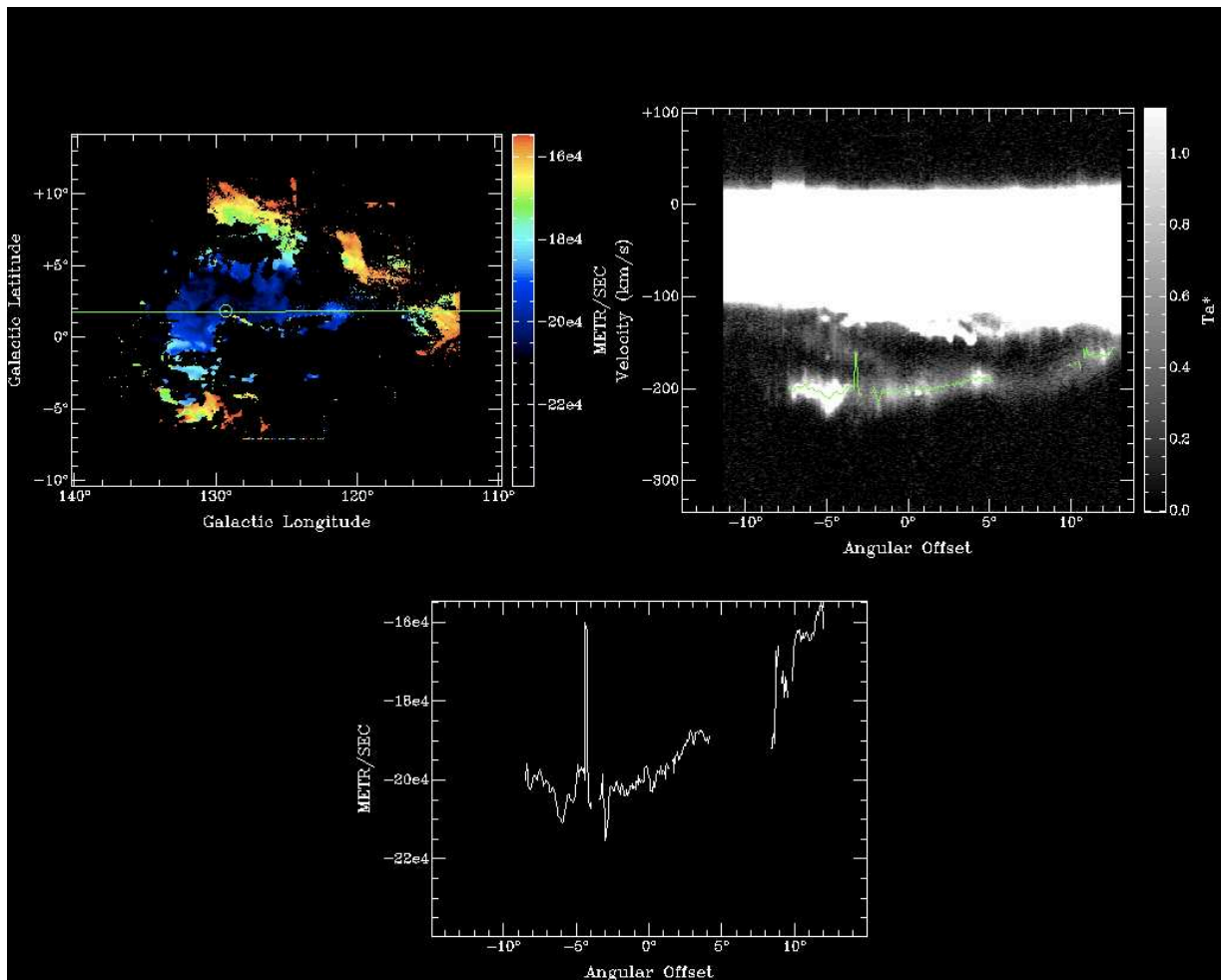


Figure 2.10: Cut through second moment map of Complex H where a turbulent region (which we named T_2) seems to be present. See Fig 2.9 for details.

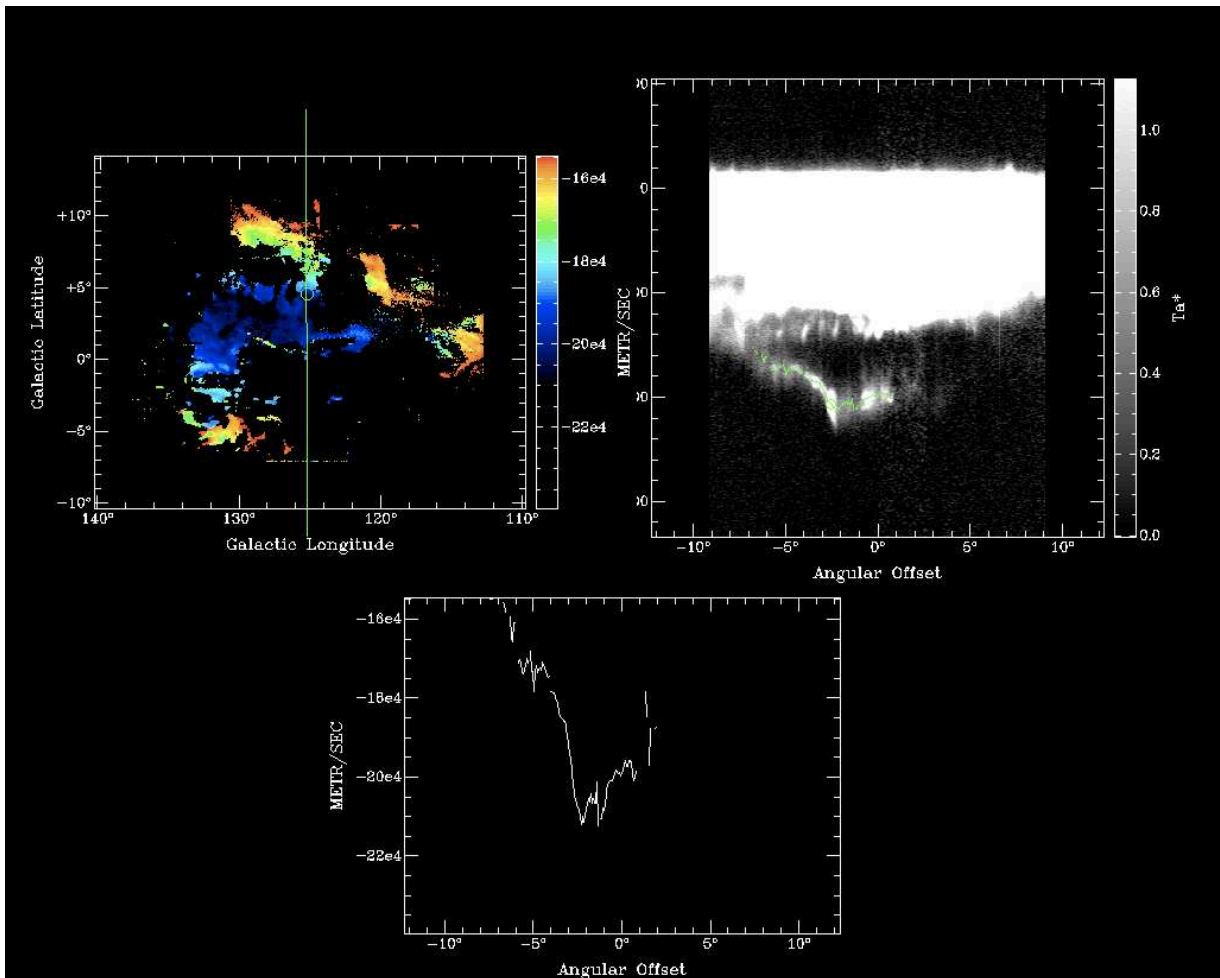


Figure 2.11: Cut through second moment map of Complex H (left) showing a clear bridge (which corresponds to bridge B₂) in the pV diagram (right) between the complex and the Galaxy. The strong drop in velocity corresponds to the area inside the green circle on the cut in the left panel. The bottom panel shows a closer look at the bridge zone pV diagram.

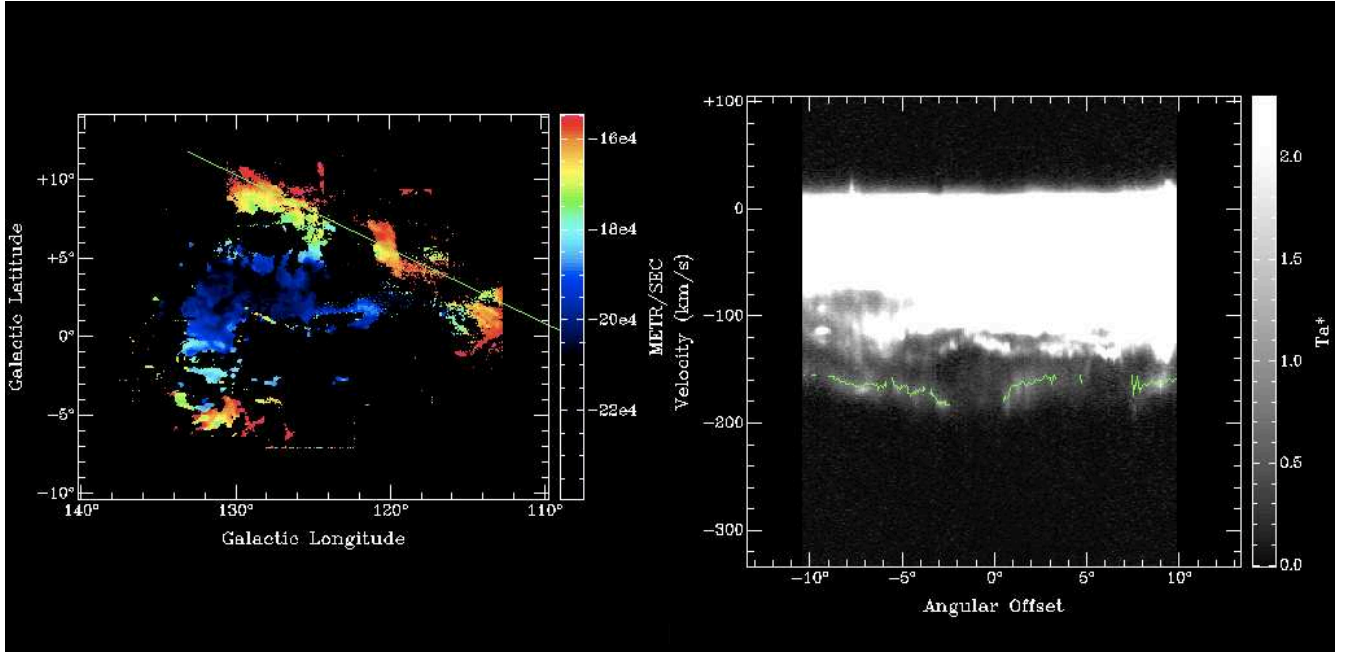


Figure 2.12: Cut through second moment map of Complex H along the tail (left) showing gas velocities close to those of the Galaxy in the pV diagram (right).

velocities than the main body of the complex, and a cut through the tail (Fig. 2.12) shows how close these velocities are to the Galactic ones. This seems to indicate that the interaction between the complex and the Galaxy has been stripping the complex from its material and might imply that the complex is in the process of being destroyed, as previously suggested by L03. It should also be noted that the left and right sides of the tail are closest to having Galactic velocities, while the central part, the region of the complex core, presents higher velocities. This is yet another indication that the complex has a velocity component coming towards us.

2.5 Discussion and Conclusions

New observations of Complex H, taken during 2003-2004 and again in 2008-2009, were reduced and analyzed. These have allowed us to produce the highest resolution HI observations of Complex H ever, and to perform the most detailed study yet of its morphology. Previous work by JL03 showed the velocity of the complex projected to the LSR in terms of l , b , and θ . We now calculated the velocity projected to the LSR but in terms of ϕ , the orbit angle which increases in a retrograde orbit, and i , the inclination of the orbit angle with respect to the Galactic plane. At the present time ϕ is equal to zero as the complex is crossing the Galactic plane, and $i = 50^\circ$ (though in JL03 paper the equivalent is $i = 230^\circ$), but it gives us an idea of the angle of the orbit that the complex follows through time if we suppose a circular orbit.

We conclude that the mass of Complex H is one order of magnitude higher than previously thought ($4.6 \times 10^7 M_\odot$), and the reason for this is a higher angular resolution

observation that has allowed us to make a better separation between the complex and the disk gas, and thus to include more gas of the complex in the analysis which forms part of the tail structure.

From the additional observations and calculations included in this chapter we have confirmed the initial deduction in JL03 that Complex H is moving with an average velocity of -200 km s^{-1} in the southeast direction, but with an angle inclined towards us, leaving a major wake of gas as it interacts with the gas in the disc of the Milky Way. The front of the main cloud is suffering a deceleration as it impinges on the Galactic disk gas, and the interactive process is leaving zones of obviously enhanced turbulence throughout the cloud, in the main dense zone as well as in the tail. But the new observations also show what seems to be a hidden part of the tail lying right behind the main body of the complex, and kinematic bridges between the cloud and Galactic emission not observed before, which are likely material stripped from either the cloud or the Milky Way itself. We interpret this as evidence for the interaction between the cloud and the gaseous halo of the Milky Way. Furthermore, the outer part of the Milky Way seems to be perturbed by the interaction with the complex. This all suggests that the complex plunged into the outer parts of the Milky Way and accelerated previously present material, so the bridges observed most likely contain Galactic gas.

The full implications of the impact of such a massive cloud belong to part of our proposed future studies, but we will briefly mention a few. As already stated by Blitz et al. (1999), it seems very unlikely that Complex H is part of a fountain. The strongest evidence is that it is located nearly in the Galactic plane, but with a large negative forbidden velocity. Fountain material that was ejected from the disk only to fall back later, would not have such a large forbidden velocity at $b=0^\circ$. Also, the mass is much too large for a condensation from the fountain (Avillez 1999). The apparent lack of evidence for current star formation or evolved populations inside the complex places it as one of the most massive known neutral hydrogen clouds with no stars, as previously stated by Simon et al. (2006), and it has an HI mass and physical extent that are consistent with those of other Local Group galaxies. Therefore, it has been suggested by Blitz et al. (1999) and by Simon et al. (2006) that Complex H is in fact a dark matter galaxy. But a problem with this model is that the complex does not seem to have rotation, so it is hard to measure how much dark matter it could actually have. In either case, it would be very strange to have a galaxy with no rotation. Assuming that it does rotate, the complex should be self-gravitating, and thus, Blitz et al. (1999) argue that unless the dark matter mass is more than 10 times the baryonic mass, it must be at a distance of Mpc, not kpc. But in our observations we see the complex interacting with the Milky Way, which indicates us that it is within a few tens of kpc of the sun. Simon et al. (2006), on the other hand, argued that if the HI extent of the cloud is smaller than the scale radius of the dark matter halo, the observed kinematics would not be expected to reflect the full gravitational potential of the halo. In either case, the lack of rotation does not agree very well with their model.

Another possible explanation for such a large massive cloud is that it is the sum of several HVCs which have collided. This is unlikely, as we do not see strong shocks or any type of interaction. Perhaps Complex H is just another HVC like other HVCs observed in our Galaxy, which for some reason has a very large amount of gas.

It is important to note that a way of overcoming the limitations of studying the Galactic

halo from within is by observing external galaxies preferably of a similar type to the Milky Way. Some HVC-like HI clouds and extraplanar gas have been found in a variety of nearby galaxies with distances of less than 7 kpc, e.g., throughout the circumgalactic environment of M31 (Thilker et al. 2005, Westmeier et al. 2005, and references therein), high velocity gas in NGC 6946 and extraplanar gas in NGC 253 (Boomsma et al. 2005a, b), in NGC 891 and NGC 2403 (see the modelling paper by Fraternali & Binney 2006 for references to the data papers), in M33 (Grossi et al. 2008), and in M83 and M51 (Miller & Bregman 2005). Studying them might bring new information on the origins of HVCs. This is what we will see in the next chapter.

3

HVCs in THINGS

3.1 Introduction

Much progress has been made in the study of HVCs (clouds of mostly neutral hydrogen moving at velocities that are not at all explicable by galactic rotation) in the Galaxy, for column densities, velocities and metallicities are readily attainable. However, distances are not so easily attainable, and this poses a problem since many fundamental parameters of the clouds, such as size and density, are still not well determined. Furthermore, distance and mass distributions are fundamental demarcations for their formation scenarios along with metallicity. A way of overcoming the limitations of studying the Galactic halo from within is by observing external galaxies preferably of a similar type to the Milky Way, where anomalous neutral gas can more easily be found. As already pointed out by Fraternali et al. (2001, 2002), some halo HI features found in external galaxies are probably analogues of some Galactic HVCs. HVC-like HI clouds and extraplanar gas has been found in a variety of nearby galaxies with distances of less than 7 kpc, e.g., throughout the circumgalactic environment of M31 (Thilker et al. 2005, Westmeier et al. 2005, and references therein), high velocity gas in NGC 6946 and extraplanar gas in NGC 253 (Boomsma et al. 2005a, b), in NGC 891 and NGC 2403 (see the modelling paper by Fraternali & Binney 2006 for references to the data papers), and in M83 and M51 (Miller & Bregman 2005).

But evidence for extra-planar gas in spiral galaxies is difficult to obtain, mainly because of the intrinsic technical difficulty of detecting objects with relatively low column density. Also, some of the HVCs observed are barely resolved with the biggest telescopes like the GBT, where observations are only useful for the nearest local galaxies and our own.

This work is an attempt to find evidence for HVCs near other galaxies, using data from “The HI Nearby Galaxy Survey” (THINGS). This is the first time that such a search can be performed across so many galaxies, thanks to the unique characteristics of the THINGS database. The minimum mass of a cloud filling a $10''$ beam (200 pc to 500 pc at the distance of our targets) is $\sim 2 \times 10^5 M_\odot$, while observed HVCs around the Galaxy have masses $>10^6 M_\odot$. This means we have good probabilities of detecting HVCs in the THINGS survey. Nevertheless, only the densest regions of such clouds will be found, as we will not be sensitive enough to pick up low surface brightness material at column densities

below $0.1 M_{\odot} \text{pc}^{-2}$, which correspond to $1.2 \times 10^{19} \text{cm}^{-2}$. Typical HVC column densities range from $\sim 7 \times 10^{17} \text{cm}^{-2}$ to 10^{19}cm^{-2} , while peak core densities may reach 10^{20}cm^{-2} to 10^{21}cm^{-2} .

Section 3.2 deals with the search for HVCs in the THINGS survey, beginning with an overview of the observations, and furthermore a discussion of what detectability is expected in the data. In Section 3.3 there is a discussion of the candidates found, and Section 3.4 includes a discussion of how a HVC of the Milky Way would look like in one of the THINGS galaxies and some final conclusions.

3.2 Search For HVCs In THINGS

3.2.1 Observations

The THINGS survey is based on a sample of 34 nearby galaxies with distances that range from 2–15 Mpc (resulting in linear resolutions of 100 to 500 pc) and high velocity ($2.6\text{--}5.2 \text{km s}^{-1}$) and angular ($\sim 6''$) resolution of HI emission. The sample is a subset of the sample of galaxies observed in the Spitzer Infrared Nearby Galaxies Survey (SINGS) (Kennicutt et al. 2003), a multiwavelength project designed to study the properties of the dusty ISM in nearby galaxies. It was also designed to complement the GALEX Nearby Galaxies Survey (NGS; Gil de Paz et al. 2007). THINGS galaxies cover a wide range of masses, from low mass dwarf galaxies to massive spiral galaxies, excluding early type (E/S0) galaxies that have little or no HI. Local Group galaxies were also excluded because of their large size on the sky, as were edge-on galaxies to avoid projection effects. The Main characteristics of the target galaxies, and the properties of the maps used for this study, are listed in Tables 3.1 and 3.2.

All THINGS galaxies were observed with the NRAO Very Large Array (VLA) in D, C, and B configurations with typical integration times of 1.5, 2.5, and 7 hr, respectively, placing the velocity resolution of the HI data at the limit of what can be achieved in studies of extragalactic HI with the VLA (Walter et al. 2008). The three configurations used for the observations allow us to trace the fine structure of HI and to recover extended emission in the objects. Data was taken over two years, from 2003 to 2005, and the total observing time was ~ 500 hours (this includes data taken from the VLA archive).

The calibration and data reduction were done using the AIPS package (see Walter et al. 2008). The uv data were inspected for each array and bad data points due to either interference or cross-talk between antennae were removed, after which the data were calibrated. To ensure that identical beam sizes were used for all THINGS observations, and to avoid being distracted by structures with the shape of the beam, the data were subsequently convolved to a common resolution of $10''$. This resulted in a good compromise in terms of the size of the beam and a typical rms noise per channel of 0.5mJy beam^{-1} for a 2.5km s^{-1} channel (corresponding to $N_{\text{HI}} = 1.5 \times 10^{19} \text{cm}^{-2}$). Most cubes are 1024×1024 and have an area of $\sim 25' \times 25'$. For more information please refer to paper Walter et al. (2008).

Galaxy	RA	Dec	D	V _{sys}	Incl	P.A.	Morph Type
-	hh mm ss.s	dd mm ss.s	Mpc	km/s	deg	deg	-
DDO 154	12 54 05.89	+27 09 9.9	4.3	375.48	66.0	229.7	10
DDO 53	08 34 07.2	+66 10 54	3.56	17.71	31.0	132	10
HO I	09 40 32.3	+71 10 56	3.84	140.39	12.0	50	10
HO II	08 19 5	+70 43 12	3.39	157.10	41.0	177	10
IC 2574	10 28 27.7	+68 24 59.4	4.02	48.62	53.4	55.7	9
M81 DwA	08 23 56.0	+71 01 45	3.55	112.00	23.0	49	10
M81 DwB	10 05 30.6	+70 21 52	5.3	346.41	79.8	321	10
NGC 1569	04 30 49.0	+64 50 53	1.95	-85.57	63.0	112	10
NGC 2366	07 28 53.4	+69 12 51.1	3.44	100.07	63.8	39.8	10
NGC 2403	07 36 51.1	+65 36 2.9	3.22	133.10	62.9	123.7	6
NGC 2841	09 22 2.6	+50 58 35.4	14.1	635.16	73.7	152.6	3
NGC 2903	09 32 10.1	+21 30 4.3	8.9	556.64	65.2	204.3	4
NGC 2976	09 47 15.3	+67 55 0	3.56	2.61	64.5	334.5	5
NGC 3077	10 03 19.1	+68 44 02	3.82	5.00	46.0	45	10
NGC 3184	10 18 17.0	+41 25 28	11.1	593.30	16.0	179	6
NGC 3198	10 19 55	+45 32 58.9	13.8	661.18	71.5	215	5
NGC 3351	10 43 57.7	+11 42 14	9.33	779.00	41.0	192	3
NGC 3521	11 05 48.6	-00 02 09.2	10.05	798.24	72.7	339.8	4
NGC 3621	11 18 16.5	-32 48 50.9	6.64	730.14	64.7	345.4	7
NGC 3627	11 20 15.0	+12 59 29.6	9.25	717.34	61.8	173	3
NGC 4214	12 15 39.2	+36 19 37	2.94	292.85	43.7	65	10
NGC 4449	12 28 11.9	+44 05 40	4.21	202.66	60.0	230	10
NGC 4736	12 50 53	+41 07 13.2	4.66	307.57	41.4	296.1	2
NGC 4826	12 56 43.6	+21 41 0.3	7.48	407.87	65.2	120.9	2
NGC 5055	13 15 49.2	+42 01 45.3	7.817	499.26	59.0	101.8	4
NGC 5194	13 29 52.7	+47 11 43	7.768	456.22	42.0	172	4
NGC 5236	13 37 0.9	-29 51 57	4.47	509.98	24.0	225	5
NGC 5457	14 03 12.6	+54 20 57	7.38	226.45	18.0	39	6
NGC 628	01 36 41.8	+15 47 00	7.3	659.12	7.0	20	5
NGC 6946	20 34 52.2	+60 09 14.4	5.9	43.50	35.9	242.7	6
NGC 7331	22 37 4.1	+34 24 56.5	14.72	815.64	75.8	167.7	3
NGC 7793	23 57 49.7	-32 35 27.9	3.82	227.15	49.6	290.1	7
NGC 925	02 27 16.5	+33 34 43.5	9.16	552.54	66.0	286.6	7

Table 3.1: Characteristics: main properties of THINGS galaxies from Walter et al. 2008. *Galaxy* stands for the galaxy name, *RA* and *Dec* are right ascension and declination in J2000.0, *D* is the distance from the Sun to the galaxy, *V_{sys}* is the systemic velocity, *Incl* and *P.A.* are inclination and position angle, and *Morph Type* is the morphological type of the galaxy (from LEDA). For further information please refer to Walter et al. (2008).

Galaxy	Sensitivity	Image Size	PIX	N(channels)	Δv	Lower limit	Linear resolution
-	mJy beam ⁻¹	pixels	"	-	km s ⁻¹	to mass M_{\odot}	pc
DDO 154	0.60	1024	1.5	57	2.6	4.08E+04	208
DDO 53	0.64	1024	1.5	41	2.6	2.98E+04	173
HO I	1.14	1024	1.5	36	2.6	6.18E+04	186
HO II	1.25	1024	1.5	54	2.6	5.28E+04	164
IC 2574	0.84	1024	1.5	83	2.6	4.99E+04	195
M81 DW A	0.78	1024	1.5	46	1.3	1.81E+04	172
M81 DW B	0.74	1024	1.5	34	2.6	7.64E+04	257
N1569	0.95	1024	1.5	75	2.6	1.33E+04	94.5
N2366	0.74	1024	1.5	66	2.6	3.22E+04	167
N2403	0.35	2048	1.0	61	5.2	2.67E+04	156
N2841	0.48	1024	1.5	132	5.2	7.01E+05	684
N2903	0.50	1024	1.5	87	5.2	2.91E+05	431
N2976	0.38	1024	1.5	42	5.2	3.54E+04	173
N3077	0.90	1024	1.5	98	2.6	4.83E+04	185
N3184	0.42	1024	1.5	72	2.6	1.90E+05	538
N3198	0.42	1024	1.5	72	5.2	5.88E+05	669
N3351	0.35	1024	1.5	70	5.2	2.60E+05	487
N3521	0.52	1024	1.5	109	5.2	4.38E+05	519
N3621	0.88	1024	1.5	72	5.2	2.85E+05	322
N3627	0.39	1024	1.5	92	5.2	2.45E+05	448
N4214	0.83	1024	1.5	98	1.3	1.32E+04	143
N4449	1.00	1024	1.5	45	5.2	1.30E+05	204
N4736	0.48	1024	1.5	68	5.2	7.66E+04	226
N4826	0.54	1024	1.5	75	5.2	2.22E+05	363
N5055	0.34	1024	1.5	87	5.2	2.55E+05	490
N5194	0.54	1024	1.5	77	5.2	2.54E+05	388
N5236	0.95	1024	1.5	123	2.6	6.98E+04	217
N5457	0.56	2048	1.0	69	5.2	2.24E+05	358
N628	0.76	1024	1.5	58	2.6	1.49E+05	354
N6946	0.76	1024	1.5	115	2.6	9.72E+04	286
N7331	0.57	1024	1.5	116	5.2	9.08E+05	714
N7793	1.15	1024	1.5	91	2.6	6.46E+04	190
N925	0.76	1024	1.5	100	2.6	2.34E+05	444

Table 3.2: Properties of the data used for the search. *Galaxy* stands for the galaxy name, *Sensitivity* is the σ measured, *Image size* corresponds to the number of pixels in RA and Dec (all images are square). The pixel size *PIX* is being given in arcsec. *N(channels)* is the number of velocity (frequency) channels used to search through; this is set by how the original THINGS survey data were collected and reduced. Δv is the average channel width, *Lower limit to mass* is the minimum mass of a cloud filling the beam that can be detected and *linear resolution* is the size in pc corresponding to 10'' angular resolution.

3.2.2 Detectability of HVCs

Of the 34 THINGS galaxy data cubes, 33 were inspected. M81 was excluded from the analysis. Because of its large angular size and velocity range, and the ongoing interaction with M82 and NGC 3077, there is hardly any area that is free enough from emission so one can search for HVC candidates. The cubes inspected have uniform noise characteristics, within a single channel and from channel to channel. The sensitivity drops, though, by up to 50% just beyond the areas that were mapped due to primary beam attenuation. This means that in the center of the map, clouds down to a mass of $10^6 M_{\odot}$ can be seen, but sensitivity is gradually lost by as much as a factor of 2 at $16'$ from the center of the galaxy (the FWHM of the VLA primary beam at 21 cm wavelength is $32'$).

We based our search on a visual inspection of position—Velocity diagrams of each of the THINGS galaxy data cubes, with the help of the Karma software package. The cuts in the cubes were made across each galaxy and the surrounding area (see Fig. 3.1). The size, in kpc, is governed by the distance to the given galaxy. The maps were inspected before any primary beam correction, so that the noise remains uniform. This allows the eye to pick up those features that seem significant. No software code was used to search for the candidates, since low level artifacts are easily picked up by the human eye but not by the code. A code would even pick parts of the galaxy, for anything above a certain flux level would be considered and would have to be checked by the eye anyway. A nice example of this can be observed in NGC 3521, where “gas at unexpected” velocities seems to be very obviously present (see Fig. 3.2). Two separate velocity systems appear, one being the differential rotating disk signature, and another which appears as a line with a smaller velocity gradient. A study done by Brinks & Burton (1984) shows that this gas is in fact the print of the galaxy’s warp. They compared synthetic line profiles with the observed ones for the M31 system and noticed that the feature of neutral atomic gas that formed a diagonal line in the position—velocity diagram corresponded to the kinematic and structural parameters of a warp (see Fig. 3.2). The smallest area around a galaxy with an HVC candidate in the data cubes was of $\sim 27 \text{ kpc}^2$ (NGC 7793), and the biggest one was of $\sim 100 \text{ kpc}^2$ (NGC 2841). The areas and velocity ranges of the observations in every galaxy are listed in Table 3.3.

Two main conditions had to be fulfilled by the HVC candidates. They had to be traceable within two or three adjacent Hi spectral channels, to overcome signal to noise uncertainties, and they should appear above a set level (an agreed limit above which detections can be trusted) of $2\text{--}3\sigma$, depending on what the actual channel maps look like (3σ detections in two channels, or 2σ detections in three channels). Still, there is some level of subjectivity involved in order to discard detections which could be due to remaining low-level artefacts in the data near noise level.

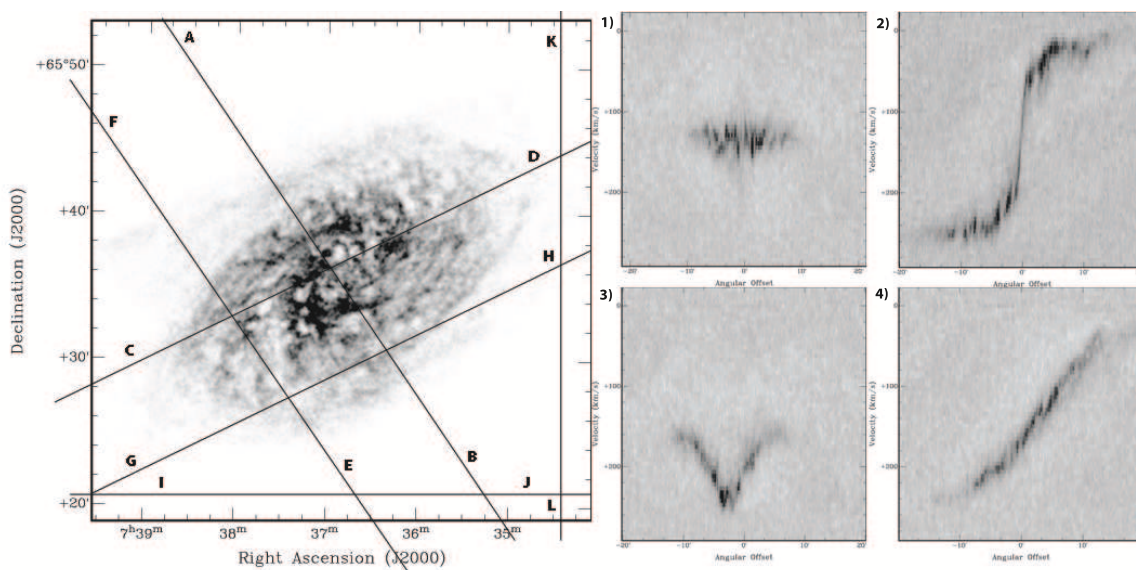


Figure 3.1: Cuts through NGC 2403 (left panel) showing how the cuts were made across each galaxy including their surrounding areas, and their resulting position-Velocity (pV) diagrams (right panel). Line AB represents panel 1) to the right. Line CD results in panel 2), line EF results in panel 3), line GH results in panel 4), and lines IJ and KL show empty pV diagrams when no forbidden gas is found.

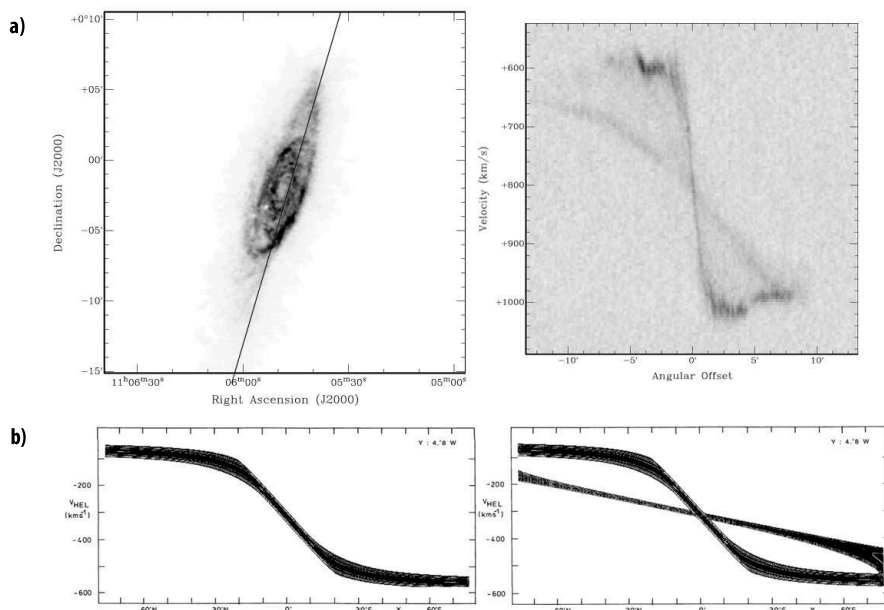


Figure 3.2: a) Cut through NGC 3521 (left panel) where “gas at unexpected velocities” is detected in its pV (right panel). b) Synthetic pV diagrams done by Brinks & Burton (1984) show a cut through a galaxy without a warp (left), and a cut through a galaxy with a warp (right), showing that the gas in NGC 3521 turns out to be an extended warp of this galaxy, and not an HVC detection.

Galaxy	Area	Velocity Range
-	kpc ²	km s ⁻¹
DDO154	1.03E+03	302.69–447.34
DDO53	7.03E+02	-34.11–65.97
HolmbergI	8.18E+02	97.15–187.42
HolmbergII	6.37E+02	102.31–239.03
IC2574	8.96E+02	-65.05–146.28
M81dwA	6.99E+02	85.93–137.50
M81dwB	1.56E+03	300.94–356.16
NGC0925	4.65E+03	428.01–654.00
NGC1569	2.11E+02	-152.66–7.87
NGC2366	6.56E+02	20.09–187.69
NGC2403	1.02E+03	-20.78–288.67
NGC2841	1.10E+04	296.82–974.74
NGC2903	4.39E+03	338.91–783.75
NGC2976	7.03E+02	-105.21–106.05
NGC3077	8.09E+02	-156.47–93.39
NGC3184	6.83E+03	498.91–682.56
NGC3198	1.06E+04	476.81–844.25
NGC3351	5.60E+03	609.12–966.58
NGC3521	6.35E+03	525.47–1085.01
NGC3621	2.44E+03	555.46–923.10
NGC3627	4.74E+03	486.94–958.12
NGC4214	4.79E+02	230.35–355.55
NGC4449	9.83E+02	92.53–319.56
NGC4736	1.20E+03	143.76–489.74
NGC4826	3.10E+03	221.26–603.61
NGC5055	5.66E+03	279.87–724.47
NGC5194	3.55E+03	266.70–659.55
NGC5236	1.97E+03	355.20–670.62
NGC5457	5.37E+03	85.55–436.58
NGC628	2.96E+03	588.09–735.60
NGC6946	1.93E+03	59.74–353.69
NGC7331	1.20E+04	536.28–1132.20
NGC7793	8.48E+02	113.94–346.15

Table 3.3: Observation Characteristics: *Galaxy* stands for the name of the galaxy, *Area* indicates the area that was observed in each of the galaxies in kpc², and *Velocity Range* indicates the range of velocities that the galaxy was observed at with respect to the Sun in km s⁻¹.

3.3 Results

3.3.1 HVC candidates

After a thorough inspection of all the subcubes, five candidates were found in total, one each in NGC 2841, NGC 3198, NGC 3621, NGC 4736, and NGC 7793. The results are presented in Fig. 3.3 in terms of pV diagrams, and the intensity maps, or zero moment maps, are presented in Fig. 3.4.

Upon further inspection we considered the candidate near NGC 2841, which presents a bright cloud that seems to be detached from the galaxy itself, to be a solid detection. The flux profile of this candidate is shown in Fig. 3.5. The following of the three candidate galaxies had detections that were at the limit of our detection criteria, NGC 3198, NGC 4736, and NGC 7793. The object found in NGC 3621, on the other hand, seems to have the properties of a dwarf galaxy. Its velocity map, or first moment map (see Fig. 3.6), shows galactic kinematics typical of a dwarf galaxy. Its radius and circular velocity (not corrected for any inclination) give us a minimum dynamical mass of $\sim 4.54 \times 10^8 M_\odot$, whereas its flux gives us an estimated mass of $\sim 7.96 \times 10^7 M_\odot$. Both values agree well with the HI mass expected in dwarf spiral galaxies, which have $M_{\text{HI}} \leq 10^9 M_\odot$ (Schombert et al. 1995). Due to the fact that the cloud lies in projection close to (or is it on top of, so along the line of sight to) NGC 3621, it isn't possible to identify in direct optical imaging any optical counterpart.

Contour maps of all the possible candidates were done. For those candidates with extended emission, maps were done after convolving them to a beam size of $30''$. Fig. 3.7 shows the contour maps of the individual relevant channels for NGC 2841 with a $10''$ beam, Fig. 3.8 for NGC 3198 with a $10''$ beam, Fig. 3.9 for NGC 3621 with a $10''$ beam, Fig. 3.10 for a $30''$ beam, Fig. 3.11 for NGC 4736 with a $10''$ beam, Fig. 3.12 for NGC 4736 with a $30''$ beam, and Fig. 3.13 for NGC 7793 with a $10''$ beam.

3.3.2 Mass estimate

Mass estimates of the HVC candidates were made using AIPS to obtain the fluxes in the velocity channels where the HVC candidates are detected. A detailed explanation of the process can be viewed in Appendix A. Once the fluxes were calculated, the mass and flux were used in the relation:

$$M_{\text{HI}} = 235.6 D^2 \sum_i \text{HI}_{\text{flux}} \quad (3.1)$$

to obtain the approximate mass of the candidates. A correction to this mass had to be applied due to primary beam attenuation. For this, I used the fact that the VLA primary beam is nearly circularly symmetric and is close to being a Gauss function with a full width at half maximum (FWHM) of $32'$, so at $16'$ radius, the function has a value of 0.5. For each HVC candidate I measured the distance from the center of the map on the channel maps which show the object best. Then I got the value of the Gauss function, and then multiplied the inverse by the HI mass that was derived.

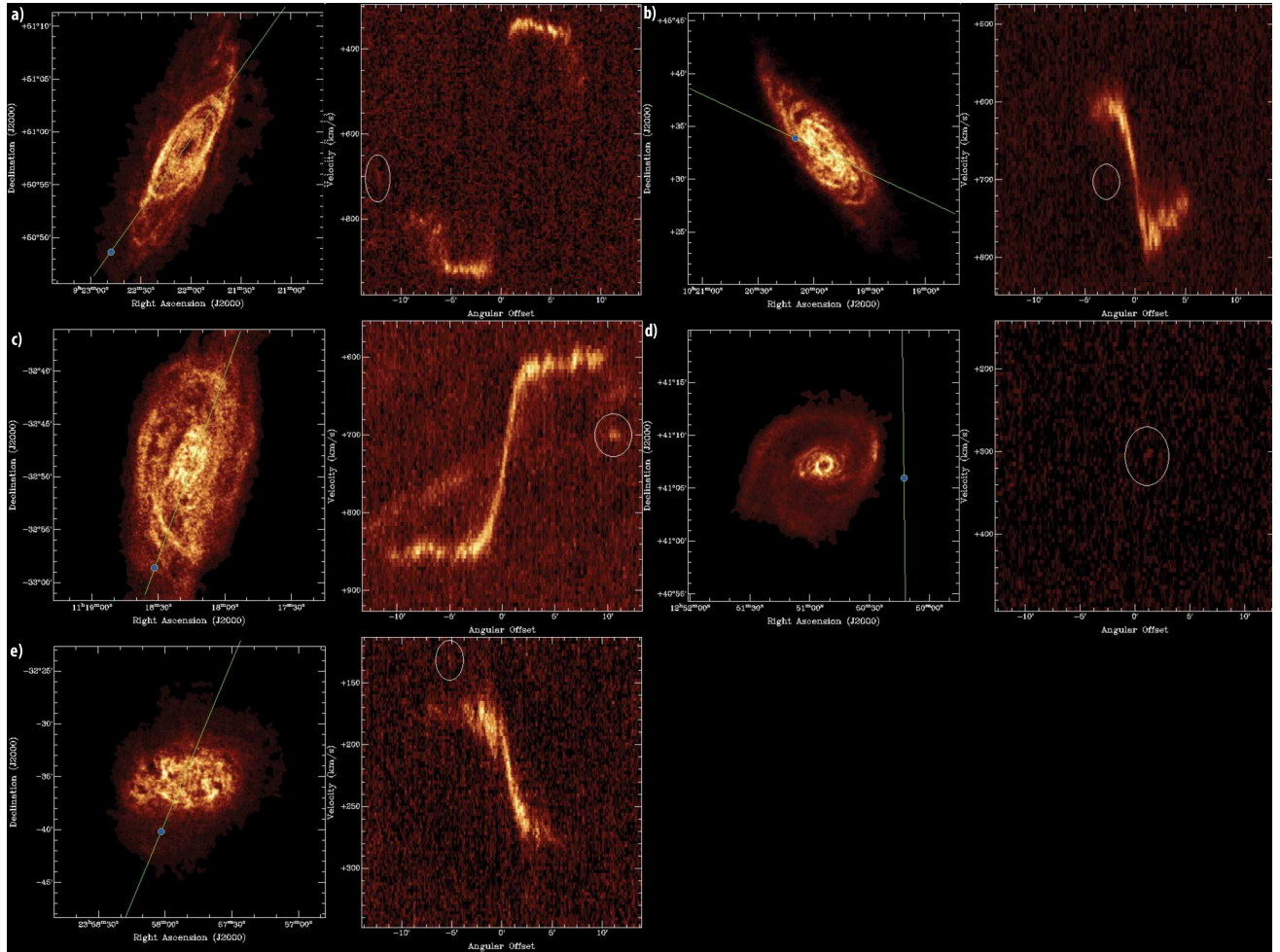


Figure 3.3: Cuts through the 5 galaxies and their corresponding pV diagrams where the HVC candidates can be seen. In the galaxy image (left), the green line corresponds to the cut through the galaxy, and the blue circle indicates the position where the candidate is seen. In the pV image (right), the candidate is visible inside the white ellipse. Galaxy a) corresponds to NGC 2841, galaxy b) to NGC 3198, c) to NGC 3621, d) to NGC 4736, and e) to NGC 7793.

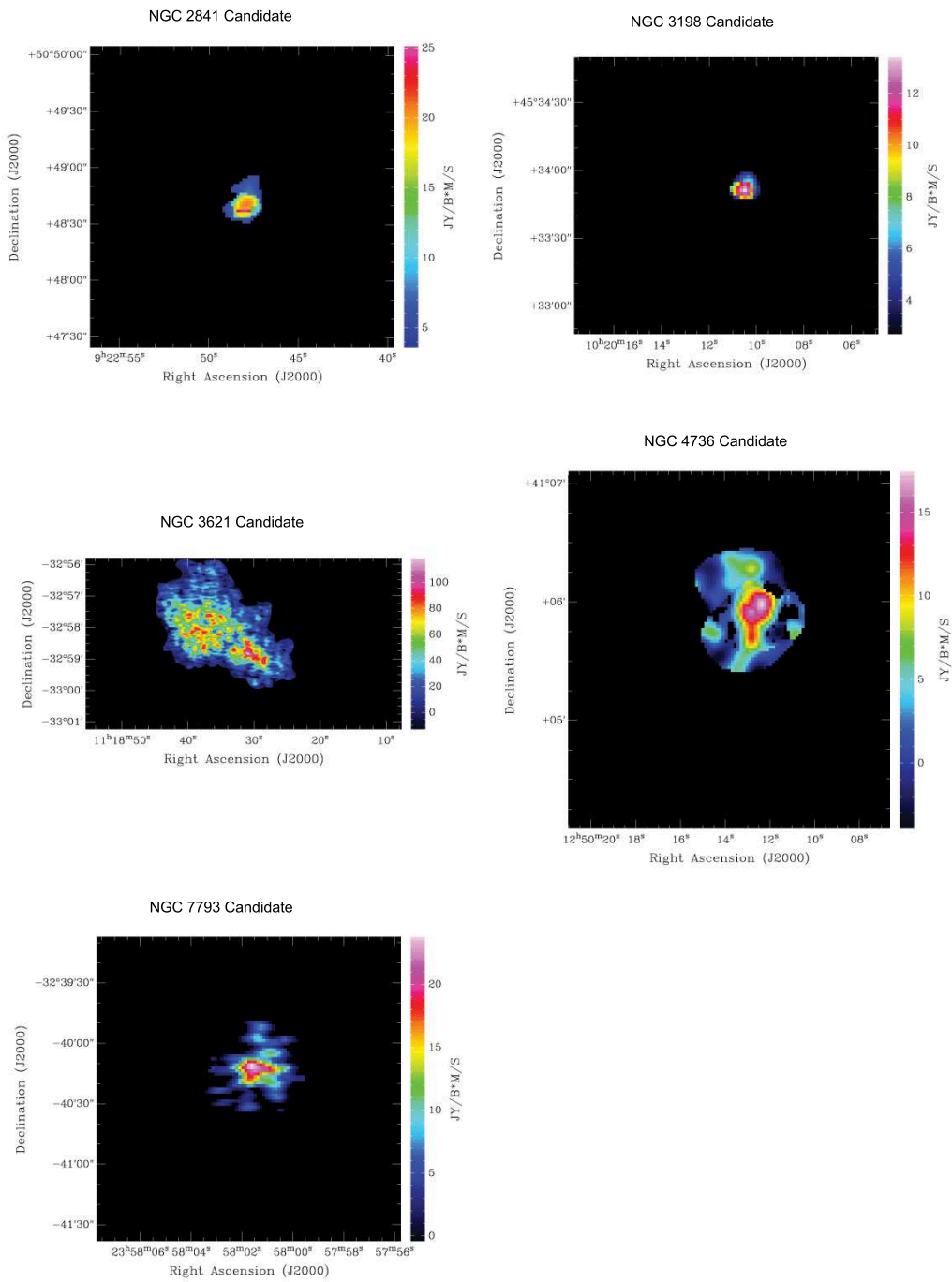


Figure 3.4: Intensity maps or moment 0 maps of all candidates.

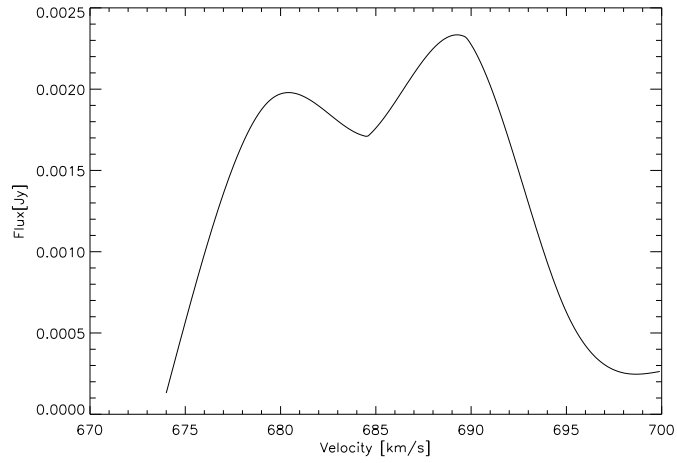


Figure 3.5: HI spectrum of the HVC candidate in NGC 2841

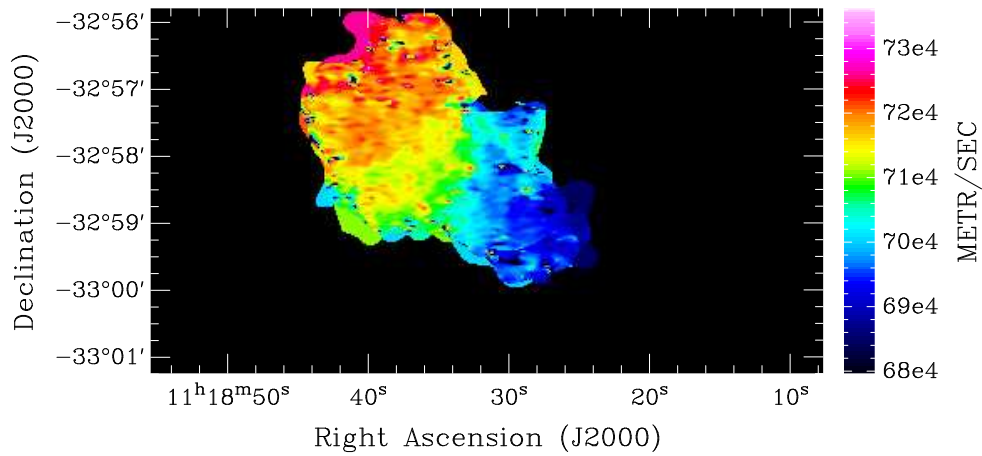


Figure 3.6: Moment 1 map showing the velocity field of the object found near NGC 3621.

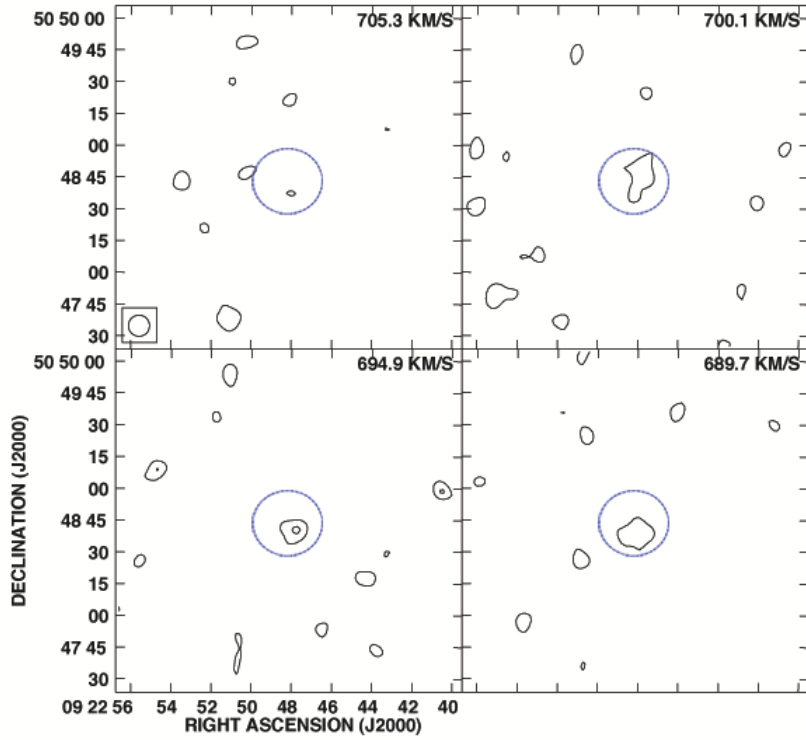


Figure 3.7: Contour maps of the channels where the HVC candidate in NGC 2841 is visible with a $10''$ beam. The blue dotted circle indicates a fixed position in each channel which aids to see the evolution of the candidate through the channels. The heliocentric velocity is indicated in each panel in km s^{-1} . The size of the beam is given in the lower right corner of the first panel only.

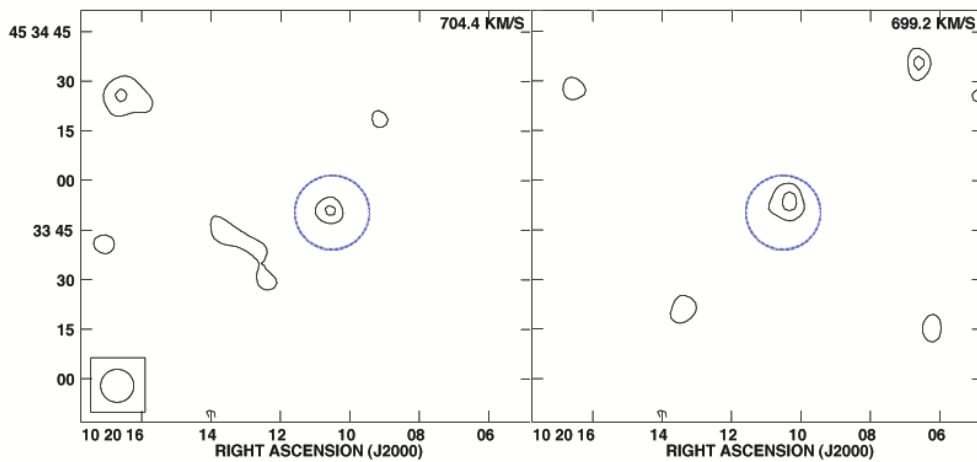


Figure 3.8: Contour maps on the channels where the HVC candidate in NGC 3198 is visible. See Fig 3.7 for details.

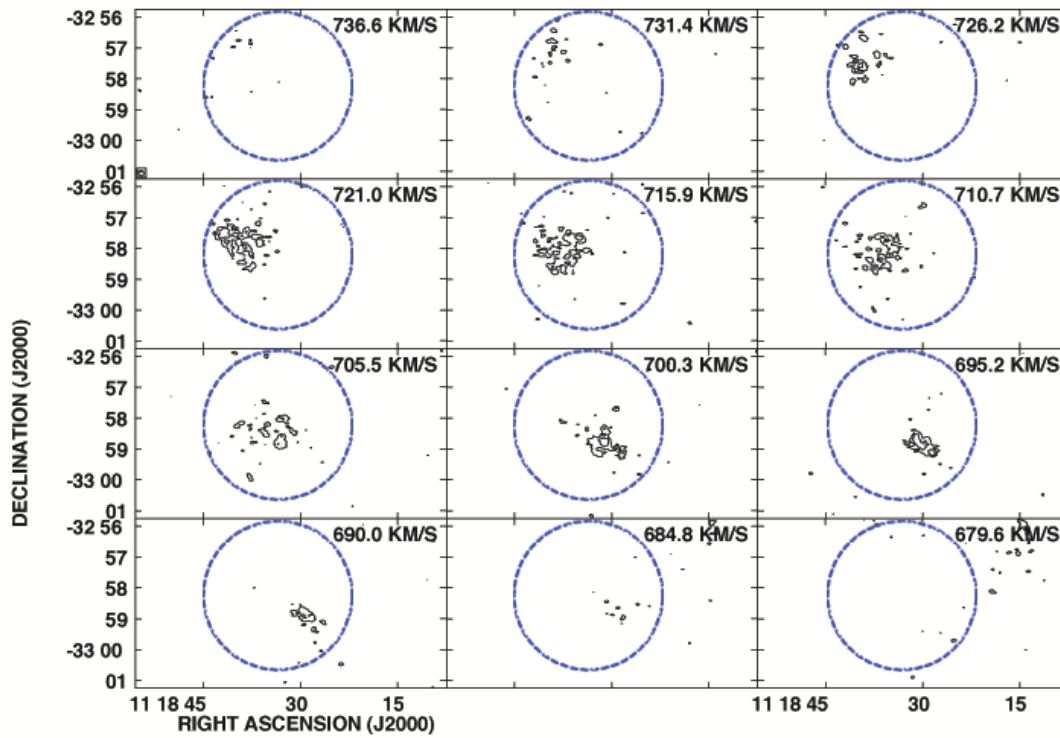


Figure 3.9: Contour maps on the channels where the HVC candidate in NGC 3621 is visible. See Fig 3.7 for details.

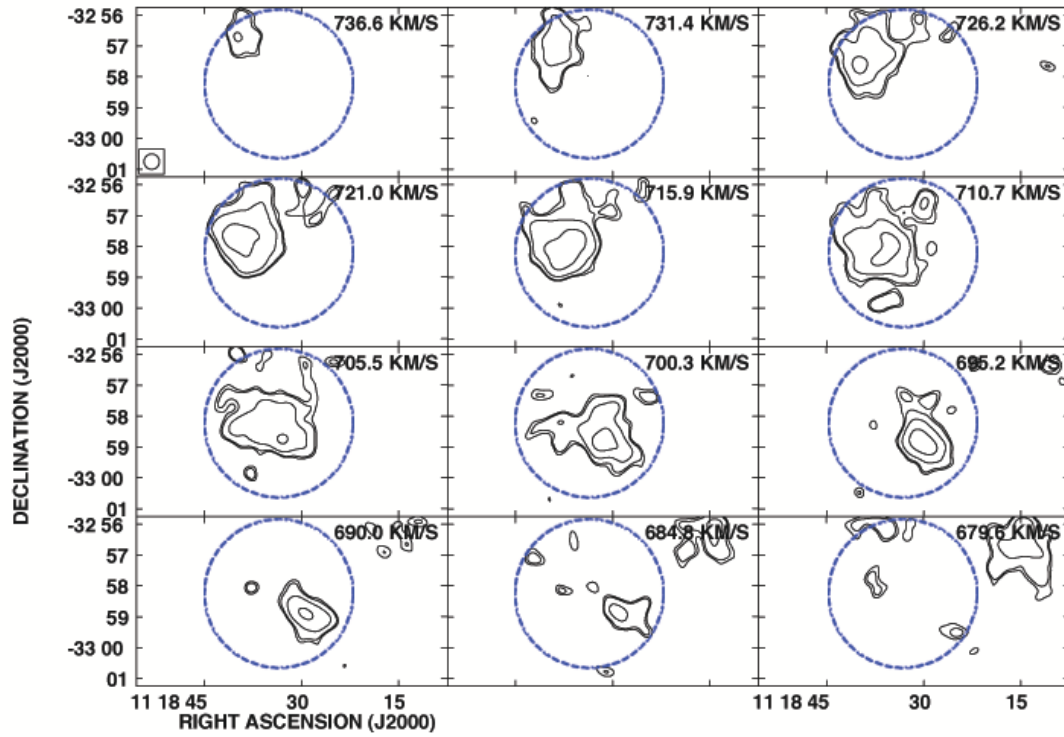


Figure 3.10: Contour maps on the channels where the HVC candidate in NGC 3621 is visible. The beam has been convolved to a 30'' beam. See Fig 3.7 for details.

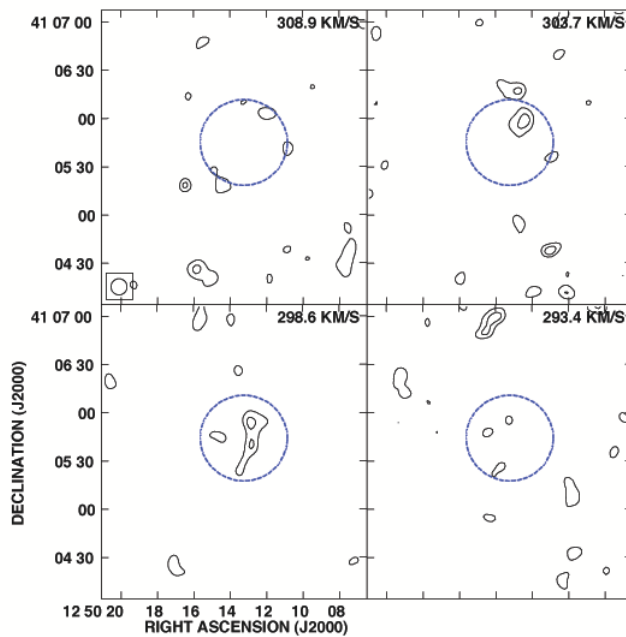


Figure 3.11: Contour maps on the channels where the HVC candidate in NGC 4736 is visible. See Fig 3.7 for details.

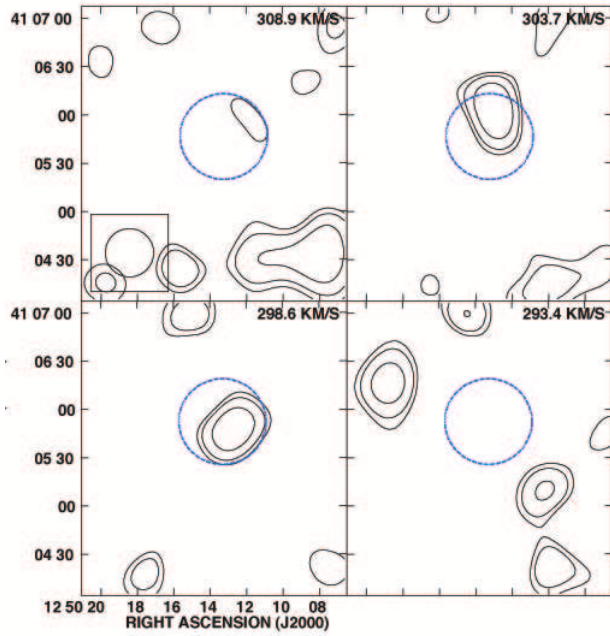


Figure 3.12: Contour maps on the channels where the HVC candidate in NGC 4736 is visible. The beam has been convolved to a $30''$ beam. See Fig 3.7 for details.

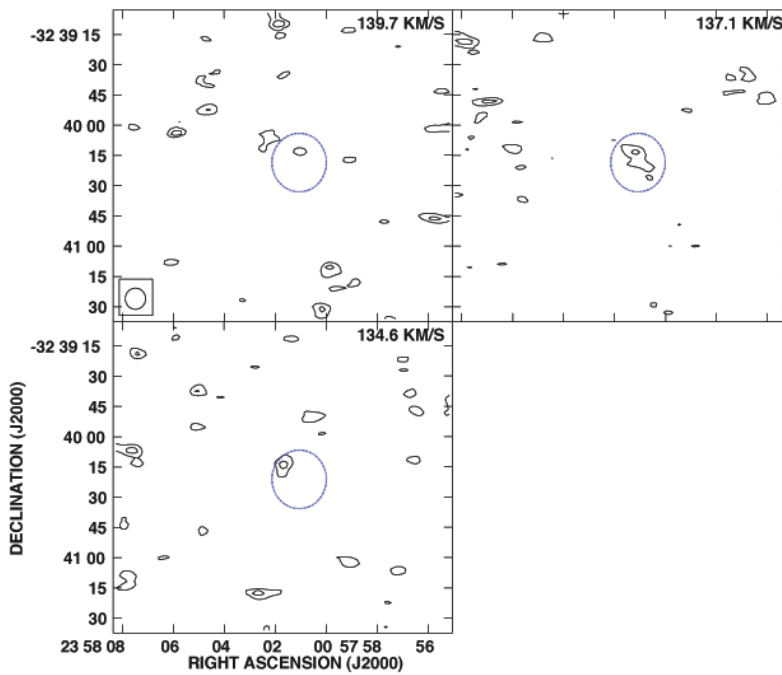


Figure 3.13: Contour maps on the channels where the HVC candidate in NGC 7793 is visible. See Fig 3.7 for details.

HVC Candidate	Mass	Projected distance	Velocity offset
-	M_{\odot}	kpc	km s^{-1}
NGC 2841	2,68E+06	52.25	70
NGC 3198	9,07E+05	16.98	42
NGC 3621	7,96E+07	18.17	30
NGC 4736	5,10E+05	11.84	18
NGC 7793	1,40E+05	6.47	97

Table 3.4: Mass estimates for the HVC candidates, their projected distances with respect to their parent galaxies, and the velocity offset from the systemic velocity of their parent galaxies.

The results are presented in Table 3.4, where for the cases of NGC 3198, NGC 4736 and NGC 7793 we show upper limits. The spectrum for the candidate in NGC 2841 is shown in Fig. 3.5.

3.4 Discussion

3.4.1 HVCs in and outside our Galaxy

In the literature, a distinction has been made between different sizes of HVCs in our Galaxy. Compact high velocity clouds (CHVC) are isolated objects, not connected to extended emission features, and usually have column densities around $N_{\text{HI}} \geq 1.5 \times 10^{18} \text{ cm}^{-2}$. Their median angular size is of less than 2° (Braun & Burton 1999). Large diffuse HVCs are more extended objects, also known as complexes, that cover several degrees on the sky. The most prominent of them are Complex A ($\sim 1200 \text{ deg}^2$), Complex C ($\sim 1600 \text{ deg}^2$), and Complex H ($\sim 478 \text{ deg}^2$). The Magellanic Stream is also considered one of these big HVCs in our Galaxy ($\sim 1000 \text{ deg}^2$), although it is well accepted that its origin is the result of the interaction between the Milky Way and the Magellanic Clouds.

Due to the extension of these HVCs, their column densities can vary widely from $\sim 2 \times 10^{17} \text{ cm}^{-2}$ to 10^{19} cm^{-2} , with some peak core densities that reach 10^{20} cm^{-2} to 10^{21} cm^{-2} . Thirty percent of high velocity gas will have $N_{\text{HI}} > 7 \times 10^{17} \text{ cm}^{-2}$, while 15% will have $N_{\text{HI}} > 2 \times 10^{18} \text{ cm}^{-2}$ (Wakker 2004). Of these HVCs, the very diffuse ones will never be detected outside our Galaxy with the telescopes that exist today due to sensitivity limitations. We will have to wait for more powerful telescopes to come on line before any detections can be done on diffuse HVCs in other galaxies. CHVCs are also unlikely to be detected in external galaxies due to resolution limitations. In the meantime, we can only focus our attention on the biggest and densest clouds. Complex C and Complex H are good examples of the kind of clouds we could possibly detect in other galaxies, as they cover a wide area on the sky (1600 deg^2 and 478 deg^2 , respectively) and have relatively large peak column densities ($\sim 10^{20} \text{ cm}^{-2}$). In the next Section we will discuss how much of these complexes could we possibly detect with our present telescopes.

3.4.2 Can we detect Galactic HVC Complex C in THINGS?

If we calculate the fraction of an HVC in our Galaxy that we could detect with the VLA near any of the THINGS galaxies, then Complex C would be a good example, for it is one

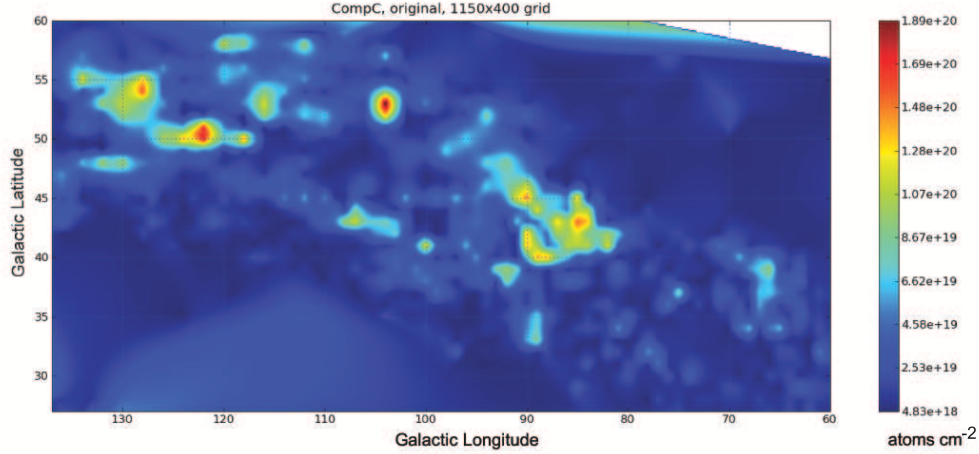


Figure 3.14: Map of Complex C as it would look like with the VLA beam when placed on galaxy NGC 1569.

of the most massive HVCs in our Galaxy and has a higher probability of being detected. But other HVCs in our Galaxy, like complex A, have even higher column densities. The sizes of the dense cores of complex A are comparable to those of Complex C, but the big total size of Complex C increases the resolution probabilities of our telescope. So in order to increase our chances of detection, we used the column densities given by Hulsbosch & Wakker (1988) for Complex C, multiplied by a factor of 2, which still gives us a realistic assumption for column densities. Then we take the values of two of the THINGS galaxies, NGC 1569, which is the closest one of the survey, with a distance of 1.95 Mpc, and NGC 7331, which is the furthest one, with a distance of 14.72 Mpc.

NGC 1569 has $\sigma=0.95 \text{ mJy beam}^{-1}$, where σ is the rms noise for any given channel, and $\Delta v=2.6 \text{ km s}^{-1}$, where Δv is the average channel width. The minimum column density detected at this galaxy is $\sim 8.18 \times 10^{19} \text{ cm}^{-2}$, which is at the upper range of column densities for Galactic HVCs. Complex C measures around 50° long, has a mass of $4.9 \times 10^6 M_\odot$ and is at a distance from the Milky Way disk of 10 kpc (Thom et al. 2008). If we now take the complex and place it at the distance of NGC 1569, it would then measure $15.38'$ long. In order to calculate the area that can be observed and the corresponding mass, we used the table given by Hulsbosch & Wakker (1988) for the complex. The table is based on observations made by Aad Hulsbosch in the period 1978-1986, using the Dwingeloo telescope. The survey had a $36'$ beam and a $1 \times 1^\circ$ (l, b) grid. If at 10 kpc the grid had a pixel size of 1° , then at 1.95 Mpc this would correspond to a pixel size of $18.45''$. Since our beam size is $10''$, Complex C could, in principle, be resolved.

Using these values, around 66 deg^2 of the complex would have at least our minimum column density, which corresponds to only 4% of the total complex. This corresponds to a mass of $\sim 1.31 \times 10^6 M_\odot$, or around $\sim 26\%$ of the total mass of Complex C. The rest would fall below our detection limits.

On the other hand, NGC 7331 has $\sigma=0.57 \text{ mJy beam}^{-1}$, and $\Delta v=5.2 \text{ km s}^{-1}$. The minimum column density detected in this case is $\sim 9.82 \times 10^{19} \text{ cm}^{-2}$, which is also at the upper range of column densities for Galactic HVCs. If we place Complex C at the distance

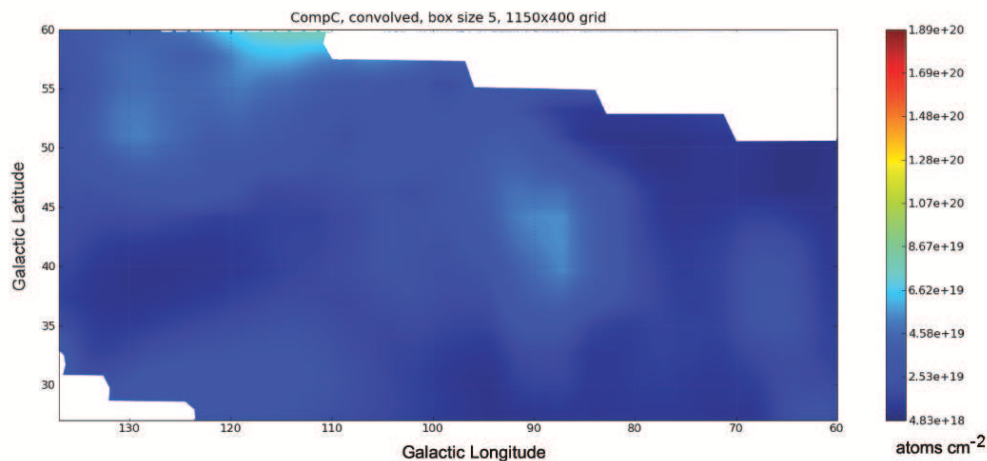


Figure 3.15: Smoothed map of Complex C as it would look like with the VLA beam when placed on galaxy NGC 7331.

of this galaxy, we would be able to see it having a longitude of $2'$ and in the Dwingeloo observations it would have a pixel size of $2.44''$. But the beam size of the VLA is $10''$, which means we would have to convolve the map of Complex C to the approximate size of the VLA beam in order to be able to compare properly. To do this, I applied a boxcar of 5 (see Appendix B for a view of the program used) to the column densities of the data given by Hulsbosch & Wakker (1988), which would give us a beam of $12.2''$. The resulting image can be seen in Fig. 3.15. Once the data was convolved, I calculated the area that would have the minimum column density detected at this distance, and found that the complete complex would fall below the detection limit. It must be noted that smoothing a peak in a map can have a strong effect if the peak is unresolved by the beam, since it will decrease substantially. This is probably the case for the hypothetical Complex C analogue in NGC 7331, which can barely be resolved and the column density peaks of which have dropped so far that they cannot be detected by the VLA.

3.4.3 Expected and actual HVC detections in the THINGS galaxies

If I take an average value between detections in close and far galaxies, we could roughly say that we could see around 3% of its mass. This would mean that I would be able to detect one big and massive HVC out of 33 HVCs. In other words, if I assume that a galaxy has around 1 very large and massive HVC in order to make it similar to our Galaxy, I would detect one HVC in every 33rd galaxy that I observe. This is of course a pure probability estimate.

Among the 33 THINGS galaxies, I have found one candidate that fits well to our conditions, and 3 candidates that fall at the limit of our detection criteria. Strangely enough, the positive candidate lies at one of the furthest distances of the THINGS survey (14.1 Mpc), and since an object like our analogue of Complex C can probably not be detected at this distance, we might assume that this object has an even bigger size than this complex, perhaps it could be some kind of tidal debris like the Magellanic Stream. Two of the other

candidates lie at small distances (NGC 4736 and NGC 7793 at 4.56 and 3.82 Mpc respectively), and one at a larger distance (NGC 3198 at 13.8 Mpc). The candidate in NGC 3621 seems to be a dwarf spiral galaxy because of its velocity field and velocity dispersion.

If we only take into account our positive detection, then we have found 1 big HVC out of 33 galaxies, which is what we would have expected. But it would still seem strange that we did not find it in a more local galaxy from our sample. A possible implication might be that big complexes are not so common in other galaxies, or that our observations are still not good enough to detect them. Another possible explanation might be that most of the big complexes in our Galaxy are the result of tidal debris or interactions with other dwarf or satellite galaxies, while most of the galaxies in our sample are isolated galaxies and therefore lack these interactions. If we do take into account our other three detections, then they are higher than the number that we expected to find and the implications would be completely different. We could then say that big and massive HVCs are more common than we thought and maybe our Galaxy is poor in big HVCs after all. Another possibility is that what we detected are not quite HVCs, but maybe bigger systems, perhaps dwarf galaxies of which the Galaxy has none. But this seems unlikely for as we mentioned, most of the galaxies in THINGS seem to be isolated galaxies with hardly any companions.

Many explanations have been offered for the origin of HVCs in the Milky Way. The four main hypotheses include a Galactic Fountain model (Bregman et al. 1980), origin from the interaction of satellite galaxies with the Milky Way (Gardiner et al. 1996), condensed gas in the halo (Maller et al. 2004), and the primordial gas model which implies an extragalactic origin (Blitz et al. 1999). Determining which is the most likely origin of our candidates is not a trivial matter, but if some of the HVCs in the Milky Way are the same as the objects we find here, some guidelines could be used as we can see where the THINGS candidates are with respect to their parent galaxies.

Candidates with distances larger than 10 kpc above the galactic disk are unlikely to be produced by galactic fountains (de Avillez 2000). The same applies to very massive HVCs, for the biggest shells observed in the largest HII regions are of the order of $10^5 M_{\odot}$. Some of the most massive candidates could be gas streams from satellites that have interacted with their host galaxy. Others could be condensed gas in the halo when close to the disk (Peek et al. 2007). The furthest candidates could be extragalactic clouds of diverse origin, but without a metallicity measurement it is hard to be certain. It must also be noted that in most cases it is not trivial to measure absolute distances between clouds and parent galaxies and only projected distances can be inferred.

Even though the masses of our detections are not very large, comparing the structure that could be observed of Complex C if put at the distance of our targets, it is reasonable to conclude that HI clouds in other galaxies can have total masses of the order of $10^6 M_{\odot}$. It is evident that having a good linear resolution and a good sensitivity is primordial in order to be able to make any detections, but with the present telescopes, this is not attainable yet. With the promise of new instruments, like the Square Kilometer Array (known as the SKA), better measurements will be possible and our understanding of the cold gas of galaxies and that in their immediate surroundings will be significantly enhanced.

4

Theoretical Modelling of the Impact of HVCs with the Galactic Disk

4.1 Introduction

As we previously mentioned in Chapter 1, since the detection of the first high velocity clouds (HVCs) in the 1960s there has been considerable discussion about their origin. Two possible mechanisms have been proposed in the last 30 years. The first, known as the galactic fountain scenario, is based on supernova (SN) activity in galactic disks. It was based on the realization that there is a circulation of matter between the disk and the halo, as the shocked gas has too much energy to be held in the disk, but not enough to overcome the potential well of the Galaxy. Hence, matter escaping from the disk, rises into the halo where it cools, and condenses into clouds, which in turn rain back onto the disk (Shapiro and Field, 1976; Bregman, 1980; Kahn 1981; Shapiro and Benjamin, 1991; Kahn, 1994; de Avillez 2000; see also Avillez & Breitschwerdt 2005). Gas infall and particularly HVCs result from thermal instabilities in a hot gaseous halo that is continuously replenished with hot gas produced by SNe and stellar winds in the disk.

The second scenario, first suggested by Oort (1970), is that the infalling gas, in particular the HVCs, has an external origin being the leftovers of the building blocks of the local group. This view, which has gained support in the last decade, explains (1) the continuous star formation rate observed in the Milky Way for long periods of time and (2) the metallicity distribution observed in the disk. In fact, the latter item is explained by chemical evolution arguments that show the need for a continuous accretion of metal-poor gas, throughout the disk lifetime, to explain the discrepancy between the observed stellar metallicity distribution in the solar neighbourhood and that predicted by closed-box models of chemical evolution.

Regarding point (1), detailed studies within the Galaxy show that there have been periods of considerable enhancement of the star formation rate, with durations of order a few hundred million to a billion years. This is known from star counts in the relatively close neighbourhood of the Sun, but from basic stellar dynamics it is also known that these enhancements must have occurred over quite a large part of the Galaxy disk at the same time. Therefore, the rate of star formation is expected to be constant for long periods of

time.

Such a widely distributed enhancement appears to be compatible only with the dynamical effect resulting from the arrival of a large diffuse HVC. This would trigger star formation in the plane by compressing gas over a wide area, and eventually it would act by compressing clouds which are already in equilibrium but just on the edge of the conditions for star formation. Analytical studies have been done with respect to this subject, and the impact of HVCs with the Galactic disk has been modelled by several authors (Cómeron & Torra 1992; Avillez 1999; Quilis et al. 2001). In Section 4.2 we present a brief review of them, and some relevant information about each of the simulations can be found in Table 4.1. But such analytical studies are done with very simplistic models of the interstellar medium, and are not accompanied by a numerical study. It is quite clear that an analytical treatment of this interaction can inevitably be followed only at a first order. The nature of such an interaction is completely non-linear, and in order to do a higher order analysis it is necessary to follow the evolution of the system in a numerical way.

With the purpose of studying the complicated interaction of a cloud with the Galactic disk, we pretend to divide our work in two parts. In the first part we will make an analysis of linear perturbations in the disk-cloud system with the intention of following the interaction in an analytic way. This will give a first order idea of the results of such a collision in a realistic context that can be used to guide future numerical simulations. The second part will include the simulations, which is part of our future work.

In Section 4.3, we will discuss the dynamics of a HVC falling into the galactic disk, following Kahn & Brett's paper (1993), and in Section 4.4, we will make a linear analysis of the disk-cloud interaction. In the analysis that we present in Section 4.4, we pretend to follow a gas element in its journey towards the galactic atmosphere, and its trajectory perturbation when it falls into the disk. A next step in the refinement of this analysis will be to consider the magnetized interstellar medium and perform yet another linear stability analysis. In summary, our analytical treatment will illustrate or reflect the main conditions of the interstellar medium like rotation, thickness of the disk, and the inclusion of magnetic fields.

The analysis of the disk stability under these conditions will provide us with an insight on whether or not the cloud-disk interaction can result in a gravitational instability and how it will modify the Jeans criterion, thus enabling the possibility of star formation and the conditions under which it will proceed. These analyses will also provide us with mathematical expressions that account for modifications to the Jeans criterion, according to the physics taken into consideration.

4.2 A Review of Numerical Simulations of HVCs

4.2.1 Hydrodynamical Simulations

Hydrodynamical simulations done by Lépine & Duvert (1994) showed the interaction of an oblique cloud with the Galactic disk and its effects on creating star-forming regions. Their main result is that such impact triggers the star formation process and that the distribution of the OB associations resulting from the impact appear to be consistent with the observed locations of those associations.

Quilis et al. (2001) used a 3D hydro-code based on high-resolution shock-capturing techniques, which was designed to simulate the evolution of an asymmetric three-dimensional distribution of gas, to investigate the interaction between the interstellar medium (ISM) and both dark matter-dominated HVCs and pure gas clouds that might be interacting with the Galactic disk as a result of a Galactic fountain. The pure gas HVCs are initially in pressure equilibrium with the external hot medium, while the dark matter-dominated clouds have an additional potential field to maintain their dynamical equilibrium. Quilis et al. (2001) used a fixed grid with ratio of sides 2 : 1 : 1 where wind is blowing down along the long axis, where the HVCs have no internal structure. The box had a size of $12 \times 12 \times 24$ kpc, with a number of cells of $128 \times 128 \times 256$, and with a numerical resolution of 90 pc. The density of the external medium was varied from 10^{-3} to 10^{-6} cm^{-3} , and the temperature of the external medium was varied from 10^6 to 10^4 K. The cloud velocities varied from 170 to 400 km s^{-1} .

As a result, Quilis et al. (2001) see that a weak bow shock is forming in front of the cloud when it penetrates the intergalactic medium, and increases its local temperature. The neutral gas found at the front edge of the HVC is compressed and heated, while a region of low pressure is created immediately behind the cloud, and when the wind is dense enough, trails of stripped HI are created.

Kudos & Basu (2004) performed hydrodynamic (HD) simulations of a HVC crossing the Galactic midplane with the aim of comparing the results with the mushroom-shaped structure of the Galactic worm GW 123.4-1.5. They assumed the ISM as an adiabatic gas and axial symmetry in cylindrical coordinates. The cloud has a density of 1 cm^{-3} , which is the same density as the cold (and therefore densest) layer of gas in the Galaxy and an initial velocity of 100 and 50 km s^{-1} . The minimum grid size used was of 1.4 pc. The computational region was of 1400×2100 pc.

As the cloud impacted the Galactic plane, it was decelerated by the gravity and was broken by eddies of the hot gas flow generated behind the cloud. This broken cloud is the one Kudos & Basu (2004) claimed formed a cap of mushroom-shaped structure. There was also a small structure formed on the opposite side of the plane because of Kelvin-Helmholtz instabilities. When the velocity of the cloud was 50 km s^{-1} , the results were similar, only that the mushroom was smaller. The dynamical timescale for this structure is around 10^7 years. These results are to be expected with the HVC densities they chose, but observations have shown that HVC densities are considerably lower than that of the cold gas layer of the Galaxy (Wakker & van Woerden 1991, Lockman 2003), which implies that their results will need to be reconsidered.

4.2.2 Magnetohydrodynamical Simulations

Cómeron & Torra (1992) followed the collision process of a HVC with the Galactic disk with 2D HD simulations. The computational grid box used by them is divided in 128×128 cells, with a cell size of a few tens of parsecs. The cloud travels at a velocity of 100 km s^{-1} , with angles of incidence with the Galactic plane of 0 and 45° , has a length of 500 pc, and a density of $10^{-2} M_\odot \text{ pc}^{-3}$, which corresponds to .44 particles cm^{-3} (the cloud is assumed to have a constant density). As a result, they obtain a shocked region where temperature and density increase and ionization takes place. This region starts to cool down as time runs, and a

dense, cold neutral layer results a few thousand years after the collision. The difference between the head-on collision and the oblique collision is the material that escapes. In the oblique collision the material entering the shock has a parallel velocity component to the shock surface, and there is an appreciable flow of compressed material that escapes the shocked layer, while this does not occur in the head-on collision. They compare this study to the origin of the Gould Belt and some of its associated structures, which may be explained by this mechanism if we assume that the shocks are stopped by the drag force from the Galactic disk gas and the gravitational force from the stellar disk, when the cloud is several hundred parsecs below the Galactic plane.

Later on, C  meron & Torra complemented their study with another paper (1994), where they deal with an oblique collision of three different HVCs varying in size, and thus in mass and column densities, and study the apparition of bound complexes from gravitational instabilities in the process. The initial conditions of their galactic disk are mainly the same as the ones in their 1992 paper, but with some modifications on the vertical structure of the magnetic field and the addition of a hot halo component on the Galactic ISM. As for the HVCs, their initial temperature is the same as in the previous paper, with a $T \simeq 40$ K, and with masses of $3.3 \cdot 10^6$, $3 \cdot 10^5$, and $3.3 \cdot 10^4$ solar masses, with lengths of 1700, 500, and 170 pc, respectively. Their results show that magnetic fields allow the growth of gravitational instabilities in the complexes formed through the path of the post-shocked layer of the HVC. This might lead to star formation in a rotating disk even with the shearing effect of the rotation at heights below 100 pc, where the growth time becomes of the order of the shearing time. C  meron & Torra (1994) also suggest that their model is in good correspondence with the main complexes of the Gould Belt.

Rand & Stone (1996) performed 3D HD and MHD (ZEUS 3D) simulations of the impact of a HVC with the edge-on galaxy NGC 4631. The Cartesian grid used had a computational domain of size $64 \times 128 \times 128$ zones, and various values of the adiabatic index γ were considered to approximate the effect of radiative cooling (γ equal to 1, 1.2, and 5/3). All the boundary conditions were periodic. They used a HVC with a size of 500pc and a cloud density of $\rho_c = .95 \text{ atoms cm}^{-3}$, a mass of $1.2 \times 10^7 M_\odot$, and an initial velocity of 200 km s⁻¹. The cloud moved with an inclined impact trajectory of 45  . Their results show that the cloud evacuated a cavity in the disk (diameter of 2.2 kpc) and swept $\sim 10^8 M_\odot$ of ambient material into a thin shell, which Rand & Stone (1996) compared to a supershell observed in the galaxy. The MHD simulations showed that the magnetic tension forces are insufficient to modify the morphology of the shell. They did not include self-gravity so were not able to see if the swept up material was subject to gravitational fragmentation, which would possibly lead to the triggering of star formation, but they could do an analytical treatment which showed it was reasonable to expect fragmentation and triggered star formation in the shell. They also note that by increasing the kinetic energy of the HVC, the shells produced are substantially larger, and increasing the linear momentum of the HVC causes the cloud to punch through the disk, creating structures extended along the trajectory of the cloud.

Simulations done by Avillez (1999) show the interaction process of clouds with the Galactic disk as a natural process resulting from a large-scale disk-halo-disk cycle - a Galactic fountain - where the disk gas flows away into the halo, cools and returns to the disk. He used a previous version of the now 3D   vora-Vienna Astrophysics Fluid-Parallel AMR (EVAF-PAMR) Code. It is a Fortran 95 code that solves HD and MHD problems with

AMR (Pember et al. 1996; Balsara 2001) in a parallel fashion and uses approximate Riemann solvers for the hydro and magnetic components (Collela & Woodward 1984; Dai & Woodward 1994, 1998). Avillez (1999) used a vertical mass distribution (Avillez et al. 1997) for the disk with the form:

$$\rho_* = \rho_{*,0} \sec h^2 \left[(2\pi G \beta_* \rho_*)^{1/2} z \right] \quad (4.1)$$

where z varies between -100 pc and 100 pc, $\rho_{*,0} = 3.0 \times 10^{-24}$ g cm $^{-3}$ is the mass density contributed by Population I stars near the Galactic plane (Allen 1991) and the constant $\beta_* = 1.9 \times 10^{-13}$ cm $^{-2}$ s 2 , with a local gravitational potential, Φ , of the form

$$\Phi = -\frac{2}{\beta_*} \ln \cosh \left[(2\pi G \beta_* \rho_*)^{1/2} z \right] \quad (4.2)$$

The disk gas is driven by SNe types Ib, Ic and II with the observed Galactic SN rates (Cappellaro et al. 1999). The equations of evolution are solved by means of a 3D hydrodynamical scheme using the piecewise parabolic method (Collela & Woodward 1984) and the adapted mesh refinement algorithm of Berger & Collela (1989).

Avillez et al. (1999) centred the simulations on the Galactic plane, having an area of 1 kpc^2 and extending 4 kpc on either side of the Galactic midplane. He used runs with grid resolutions of 5 pc and 10 pc in the disk regions of $-270 \leq z \leq 270 \text{ pc}$, and $z \leq -250 \text{ pc}$ and $z \geq +250 \text{ pc}$, respectively. The boundary conditions are periodic along the vertical axis, and outflow in the upper and lower parts of the grid parallel to the Galactic plane. His results show that as the hot gas produced by the SNe rises into the halo, it cools and condenses into clouds of varying sizes (from a few parsecs to tens and hundreds of parsecs) which rain back into the Galactic disk interacting with the hot gas present in the region where they are, as well as with hot gas moving upwards engulfing them. The clouds are classified according to their sizes and velocities into low, intermediate, high and very high velocity clouds, and have a multiphase structure, where the core of the cloud is formed by cold gas ($T \leq 10^4 \text{ K}$), surrounded by warmer gas with temperatures of 10^4 K . They are embedded in a hot medium with temperatures greater than or equal to 10^5 K .

In order to study the interaction of a general HVC with the gaseous disk, Santillan et al. (1999) performed 2D simulations employing the MHD code ZEUS 3D. They set up a disk in magnetohydrostatic equilibrium, with a plane-parallel magnetic configuration and a HVC which is injected into the medium at different angles. Using an effective temperature of $\approx 11,000 \text{ K}$ for the medium and a strength of $\approx 5 \mu\text{G}$ for the field magnetic on the plane, the parameters that were varied in this experiment were the angle of impact, which was in the range ($0^\circ, 60^\circ$), and the height at which the cloud was injected, which was varied between $350\text{-}405 \text{ pc}$. Their main result is that the HVC was prevented from penetrating the galactic gaseous disk and could even bounce back. This effect turned out to be one associated with the dimensionality of the problem. With new simulations they carried out in 3D (Santillan et al. 2003) using the same plane-parallel magnetic configuration, their results were different and the HVC penetrated the galactic atmosphere all the way down to the disk. This effect is due to the fact that in 3D the magnetic field lines have another degree of freedom and can slide past one another instead of building up pressure and magnetic tension.

Further work done by Konz et al. (2002), shows 2D MHD simulations of a HVC moving through a hot magnetized ambient plasma, where the formation of the comet-like head-tail structure of the HVC is formed due to their magnetic field which they argue forms a magnetic barrier that exerts a stabilizing pressure on the cloud and hinders hot plasma from diffusing into the cloud. Here they used parameters of HVCs in the Magellanic Stream, with a cloud size of 100 pc and a volume density of $\rho_c = 10^{-3}$ atoms cm^{-3} . The cloud is initially at rest. The temperature profile for the cloud is given by $T(r) = p_{n0}/\rho_n(r)$. This means that the neutral gas outside the cloud is about a factor 25 hotter than that at the center of the cloud, which they argue does not agree with realistic temperature gradients. Simulations with steeper gradients in the temperature and the density of the neutral gas component have shown qualitatively the same evolution of the system, apart from the longer calculation time.

In Santillan et al. (2004) new simulations were presented with very similar initial conditions as in their previous works (see Santillan et al. 1999, 2001). The cube has 3 kpc per side and they use an isothermal equation of state. The cloud is a sphere, whose size is not specified in the paper, but starts at a height of ~ 2.5 kpc, with a density of $n_{\text{HVC}} = 0.1 \text{ cm}^{-3}$ and a velocity of $v_{\text{HVC}} = 100 \text{ km s}^{-1}$, which, they say, corresponds to an injected mass to the disk of $M_{\text{HVC}} = 4 \times 10^6 M_{\odot}$, and an injected energy of $E_{\text{HVC}} = 10^{53}$ ergs. Their results show the formation of a thin supershell in the Galactic plane after the collision of a cloud with the magnetized gaseous disk, whose thickness depends on the initial parameters of the magnetic field itself (magnitude and topology). The material behind the shocked HVC begins to expand along the compressed field lines, accumulating material and forming the shell. Further study on the subject lead them to perform 2D MHD numerical experiments (Santillan et al. 2007) to investigate the effects of continuing infall of clumpy gas in the extended HI galactic disk. They used a galactocentric distance of 20 kpc, with a cloud velocity of 100 km s^{-1} , starting at a disk height of 2 kpc, with a density of 0.1 cm^{-3} and a radius of 50 pc, and a kinetic energy of $\sim 10^{50}$ ergs. The injection rate of clouds into the box domain is 300 Gyr^{-1} . As a result, clouds interacting with the ambient medium are diluted, mixing with the turbulent disk at a height of 500 pc. But as they fall, they perturb the disk through MHD waves, producing a network of plumes and shells, and arising rms velocities of $3\text{-}8 \text{ km}^{-1}$ in the warm phase of HI, thus suggesting that the outer disk is being rained on by Galactic fountain material driven by inner star bursts or matter circulation in the halo.

4.2.3 Smooth Particle Hydrodynamics Tree Codes

Peek et al. (2008) did simulations with a TreeSPH code on galaxy formation which generated condensed clouds in the halo, accelerating and becoming more massive as they fell towards the disk, and compared their results to the extra-planar gas observed around the Andromeda galaxy. Their code followed the chemical evolution of 10 elements, and the algorithm included SNe of type Ia and II, and mass loss from stars of all masses. They also included radiative cooling depending on the metal abundance of the cloud and the meta-galactic UV field, as well as radiative transfer by switching off the UV field where the gas becomes optically thick to the Lyman limit photons. They started with 3.2×10^5 particles, with a circular velocity of 224 km s^{-1} at $z = 0$. Particles are split throughout

the simulation, and when they reach 8.6×10^5 gas particles, the warm/hot gas in the inner 100 kpc of the galaxy halo is then resolved with particles of mass $m_{\text{gas}} = 11700 M_{\odot}$, and a gravity softening length of 128 pc. By a time of 10.3 Gyr, more than 100 condensed halo clouds had been formed with distances less than 100 kpc from the Galactic center, and with a mass resolution of $3 \times 10^6 M_{\odot}$, giving an accretion rate of $0.2 M_{\odot}/\text{year}$. From their results, the authors conclude that the majority of HVCs are consistent with being infalling, condensed clouds that are a remnant of Galaxy formation.

4.2.4 Summary

The models discussed above used physical conditions of the impacting cloud and the gas disk derived from observations. In general the ISM is taken as not having any changes besides those resulting from the motion of the impacting cloud through it. However, the ISM is far from smooth and it is always under the effects of different kinds of phenomena such as blast waves, stellar winds, etc, to name a few. A realistic understanding of HI clouds impacting the Galactic disk relies on a good knowledge of the physical conditions of the disk, as well as on three-dimensional models, which may account at the same time for the presence of OB associations, runaway stars, disk-halo interaction through chimneys and Galactic fountains, formation of HI clouds in the halo and their return to the Galactic disk, that is, a dynamical disk.

Magnetic fields need also to be taken into account. In theoretical terms the field lines will be compressed and therefore, magnetic tension will act against compression received by HVCs on the Galactic disk, but this will depend on the curvature of the lines. Magnetic field lines in the Galaxy are tangled and inhomogeneous due to matter circulation between stars and the interstellar gas, and, in particular, the energy input by random and clustered SN explosions which induce shear flows. A huge thermal overpressure due to combined SN explosions can sweep the magnetic field into dense filaments and punch holes into the extended warm and ionized HI layers (Avillez & Breitschwerdt 2005). We will use these physical constraints in our future numerical simulations.

4.3 Dynamics of an infalling HVC

As we mentioned it before, there are two main scenarios to explain the origin of HVCs. In one of them the HVCs have a Galactic origin; clusters of SNe continually eject material to the Galactic atmosphere, it cools and then rains down upon the Galactic disk. In order to explore this scenario we will conduct some calculations on the mechanics of a cloud formed in this way, sheared and finally returning to the disk in the Galactic fountain scenario. We will follow Kahn & Brett's (1993, from now on KB) calculations. But we must highlight the fact that the downward trajectory of any HVC formed in this way, also applies to those HVCs which might have extragalactic origins.

In disk galaxies, particularly ours, rotation curves are essential tools for understanding how the Galaxy mass is distributed. Observations have shown that $v_r = \text{constant}$, where v_r would be the rotation velocity of the gas around the galactic center, which means that the rotation curve is flat. But if the gas is being driven by the Galaxy's potential, then we can suppose that it is in equilibrium. In this way we can probe the potential. In a

dynamical equilibrium state, the gas rotates and is attracted by the Galaxy, so we can use the condition of having the centrifugal force equal to the gravitational force, this is $v_r^2/r = GM(r)/r^2$, where if $v_r = \text{constant}$, we need $M(r) \propto r$. From this equation, we can deduce that if $M(r) = \mu r$ then

$$v_r^2 = G\mu$$

and since we have two contributions of mass in a galaxy, one from Population I (young stars, dust and gas) and one of Population II (high amount of low mass stars), we can define an average rotational velocity as

$$V \equiv v_r = \sqrt{2G\mu}.$$

For the young population the mass can be considered to be contained in a thin disk, so we can use cylindrical coordinates to denote the mass proportion with distance, which can be denoted as ϖ . We can then use the Poisson equation to calculate the potential. Since we are assuming symmetry with respect to the Galactic plane, we just consider the first component of the Laplacian in polar coordinates in order to obtain the potential, and the same for the Laplacian in cylindrical coordinates. Thus, we can write the Population II potential as

$$\frac{1}{\varpi^2} \frac{d}{d\varpi} \varpi^2 \frac{d\Phi_{II}}{d\varpi} = 4\pi G\mu\varpi / 4\pi\varpi^3 = \mu G / \varpi^2.$$

which implies that

$$\varpi^2 \frac{d\Phi_{II}}{d\varpi} = \mu G \varpi.$$

and dividing by ϖ^2 and integrating we find

$$\Phi_{II} = \mu G \log(\varpi).$$

If we recall how the average rotational velocity V was defined, then we can rewrite the last equation as

$$\Phi_{II} = \frac{V^2}{2} \log \frac{R_*}{r}$$

where we change the variable ϖ for R_*/r in order to evaluate the integral. And if we do the same with Population I we get

$$\Phi_I = \frac{V^2}{2} \left(\log \frac{R_*}{\varpi} - \sinh^{-1} \frac{z}{\varpi} \right).$$

The vertical component of the gravity is (see Appendix C)

$$-g_{\perp} = \frac{V^2}{2R_*}. \quad (4.3)$$

where R_* is the distance from the Sun to the Galactic center.

The energy of a particle in a gravitational field is simply its weight by its height with respect to the field. By applying this concept to calculate the energy of an object on

the Galaxy's atmosphere we have that its potential energy is given by the energy used to reach that height. In other words, an object shot upwards with an initial velocity v will reach a height Z once it has consumed all its kinetic energy. This can be written as $mg_{\perp}Z = 1/2mv_0^2$, where u_0 is the velocity in the plane of the object. So the object will reach a height

$$Z = u_0^2/2g_{\perp}. \quad (4.4)$$

If we have a Galactic atmosphere in one dimension with a fluid element originated from a SN going up at a velocity u because of its high temperature, it will reach a certain height where it will meet gas already there and gas coming down with a velocity w , a height z and a superficial density Σ . In order to study its movement we need to see what values are conserved, so we look first into the mass. In a stationary configuration we need to have the quantity of what's coming up also coming down, and the flux of the gas is defined as $\phi = \rho v$, so the rate at which the flux changes is the same as the mass coming up minus the mass coming down, so $\rho(u + w)$ = the rate at which the flux changes, since u and w have different signs, and since $\phi = \rho u$ then $\rho = \phi/u$. And since the flux change rate is equal to $d\Sigma/dt$, then

$$\frac{d}{dt}\Sigma w = \frac{\phi}{u}(u + w).$$

Now we look into the conservation equation, where we basically have $F = ma$, so ma is simply $d\Sigma w/dt$, and F is just the gravitational acceleration that is being affected by the flux, that is, the free fall is stopped by the ascending flux which results from the interaction of the object falling minus the one flowing up. Writing this with the second law of Newton gives us

$$\frac{d}{dt}\Sigma w = \Sigma g - \phi(u + w). \quad (4.5)$$

At this point we need a relation between u and w which can be obtained as follows. From the law of conservation of mass we can show that $w d\Sigma/du = \phi/g(u + w)$. If we integrate such a relation from the point to which the sheet is located to its maximum height we get

$$u + w = \frac{g \Sigma}{\phi 2}$$

which after rearranging says that $\Sigma = 2(u + w)\Phi/g$. Using this result on the mass conservation relation we obtain

$$w \frac{d}{du}(u + w) = \frac{1}{2}(u + w)$$

which can be solved for $dw = (u/2w - 1/2)du$. Once again we can integrate this equation from the present position of the sheet, z , to its maximum attainable height, z_{max} , with the result

$$w(z_{max}) - w(z) = (u^2(z_{max}) - u^2(z))/4w.$$

Finally, making use of the fact that $w(z_{\max}) = u(z_{\max}) = 0$ we get the relation between w and u , $w = u/2$. Inserting this relation on 4.5 and assuming a constant flux of matter

$$\Sigma g = \phi(u + w) = \phi(3/2u)$$

or

$$\Sigma = \frac{3\phi u}{2g},$$

and since $u = g\tau$

$$\Sigma = \frac{3\phi\tau}{2}, \quad (4.6)$$

which describes the upflow and downflow of the gas in the Galactic fountain, with a speed of descent of

$$w = |g_{\perp}| \tau/4. \quad (4.7)$$

But if we consider the flow flowing up and moving along the radius, then we need to calculate its orbit. The radial potential tells us that

$$g_{\varpi} = -\frac{V^2}{\varpi_0} + \frac{V^2}{\varpi_0} \left(\Pi + \frac{z}{2} \right), \quad (4.8)$$

where Π is the radial potential perturbation. Now we make two suppositions. The first one is that when the gas moves through the radius, it does it inside the galaxy, which is why the terms have opposite signs. The second one is that if we move a little bit in the radius, there is a potential change in z , which is half of the displacement in the radius. We now focus on the angular momentum which is defined as $r \times v$, where r is the position of a particle and v its velocity, but we are denoting position as ϖ so the angular momentum is $J = \varpi V$, and this vector points on the z direction. If we suppose that when the gas flows up the Galactic atmosphere, it does not change its radial direction, the change rate of the angular momentum in the gas layer with a mass Σ will be

$$\frac{d}{d\tau}(\Sigma J)$$

and since the angular momentum J is constant, its derivative is zero. But if we suppose that when the gas falls it moves in the radial direction, then it moves from ϖ to $\varpi_0 + \Pi$, where the subindex 0 implies the original distance from where the gas originated. Then we have

$$\frac{d}{d\tau}(\Sigma J) = \dot{\Sigma} V (\varpi_0 + \Pi).$$

Now we define the Lagrangian angular momentum, this is, the one that moves along with the fluid, as $j \equiv J - V\varpi_0$. We can now write the above equation in terms of j as

$$\frac{d}{d\tau}(\Sigma j) = \dot{\Sigma} V \Pi.$$

Since Σ is directly proportional to τ , we can substitute equation 4.6 in the previous one and cancel similar terms to obtain

$$\frac{d}{d\tau}(\tau j) = V\Pi. \quad (4.9)$$

When we perturb the orbit of an object that is orbiting the Galactic center, it makes epicycles with respect to its orbit, which is no more than a simple harmonic movement in the azimuthal and radial coordinates. In principle, gas expelled into the Galactic atmosphere would also move like this, so a good approximation of the movement of the gas layer in the radial direction could be given by the harmonic movement equation, with the small correction that our gas layer is accreting material that is expelled from the disk. If we call the mass that is being added to the gas layer f_{add} , then we can write

$$\frac{d^2\Pi}{d\tau^2} + \kappa^2\Pi = f_{\text{add}}, \quad (4.10)$$

where κ^2 is the epicyclic frequency.

But our gas layer will not move as an oscillator, this is just to give us an idea of how the orbit of our gas layer would be. We have to consider some things in order to understand how to treat the orbit of the gas element. To begin with, the gas moves in the radial direction by an amount Π , so when it gets closer to the Galactic center it accelerates, and this acceleration goes like $-\Delta V/\Delta t$, which in our case would be something like $-\dot{\Pi}/\tau$. Then, from Eq. 4.8 we can see that when it moves in a radial direction, the potential changes in ϖ and in z , so we should add that change of potential to our movement equation. When we move in radius the centrifugal force also changes, and modifies the value of V^2/ϖ^2 to $V^2/(\varpi + \Delta\varpi)$, if we expand the denominator by the binomial law and stay with the first terms, which is basically $V^2/\varpi_0(1 - \varpi/\varpi_0)$. If we rewrite this term as a function of J , we find that the change of the centrifugal force is $VJ/\varpi_0^2 - V\varpi/\varpi_0^2$, or writing it in terms of j we have Vj/ϖ_0^2 .

We now add this to Eq. 4.10 and get

$$\frac{d^2\Pi}{d\tau^2} + \frac{1}{\tau} \frac{d\Pi}{d\tau} + \kappa^2\Pi = \frac{V^2 z}{2\varpi_0^2} + \frac{2Vj}{\varpi_0^2}. \quad (4.11)$$

We can now calculate the vertical coordinate z using the speed of descend w . We first integrate from a height z where our element is, up to a reference height Z , which is the maximum height the gas element can reach. Then

$$\int_z^Z w d\tau = \int g_{\perp} \tau / 4 d\tau$$

which simply gives us

$$z = Z - \frac{1}{8} g_{\perp} \tau^2 = Z - \frac{V^2 \tau^2}{16\varpi_0}, \quad (4.12)$$

where we use Eq. C.2 (see Appendix C) for g_{\perp} .

If we now use the value of Π in Eq. 4.9 and the new value for z , and we substitute it in Eq. 4.11, then we get

$$\frac{d^2}{d\tau^2} \frac{1}{V} \frac{d}{d\tau} \tau j + \frac{1}{\tau} \frac{d}{d\tau} \frac{1}{V} \frac{d\tau j}{d\tau} + \frac{\kappa^2}{V} \frac{d}{d\tau} \tau j = \frac{V^2}{2\omega_0^2} (Z - V^2\tau^2/16\omega_0^2) + \frac{2Vj}{\omega_0^2}$$

and solving it we have

$$\frac{1}{V} \left(3 \frac{d^2 j}{d\tau^2} + \tau \frac{d^3 j}{d\tau^3} \right) + \frac{1}{V} \frac{d^2 j}{d\tau^2} + \frac{1}{V\tau} \frac{dj}{d\tau} + \frac{j}{\tau V} + \frac{\kappa^2 \tau}{V} \frac{dj}{d\tau} + \frac{j\kappa^2}{V} - \frac{2Vj}{\omega_0^2} = \frac{ZV^2}{2\omega_0} - \frac{V^4\tau^2}{32\omega_0^2}.$$

If we rearrange this expression and group common terms, multiply by V and divide by τ , this is reduced to

$$\frac{d^3 j}{d\tau^3} + 4/\tau^2 \frac{d^2 j}{d\tau^2} + \frac{dj}{d\tau} \left(\frac{2}{\tau^2} + \kappa^2 \right) + j \left(\frac{\kappa^2}{\tau} - \frac{2V^2}{\omega_0\tau} \right) = \frac{ZV^3}{2\omega_0^2\tau} - \frac{V^5\tau}{32\omega_0^3}.$$

Finally, the epicyclic frequency is defined as $\kappa^2 = 2V^2/\omega_0^2$, so we substitute this definition in the term that linearly depends on j , and this term becomes zero, so we are left with the relation

$$\frac{d^3 j}{d\tau^3} + 4/\tau^2 \frac{d^2 j}{d\tau^2} + \frac{dj}{d\tau} \left(\frac{2}{\tau^2} + \kappa^2 \right) = \frac{ZV^3}{2\omega_0^2\tau} - \frac{V^5\tau}{32\omega_0^3}. \quad (4.13)$$

The solution for this equation is:

$$\tau \frac{dj}{d\tau} = \frac{VZ}{4} + \frac{a}{\tau} \sin(\kappa\tau - \epsilon) - \frac{\omega_0^2(\kappa^3\tau^2 - 6\kappa)}{128\sqrt{2}}. \quad (4.14)$$

This new equation has two parameters, a and ϵ . To find them we impose boundary conditions. For example, at a time $\tau = 0$, that is, when a gas element begins to fall, we know that the velocity is completely vertical, since we supposed that the gas flows up without a radial component in its velocity. Then, if $\tau = 0$ we can make the radial component of velocity equal to zero and find our parameters. Since the radial component of the displacement of our gas element is Π , this is reduced to

$$0 = \frac{d\Pi}{d\tau} = \frac{1}{V} \frac{d^2}{d\tau^2} (\tau j). \quad (4.15)$$

We just substituted Eq. 4.9 in the definition of radial velocity. The terms that depend on τ in Eq. 4.14 become zero, and since the limit when τ tends to zero in $\sin(\kappa a\tau)/\tau$ is κa , then Eq. 4.14, for $\tau = 0$, reduces to the following when $\epsilon = 0$:

$$0 = \frac{VZ}{4} + \kappa a + \frac{3\kappa\omega_0^2}{64\sqrt{2}}. \quad (4.16)$$

If we substitute our definition $\kappa^2 = 2V^2/\omega_0^2$ in the above equation, we get

$$\kappa a = -\frac{V}{4} \left(Z + \frac{3\omega_0}{16} \right).$$

and if we substitute this in Eq. 4.14 we get

$$\tau \frac{dj}{d\tau} = \frac{V}{4} \left(Z + \frac{3\varpi_0}{16} \right) \left(1 - \frac{\sin \kappa\tau}{\kappa\tau} \right) - \frac{V\varpi_0}{128} \kappa^2 \tau^2.$$

Then we make a Taylor series expansion for $\sin \kappa\tau$ and get

$$\tau \frac{dj}{d\tau} = \frac{VZ}{24} \kappa^2 \tau^2 - \frac{V}{4} \left(Z + \frac{3\varpi_0}{16} \right) \sum_{n=2}^{\infty} \frac{(-1)^n (\kappa\tau)^{2n}}{(2n+1)}. \quad (4.17)$$

Eq. 4.7 tells us the velocity at which the gas element flows downwards, so we now use it instead of w , but in terms of the velocity at which the gas flows up, u , and then we work out the value of τ and use Eq. C.1 (see Appendix C) to substitute the value of g_{\perp} :

$$\tau = \frac{4 * w}{g_{\perp}} = \frac{4u/2}{V^2/2\varpi} = \frac{4u\varpi}{V^2}.$$

If we now use Eqs. C.1 and 4.4, we can write out this equation in terms of the height at which the gas element falls, Z . So we call the time at which the gas element touches the Galactic plane τ_1 . Then

$$\tau = \tau_1 = \frac{4\varpi_0 u_0}{V^2} = \frac{4(Z\varpi_0)^{1/2}}{V}. \quad (4.18)$$

If we use the following definition: $\kappa = V\sqrt{2}/\varpi_0$, then we can use the previous equation to calculate that

$$\kappa^2 \tau^2 = \frac{2V^2}{\varpi_0^2} \frac{16Z\varpi_0}{V^2} = \frac{32Z}{\varpi_0}.$$

If we suppose that the maximum altitude that the gas layer can reach is $Z = 3$ kpc with a galactocentric distance of $\varpi_0 = 8.5$ kpc, then the previous equation becomes

$$\kappa\tau_1 \approx 3.3. \quad (4.19)$$

Now we calculate an equation that will help us follow the trajectory of the gas element afterwards. In order to obtain these relations we first need to take Eq. 4.9 and divide it by $1/VZ$, so we get

$$\frac{\Pi}{Z} = \frac{1}{VZ} \frac{d(\tau j)}{d\tau}.$$

The last term of this equation can be calculated with the help of Eq. 4.17, which we calculate in Taylor series until $n=4$, to make sure we have a good convergence. But Eq. 4.17 is written in terms of $\tau dj/d\tau$ while this equation is in terms of the derivative of τj . So we first calculate the derivative of the product

$$\frac{d}{d\tau}(\tau j) = \tau \frac{d}{d\tau} j + j. \quad (4.20)$$

The first term of this relation, $\tau d/d\tau j$ is entirely given by Eq. 4.17, so we just need to calculate the j term. We can calculate it in terms of τ if we first divide Eq. 4.17 by τ and then we integrate over τ , and in this way we get

$$j = \int \frac{VZ}{24} \kappa^2 \tau - \frac{V}{4} \left(Z + \frac{3\varpi_0}{16} \right) \left(\frac{\kappa^4 \tau^3}{5!} - \frac{\kappa^6 \tau^5}{7!} + \frac{\kappa^8 \tau^7}{9!} \right) d\tau,$$

and integrating gives us

$$j = \frac{VZ}{2 \times 24} \kappa^2 \tau^2 - \frac{V}{4} \left(Z + \frac{3\varpi_0}{16} \right) \left(\frac{\kappa^4 \tau^4}{4 \times 5!} - \frac{\kappa^6 \tau^6}{6 \times 7!} + \frac{\kappa^8 \tau^8}{8 \times 9!} \right).$$

We can now calculate the right part of the relation of Π/Z , which gives us

$$\begin{aligned} \frac{\Pi}{Z} &= \frac{1}{VZ} \frac{d}{d\tau} (\tau j) = \frac{1}{VZ} (\tau d/d\tau j + j) = \frac{1}{24} \kappa^2 \tau^2 (1 + 1/2) - \frac{1}{4} \\ &\quad \left(1 + \frac{3\varpi_0}{16Z} \right) \left(\frac{\kappa^4 \tau^4}{5!} (1 + 1/4) - \frac{\kappa^6 \tau^6}{7!} (1 + 1/7) + \frac{\kappa^8 \tau^8}{9!} (1 + 1/8) \right), \end{aligned}$$

which then reduces to

$$\frac{\Pi}{Z} = \frac{1}{VZ} \frac{d(\tau j)}{d\tau} = \frac{\kappa^2 \tau^2}{24} - \frac{1}{4} \left(1 + \frac{3\varpi_0}{16Z} \right) \left[\frac{(\kappa\tau)^4}{4(4!)} - \frac{(\kappa\tau)^6}{6(6!)} + \frac{(\kappa\tau)^8}{8(8!)} \right]. \quad (4.21)$$

Another useful relation is obtained by combining Eqs. C.1 (see Appendix C) and 4.4 so that we get

$$Z = \frac{u_0^2 \varpi_0}{V^2}. \quad (4.22)$$

When we deduced Eq. 4.19 we calculated the product of $\kappa\tau_1 \approx 3.3$, and Eq. 4.13 is in terms of that product, so we could then calculate Π which is the displacement in the radius in the Galactic plane, from that equation. So according to Eq. 4.19

$$\frac{\Pi}{Z} = (\pi^2/16) - \frac{1}{4} \left(1 + \frac{(3 \times 8.5)}{16 \times 3} \right) \left(\frac{3.3^4}{4(4!)} - \frac{3.3^6}{6(6!)} + \frac{3.3^8}{8(8!)} \right) \approx 0.305$$

which tells us that the radial displacement of the gas element when coming down is

$$\Pi = 0.305Z$$

and if $Z = 3$ kpc, it would be around 0.9 kpc.

Now, a gas element should have an intrinsic angular velocity V/ϖ_0 , but while being adrift in the Galactic atmosphere its angular velocity changes by an amount of w , since its angular velocity is different while being closer or further away from the Galactic center. Then, if Ω is the angular velocity of a gas element in a given time, and remembering that $rV = J$, we have that

$$\Omega = \frac{V}{\varpi_0} + w = \frac{J_0 + j}{(\varpi_0 + \Pi)^2}.$$

We can expand this relationship in the following way: we first factorize ϖ_0 and then we use the binomial theorem as follows

$$\frac{1}{(\varpi_0 + \Pi)^2} = \frac{1}{\varpi_0^2(1 + \Pi/\varpi_0)^2} = \frac{(1 + \Pi/\varpi_0)^{-2}}{\varpi_0^2} = \frac{1}{\varpi_0^2}(1 - 2\Pi/\varpi_0 + \dots).$$

Substituting in the above equation we get

$$\Omega = \frac{V}{\varpi_0} + w = \frac{J_0}{\varpi_0^2} + \frac{j}{\varpi_0^2} - \frac{2\Pi J_0}{\varpi_0^3} + \dots \quad (4.23)$$

So we can now calculate the differential angular velocity which is simply

$$\Omega - \frac{V}{\varpi_0} \equiv w \equiv \frac{1}{\varpi_0^2}(j - 2V\Pi).$$

If we use Eq. 4.9 and factorize the term $\sqrt{\tau}$ we have that

$$\Omega - \frac{V}{\varpi_0} = \frac{1}{\varpi_0^2} \left(j - 2\frac{d\tau j}{d\tau} \right) = \frac{2\tau^{1/2}}{\varpi_0^2} \frac{d(j\tau^{1/2})}{d\tau}. \quad (4.24)$$

Now that we have all these relations we are ready to calculate the trajectory of the gas element, but instead of following it in the $r - Z$ plane, we are going to map in the Galactic plane and in a reference frame that rotates at an angular speed of V/ϖ_0 . In that case, the angular coordinate would simply be

$$\theta = \int w d\tau. \quad (4.25)$$

The derivative of this equation would then be w , but w is given by Eq. 4.24, so we just substitute and get

$$\frac{d\theta}{d\tau} = -\frac{2\tau^{1/2}}{\varpi_0^2} \frac{d(j\tau^{1/2})}{d\tau}.$$

Now, the $d(j\tau^{1/2})/d\tau$ term can be obtained in the same way as we calculated Eq. 4.21. We don't know how much $d(j\tau^{1/2})/d\tau$ is, but we know how much $\tau dj/d\tau$ is, so we first expand the first derivative to see how we can relate it with the second:

$$\tau^{1/2} \frac{d}{d\tau} (j\tau^{1/2}) = \tau^{1/2} \left(\tau^{1/2} \frac{d}{d\tau} j + j \frac{\tau^{-1/2}}{2} \right) = \tau \frac{d}{d\tau} j + \frac{j}{2}.$$

This last relation is identical, up to a factor of $1/2$, to Eq. 4.20.

So we just write the same relations except for a factor of $1/2$ for the j term that comes out from integrating Eq. 4.17. We get

$$\begin{aligned} \frac{d\theta}{d\tau} &= -\frac{2\tau^{1/2}}{\varpi_0^2} \frac{d(j\tau^{1/2})}{d\tau} = \frac{-2}{\varpi_0} \left(\tau \frac{d}{d\tau} j + \frac{j}{2} \right) = \\ &= \frac{-2}{\varpi_0} \left(\frac{VZ}{24} \kappa^2 \tau^2 (1 + 1/4) - \frac{V}{4} \left(Z + \frac{3\varpi_0}{16} \right) \left(\frac{\kappa^4 \tau^4}{5!} (1 + 1/8) - \frac{\kappa^6 \tau^6}{7!} (1 + 1/14) + \frac{\kappa^8 \tau^8}{9!} (1 + 1/16) \right) \right), \end{aligned}$$

which is reduced, after multiplying by $-2/\varpi_0^2$ and solving the ratio, to

$$\frac{d\theta}{d\tau} = -\frac{2\tau^{1/2}}{\varpi_0^2} \frac{d(j\tau^{1/2})}{d\tau} = \frac{-5VZ}{48\varpi_0^2} \kappa^2 \tau^2 + \frac{V}{4\varpi_0^2} \left(Z + \frac{3\varpi_0}{16} \right) \left(\frac{9}{20} \frac{\kappa^4 \tau^4}{4!} - \frac{13}{42} \frac{\kappa^6 \tau^6}{6!} + \frac{17}{72} \frac{\kappa^8 \tau^8}{8!} \right).$$

This last equation is in terms of τ . It has the big advantage that it gives us the position projected to the (θ) plane of the gas element by just integrating by τ , which gives us

$$\theta = -\frac{5VZ}{144\varpi_0^2 \kappa} \kappa^3 \tau^3 + \frac{V}{4\varpi_0^2 \kappa} \left(Z + \frac{3\varpi_0}{16} \right) \left(\frac{9}{100} \frac{(\kappa\tau)^5}{4!} - \frac{13}{294} \frac{(\kappa\tau)^7}{6!} + \frac{17}{648} \frac{(\kappa\tau)^9}{8!} + \dots \right). \quad (4.26)$$

If we want to make our equations adimensional, we can think that the first adimensional quantity could be one that relates quantities in the radial direction. We can then define $\lambda \equiv \Pi/\varpi_0$, and since our equations are written in terms of $\kappa\tau$, we can define the $s \equiv \kappa\tau$ variable which is also adimensional. If we use these definitions we can write Eq. 4.21 in terms of λ as

$$\lambda = \frac{\Pi}{\varpi_0} = \frac{s^2 Z}{16} - \frac{Z}{4\varpi_0} \left(1 + \frac{3\varpi_0}{16Z} \right) \left(\frac{s^4}{4 \times 4!} - \frac{s^6}{6 \times 6!} + \frac{s^8}{8 \times 8!} \right). \quad (4.27)$$

We can use the same proceeding for Eq. 4.26. In order to make the variable change in this equation, we need to first notice that there is a term $1/\kappa$ in both sides of the equation. In order to get rid of this term, we remember the definition of $\kappa = \sqrt{2V}/\varpi_0$ and substitute, resulting in

$$\theta = \frac{-5Zs^3}{144\sqrt{2}\varpi_0} + \frac{Z}{4\varpi_0\sqrt{2}} \left(1 + \frac{3\varpi_0}{16Z} \right) \left(\frac{9s^5}{100 \times 4!} - \frac{13s^7}{294 \times 6!} + \frac{17s^9}{648 \times 8!} \right),$$

or factorizing the term Z/ϖ_0 ,

$$\theta = -\frac{Z}{\varpi_0} \left(\frac{5\sqrt{2}s^3}{288} - \frac{\sqrt{2}}{8} \left(1 + \frac{3\varpi_0}{16Z} \right) \left(\frac{9s^5}{100 \times 4!} - \frac{13s^7}{294 \times 6!} + \frac{17s^9}{648 \times 8!} \right) \right). \quad (4.28)$$

This equation tells us how much the gas element that has been detached from the gas layer has moved in the azimuthal coordinate, projected on the plane. Together with Eq. 4.27, this allows us to calculate the trajectory of a gas element in radius and azimuth. These numbers depend basically on the radius, and on the altitude at which the gas elements, which were detached from the gas layer formed by the galactic fountain, originally are.

As an example, if $Z=3\text{kpc}$ and $\varpi_0 = 8.5\text{ kpc}$, then

$$\varpi_0/Z \approx 2.8$$

and

$$1 + 3\varpi_0/16Z \approx 1.5.$$

4.4 *Triggering of Cloud Collapse in a Galactic Disk by Infall of a High-Velocity Cloud* **67**

As mentioned at the beginning of this section, this trajectory can be used by any cloud falling into the disk, so if, for example, we have a cloud like Complex C, with a Galactic height of 10 kpc, we just change the value of Z to 10 and we would have

$$\varpi_0/Z \approx 0.85$$

and

$$1 + 3\varpi_0/16Z \approx 1.15.$$

As we said at the beginning of this section, this calculations apply to HVCs formed in the Galactic Fountain scenario as well as those of extragalactic origin. This simple analytic analysis can provide us with tools to calculate the path an infalling HVC would follow while interacting with a gaseous Galactic disk. Yet, the interaction process itself needs to be described from the point of view of the hydrodynamical equations and this is the topic of the next sections.

4.4 **Triggering of Cloud Collapse in a Galactic Disk by Infall of a High-Velocity Cloud**

In this section, we aim to make sufficient simplifications of the five classical coupled equations representing the rotating gas disk of a standard disk galaxy describing the interaction of a HVC with a quiescent gas disk in rotation to allow us to obtain an analytical solution. We then use this to explore how the impact of a HVC on a disk affects the underlying gravitation equilibrium of the clouds and thereby triggers their collapse prior to the star-forming process. Our model includes a giant HVC colliding at velocities in excess of 100 km s^{-1} with a galactic disk with (1) finite thickness and uniform rotation, (2) infinite thickness and a shearing box approximating differential rotation, and (3) infinite thickness and a shearing box with magnetic field.

4.4.1 **Infinite thickness and uniform rotation**

We first study the ideal magnetohydrodynamic equations with an infinite conductivity in a rotating reference frame at an angular velocity Ω , for a homogeneous disk with infinite thickness, following Chandrasekhar (1954) in order to obtain the modified Jeans condition for this case.

The equations that describe the behaviour of this system are the equation of continuity, the motion equation and the Poisson equation:

$$\frac{\partial \rho}{\partial t} + \nabla \cdot (\rho v) = 0$$

$$\frac{\rho \partial v}{\partial t} + \rho(v \cdot \nabla)v = -\nabla P - \rho \nabla \psi + 2\rho(v \times \Omega) \pm (0, 0, \frac{\rho V_{\text{HVC}}^2 10^{-4}}{3d})$$

$$\nabla^2 \psi = -4\pi G\rho,$$

where v is the velocity of the fluid with respect to the rotating axes, ρ and P are the density and pressure respectively, and ψ is the gravitational potential. The last term in the motion equation is the force supplied by the shock front produced when the HVC impinges on the ISM of the galactic disk (on a vertical direction, thus only taking into account the z axis) with a typical HVC density of $\rho \sim 10^{-4} \rho_{\text{ISM}}$. This term was first calculated in Casuso et al. (2006), and was taken from Huang & Weigert (1982) who used the expression $\rho v^2/d$ as a momentum flux in a shock front. A positive value of this term means that during the interaction of the HVC with the disk, the shock front destabilizes some fraction of the gas favoring gravitational collapse, while a negative value implies that after a relaxation time, the clouds that have not yet collapsed to form stars will incorporate the shock energy as internal turbulent energy increasing the stability of the clouds until the energy is dissipated and the equilibrium is reestablished.

If we consider that the pressure changes are adiabatic, $\delta P = c^2 \delta \rho$, and suppose that the medium is homogeneous and static, we can then introduce infinitesimal perturbations in the system in order to find out its behaviour to first order. In doing so we can obtain a dispersion equation that tell us when we can have instability in the system. The small perturbations analysis is deferred to Appendix D.

Now, the dispersion equation of the system is

$$|A| = 0 \longrightarrow (-w^2 + 4\Omega^2)(-w^2 + k^2 c^2 - 4\pi G) i k^2 = 0 \quad (4.29)$$

the solution of which gives us the wave propagation modes

$$w_1 = \pm 2\Omega, \text{ and}$$

$$w_2 = \pm \left(k^2 c^2 - 4\pi G \mp \frac{V_{\text{HVC}}^2 10^{-4} k}{3d} \right)^{1/2} = 0$$

If we take $\Omega_3^2 = c^2 k^2 - 4\pi G \rho \mp \frac{10^{-4} V_{\text{HVC}}^2 k}{3d}$, we can infer that the two modes in which the waves can be propagated through the medium are related by $w_1 w_2 = 2\Omega_3 \Omega$. For this case we can observe that the instability is introduced on the medium through the classic Jean's term modified only by the momentum flux from the HVC, as given by Casuso et al (2006).

4.4.2 Shearing Box and Infinite Thickness

On this section we will add an important piece of physics to the problem under consideration: shear. The cloud is subjected to shear as it falls into the disk and on this section we will study the complexities brought upon our problem due to its inclusion. We follow the work of Goldreich & Lynden-Bell (1956b) in considering a medium which is uniformly sheared in the rotating axes. If we adopt a frame of reference on the rotating axes we have

$$\frac{\partial v}{\partial t} + (v \cdot \nabla)v + 2(\Omega \times v) - \Omega^2 R = \nabla \psi - \frac{1}{\rho} \nabla P$$

where v is the velocity of the fluid with respect to the rotating axes, Ω is the angular velocity around the z axis $(0, 0, \Omega)$, $R = (x, y, 0)$, and ψ the gravitational potential.

Assuming a polytropic fluid, the equation of state is $P = \kappa \rho^\gamma$, and we can write:

4.4 Triggering of Cloud Collapse in a Galactic Disk by Infall of a High-Velocity Cloud **69**

$$\frac{1}{\rho} \nabla P = \frac{1}{\rho} \kappa \rho^{\gamma-1} \gamma = \gamma \kappa \rho^{\gamma-2} = \nabla \left(\frac{\gamma \kappa}{\gamma-1} \rho^{\gamma-1} \right) \quad (4.30)$$

so that our effective potential can be written as:

$$\bar{\chi} \equiv \psi - \frac{\gamma \kappa \rho^{\gamma-1}}{\gamma-1}. \quad (4.31)$$

If $v = u_0 + u$, with $u_0 = u_0(R) \hat{\phi}$ as the equilibrium state velocity and u as the perturbation, and using the fact that $R = -\hat{z} \times \hat{\phi}$ for the term $2(\Omega \times u)$, then the perturbed motion equation is:

$$\frac{\partial u_0}{\partial t} + \frac{\partial u}{\partial t} + (u_0 \cdot \nabla) u_0 + (u_0 \cdot \nabla) u + (u \cdot \nabla) u_0 + (u \cdot \nabla) u + 2(\Omega \times u) + 2(\Omega \times u_0) - \Omega^2 R = \nabla \chi_0 + \nabla \chi_1.$$

Subtracting the part that is in equilibrium we get:

$$\frac{\partial u}{\partial t} + (u_0 \cdot \nabla) u + (u \cdot \nabla) u_0 + (u \cdot \nabla) u + 2(\Omega \times u) = \nabla \chi_1. \quad (4.32)$$

Now we concentrate on the stability of a small fraction of the Galaxy, around a point (R_0, ϕ_0, z) . We choose the axes velocities such that $u_0(R_0 = 0)$ and we place the axes (x, y, z) with the origin in (R_0, ϕ_0) in such a way that the x axis points in the opposite direction of the Galactic Center. If we expand the components of u_0 in the Taylor series around (R_0, ϕ_0) , remembering that $u = [0, u(R), 0]$, we obtain:

$$u(R_0, \phi_0, z) = R \frac{\partial u}{\partial R}(R) \hat{R} + \phi \frac{\partial u}{\partial \phi}(R) \hat{\phi} \Big|_{(R_0, \phi_0)}$$

so that

$$u_0(R_0, \phi_0) = \phi_0 \frac{\partial u(R)}{\partial \phi} \Big|_{(R_0, \phi_0)} = \phi_0 \frac{\partial u(R)}{\partial R} \frac{\partial R}{\partial \phi} = \phi_0 \frac{R_0}{\phi_0} \frac{\partial u(R)}{\partial R} \frac{\partial \hat{R}}{\partial \hat{\phi}},$$

and in polar coordinates

$$\frac{\delta \hat{e}_R}{\delta \hat{e}_\phi} = \hat{e}_\phi \quad \Rightarrow \quad u_0(R_0, \phi_0) = R_0 \frac{\partial u(R)}{\partial R} \hat{e}_\phi,$$

or in the new coordinates:

$$u_0(x, y, z) = (u_{0x}, u_{0y}, u_{0z}) = \left[\left(0, \frac{x}{R_0}, 0 \right) + 0 \left(\frac{x^2 + y^2}{R_0^0} \right) \right] R_0 u'_0$$

with $u'_0 = \frac{du_0}{dR} \Big|_{R=R_0}$.

Now, the Oort constant A can be evaluated in $R = R_0$ if we recall that the circular velocity is $-(u_0 + \Omega R)$ and that $u_0(R_0) = 0$:

$$A = \frac{1}{2} \frac{du_0}{dR} = \frac{1}{2} u'_0.$$

Substituting these equations in Eq. 4.32 we get

$$\begin{aligned} \frac{\partial u}{\partial t} + [u_{0x} \cdot \frac{\partial u}{\partial x}] + [u_{0y} \cdot \frac{\partial u}{\partial y}] + (u_{0z} \frac{\partial u}{\partial z}) + (u \cdot \nabla)(u_0) + 2\Omega \times u + (u \cdot \nabla)u = \nabla \chi_1 \\ \frac{\partial u}{\partial t} + [2A \times \frac{\partial u}{\partial y}] + 2A u_x \hat{y} + 2(\Omega \times u) + (u \cdot \nabla)u = \nabla \chi_1. \end{aligned} \quad (4.33)$$

In the same way, the equilibrium condition $\frac{\partial \rho}{\partial t} + \nabla \cdot (\rho u) = 0$ would be:

$$\frac{\partial(\rho + \delta\rho)}{\partial t} + \nabla \cdot (\rho + \delta\rho)(u_0 + u) = 0.$$

Subtracting the equilibrium state:

$$\begin{aligned} \frac{\partial \delta\rho}{\partial t} + \nabla \cdot [\rho(u_0 + u) + \delta\rho(u_0 + u)] = 0 \\ \Rightarrow \frac{\partial \delta\rho}{\partial t} + \nabla \cdot [(\rho u) + \delta\rho u_0] = 0 \\ \Rightarrow \frac{\partial \delta\rho}{\partial t} + \nabla \cdot (\rho u) + \nabla \cdot (\delta\rho u_0) = 0 \Rightarrow \frac{\partial \delta\rho}{\partial t} + \nabla \cdot (\rho u) + 2A_x \frac{\partial \delta\rho}{\partial y} = 0. \end{aligned} \quad (4.34)$$

We are now interested in changing to shearing axes, which move with the non-perturbed flux. So we use the following conversion:

$$\begin{aligned} x' &= x \\ y' &= y - 2A_x t \\ z' &= z \\ t' &= t \end{aligned}$$

and the transformation equations are then:

$$\begin{aligned} \frac{\partial}{\partial x} &= \frac{\partial}{\partial x'} - 2A_{x'} \frac{\partial}{\partial y'} \\ \frac{\partial}{\partial y} &= \frac{\partial}{\partial y'} \\ \frac{\partial}{\partial z} &= \frac{\partial}{\partial z'} \\ \frac{\partial}{\partial t} &= \frac{\partial}{\partial t'} - 2A_{x'} \frac{\partial}{\partial y'} \text{ and } \frac{\partial}{\partial t'} = \frac{\partial}{\partial t} + 2A_x \frac{\partial}{\partial y} \end{aligned}$$

Applying these transformations to the movement equation 4.33 we get, for the component in x :

$$\frac{\partial u_x}{\partial t'} + 2A_x \frac{\partial u_x}{\partial y'} + 2(\Omega \times u) + (u \cdot \nabla)u_x = \left(\frac{\partial}{\partial x'} - A t' \frac{\partial}{\partial y'} \right) \chi_1,$$

where $\Omega \times u = \hat{i}(-\Omega u_y) - \hat{j}(-\Omega u_x)$.

So we get:

$$\frac{\partial u_x}{\partial t'} - 2\Omega u_y + (u \cdot \nabla)u_x = \left(\frac{\partial}{\partial x'} - A't' \frac{\partial}{\partial y'} \right) \chi_1. \quad (4.35)$$

For the component in y :

$$\frac{\partial u_y}{\partial t'} + 4A_x \frac{\partial u_y}{\partial y} + 2A u_x \hat{y} + 2\Omega u_x + (u \cdot \nabla)u_y = \left(\frac{\partial}{\partial y'} \right) \chi_1$$

and with $B \equiv \frac{1}{2} \left(\frac{u}{R} + \frac{\partial u}{\partial R} \right) = \Omega + A$

$$\frac{\partial u_y}{\partial t'} + 2B u_x + (u \cdot \nabla)u_y = \left(\frac{\partial}{\partial y'} \right) \chi_1, \quad (4.36)$$

and for the component in z :

$$\frac{\partial u_z}{\partial t'} + (u \cdot \nabla)u_z = \left(\frac{\partial}{\partial z'} \right) \chi_1. \quad (4.37)$$

In the same way, the transformed continuity equation 4.34 becomes:

$$\begin{aligned} \frac{\partial \delta \rho}{\partial t'} + 2A_x \frac{\partial \delta \rho}{\partial y} + \left(\frac{\partial}{\partial x'} - A't' \frac{\partial}{\partial y'} \right) (\rho u_x) + \frac{\partial}{\partial y'} (\rho u_z) + 2A_x \frac{\partial \delta \rho}{\partial y} &= 0 \\ \frac{\partial \delta \rho}{\partial t'} + \left(\frac{\partial}{\partial x'} - A't' \frac{\partial}{\partial y'} \right) (\rho u_x) + \frac{\partial}{\partial y'} (\rho u_z) &= 0, \end{aligned} \quad (4.38)$$

and the perturbed Poisson equation would be:

$$\left[\left(\frac{\partial}{\partial x'} - A't' \frac{\partial}{\partial y'} \right)^2 + \frac{\partial^2}{\partial y'^2} + \frac{\partial^2}{\partial z'^2} \right] \delta \Psi = -4\pi G \delta \rho. \quad (4.39)$$

In order to linearize the equations 4.35, 4.36, and 4.37, we have to eliminate the term $(u \cdot \nabla)u$ and replace ρ for ρ_0 , for the other terms are quadratic. The equation 4.30 is linearized as:

$$\delta \chi = \delta \psi - c^2 \frac{\delta \rho}{\rho_0}, \quad (4.40)$$

where $c^2 = k\gamma\rho_0^{\gamma-1}$.

If we do a Fourier analysis in x' and y' , and assuming that the perturbed quantities are of the form $e^{i(K_x x' + k_y y')}$, the linearized equations 4.35, 4.36, and 4.37 become:

$$\frac{\partial u_x}{\partial t'} - 2\Omega u_y = i(k_x - 2A't'k_y)\chi_1 \quad (4.41)$$

$$\frac{\partial u_y}{\partial t'} + 2B u_x = i k_y \chi_1 \quad (4.42)$$

$$\frac{\partial u_z}{\partial t'} = \frac{\partial \chi_1}{\partial z'}. \quad (4.43)$$

Equation 4.38 tells us that:

$$\frac{\partial \delta \rho}{\partial t'} + i(k_x - 2At'k_y)\rho_0 u_x + ik_y \rho_0 u_y + \frac{\partial}{\partial z'}(\rho_0 u_z) = 0, \quad (4.44)$$

and equation 4.39:

$$\left[(k_x - 2At'k_y)^2 + k_y^2 - \frac{\partial^2}{\partial z'^2} \right] \psi_1 = 4\pi G \delta \rho. \quad (4.45)$$

We introduce now a new “temporal” variable τ , defined as:

$$\tau = 2At' - \frac{k_y}{2A}.$$

Equations 4.41, 4.42, and 4.43 can be written in terms of this new variable. First we divide by $2A$, we define the variable $K \equiv \frac{k_y}{2A}$, and we obtain:

$$\begin{aligned} \frac{\partial u_x}{2A \partial t'} - \frac{2\Omega u_y}{2A} &= \frac{i}{2A} (k_x - 2At'k_y) \chi_1 = \\ &= \frac{-i}{2A} (2At'k_y - k_x) \chi_1 = \\ &= -ik_y \left(t' - \frac{k_x}{2Ak_y} \right) \chi_1 = \\ &= \frac{ik_y}{2A} \left(2At'k_y - \frac{k_x}{k_y} \right) \chi_1 \end{aligned}$$

which turns out to be:

$$i_x - \frac{\Omega}{A} u_y = -iK \tau \chi_1. \quad (4.46)$$

From Eq. 4.42 we obtain:

$$\frac{\partial u_y}{2A \partial t'} + \frac{2Bu_x}{2A} = -\frac{ik_y}{2A} \chi_1 = iK \chi_1$$

which gives us:

$$i_y + \frac{Bu_x}{A} = -iK \chi_1. \quad (4.47)$$

And from Eq. 4.43 we get:

$$\frac{\partial u_z}{2A \partial t'} = \frac{1}{2A} \frac{\partial}{\partial t'} \chi_1$$

which gives us:

$$i_z = \frac{1}{2A} \frac{\partial}{\partial z'} \chi_1. \quad (4.48)$$

In a similar way, if we divide Eq. 4.44 by $2A$ we obtain:

$$\begin{aligned}
 \frac{\partial \delta \rho}{2A \partial t'} + \frac{i}{2A} (k_x - 2At'k_y) \rho_0 u_x + \frac{ik_y}{2A} \rho_0 u_y + \frac{\partial(\rho_0 u_z)}{2A \partial z'} &= 0 \\
 \delta \dot{\rho} - \frac{ik_y}{2A} (2At' - \frac{k_x}{k_y}) \rho_0 u_x + iK \rho_0 u_y + \frac{\partial}{2A \partial z'} (\rho_0 u_z) &= 0 \\
 \delta \dot{\rho} - iK \tau \rho_0 u_x + iK \rho_0 u_y + \frac{\partial}{2A \partial z'} (\rho_0 u_z) &= 0.
 \end{aligned} \tag{4.49}$$

Multiplying Eq. 4.45 with Eq. 4.30 we obtain:

$$\begin{aligned}
 \left(-k_y^2 \left(2At' - \frac{k_x}{k_y} \right)^2 + k_y^2 + \frac{\partial^2}{\partial z'^2} \right) \psi_1 &= 4\pi G \delta \rho \\
 \left[-k_y^2 (1 + \tau^2)^2 + \frac{\partial^2}{\partial z'^2} \right] \psi_1 &= 4\pi G \delta \rho.
 \end{aligned} \tag{4.50}$$

In order to derive the second component of the vorticity equation, we multiply Eq. 4.47 by $-iK\tau$ and Eq. 4.46 by $-iK$

$$-iK\tau u_y - iK\tau \frac{B}{A} u_x = K^2 \tau \chi_1$$

and

$$-iK u_y + iK \frac{\Omega}{A} u_y = -K^2 \tau \chi_1,$$

and then we add them, to obtain:

$$-iK \frac{\partial}{\partial \tau} (u_x + \tau u_y) + iK \left(-\frac{\tau B}{A} u_x + \frac{\Omega}{A} u_y \right) = 0.$$

And if $\Omega_0 = B - A$ when $\frac{\Omega}{A} = \frac{B-A}{A}$, then:

$$-iK \frac{\partial}{\partial \tau} (u_x + \tau u_y) + iK \frac{B}{A} (-\tau u_x + u_y - 1) = 0. \tag{4.51}$$

In a similar way, if we multiply Eq. 4.46 by $-iK\tau$ and Eq. 4.47 by iK , we obtain:

$$-iK\tau u_x + iK \frac{\Omega}{A} u_x = -K^2 \tau^2 \chi_1$$

and

$$-iK u_y + iK \frac{B}{A} u_x = -K^2 \chi_1,$$

and then we add them, to obtain:

$$\begin{aligned}
 -iK \frac{\partial}{\partial \tau} (u_y - \tau u_x) + iK \left(\frac{\tau \Omega}{A} u_y + \frac{B}{A} u_x \right) &= -K^2 (1 + \tau^2) \chi_1 \\
 -iK \frac{\partial}{\partial \tau} (u_y - \tau u_x) + iK \frac{\Omega}{A} (\tau u_y + u_x) + 2iK u_x &= -K^2 (1 + \tau^2) \chi_1.
 \end{aligned} \tag{4.52}$$

If we focus on not having any variations in z , that is, $\frac{\partial}{\partial z} = 0$ and $u_z = 0$, the equation of continuity (Eq. 4.49) becomes:

$$\begin{aligned} \delta\dot{\rho} - iK\tau\rho_0u_x + iK\rho_0u_y &= 0 \\ iK(-\tau u_x + u_y) &= -\frac{\delta\dot{\rho}}{\rho_0}. \end{aligned} \quad (4.53)$$

If we substitute the value of Eq. 4.53 in the vorticity equation, 4.51, we obtain:

$$\begin{aligned} -iK\frac{\partial}{\partial\tau}(u_x + \tau u_y) + iK\frac{B}{A}\left(\frac{\delta\dot{\rho}}{\rho_0 iK}\right) &= 0 \\ \frac{\partial}{\partial\tau}\left[iK(u_x + \tau u_y) - \frac{B}{A}\frac{\delta\dot{\rho}}{\rho_0}\right] &= 0 \\ iK(u_x + \tau u_y) - \frac{B}{A}\frac{\delta\dot{\rho}}{\rho_0} &= C_1. \end{aligned} \quad (4.54)$$

where C_1 is a constant. If we now multiply Eq. 4.53 by $-\tau$, add it to Eq. 4.54 multiplied by -1 , and define $\frac{\delta\dot{\rho}}{\rho_0} \equiv \dot{\Theta}_1$, we get:

$$\begin{aligned} iK(\tau^2 u_x - \tau u_y) &= \left(\tau\dot{\Theta}_1 + \frac{B}{A}\dot{\Theta}_1 + C_1\right)(-1) \\ iK(u_x(1 + \tau^2)) &= -\tau\dot{\Theta}_1 - \frac{B}{A}\dot{\Theta}_1 - C_1. \end{aligned} \quad (4.55)$$

Equations 4.53, 4.54, and 4.55 can be used as follows to eliminate the velocity in Eq. 4.52:

$$\begin{aligned} iK\frac{\partial}{\partial\tau}\left(-\frac{\dot{\Theta}_1}{iK}\right) + iK\frac{\Omega}{A}\left(\frac{-C_1 - \frac{B\Theta_1}{A}}{iK}\right) + 2iK\left(\frac{-C_1 - \frac{B\Theta_1}{A} - \tau\dot{\Theta}_1}{iK(1 + \tau^2)}\right) &= -K^2(1 + \tau^2)\chi_1 \\ -\ddot{\Theta}_1 + \frac{\Omega}{A}\left(-C_1 - \frac{B\Theta_1}{A}\right) + \frac{2}{(1 + \tau^2)}\left(-\tau\dot{\Theta}_1 - C_1 - \frac{B\Theta_1}{A}\right) &= -K^2(1 + \tau^2)\chi_1 \end{aligned} \quad (4.56)$$

$$\begin{aligned} \frac{\ddot{\Theta}_1}{(1 + \tau^2)} + \frac{2\tau\dot{\Theta}_1}{(1 + \tau^2)} + \frac{\Omega}{A(1 + \tau^2)}\left(C_1 + \frac{B\Theta_1}{A}\right) + \frac{2}{(1 + \tau^2)^2}\left(C_1 + \frac{B\Theta_1}{A}\right) &= K^2\chi_1 \\ \frac{\partial}{\partial\tau}\left(\frac{\dot{\Theta}_1}{(1 + \tau^2)}\right) + \left(\frac{\frac{2B}{A}}{(1 + \tau^2)^2} + \frac{\frac{B\Omega}{A^2}}{(1 + \tau^2)}\right)\left(\Theta_1 + \frac{AC_1}{B}\right) &= K^2\chi_1. \end{aligned} \quad (4.57)$$

And now, from Eqs. 4.40 and 4.50, we get:

$$\left[-k_y^2(1 + \tau^2) + \frac{\partial^2}{\partial z'^2}\right]\left(\chi_1 + \frac{c^2\delta\rho}{\rho_0}\right) = -4\pi G\delta\rho$$

$$\begin{aligned}
 -k_y^2 (1 + \tau^2) \left(\chi_1 + \frac{c^2 \delta \rho}{\rho_0} \right) &= -4\pi G \delta \rho \\
 \chi_1 &= \frac{-4\pi G \delta \rho - c^2 \delta \rho k_y^2 (1 + \tau^2)}{-k_y^2 (1 + \tau^2)} \\
 \chi_1 &= \left(\frac{4\pi G \delta \rho}{k_y^2 (1 + \tau^2)} - c^2 \right) \Theta_1.
 \end{aligned} \tag{4.58}$$

If we add the HVC term, Eq. 4.40 becomes:

$$\chi_1 = \psi - \frac{c^2 \delta \rho}{\rho_0} \pm \frac{\alpha V_{\text{HVC}}^2}{3dK} \frac{\delta \rho}{\rho}$$

and we can write:

$$-4\pi G \delta \rho = \left[-k_y^2 (1 + \tau^2) + \frac{\partial^2}{\partial z'^2} \right] \left(\chi_1 + \frac{c^2 \delta \rho}{\rho_0} \pm \frac{\alpha V_{\text{HVC}}^2 \delta \rho}{3dK \rho} \right) \tag{4.59}$$

$$\chi_1 = \left[\frac{4\pi G \rho_0}{k_y^2 (1 + \tau^2)} - c^2 \pm \frac{\alpha V_{\text{HVC}}^2}{3dK} \right] \Theta_1. \tag{4.60}$$

Remembering that $K = \frac{k_y}{2A}$, we multiply Eq. 4.58 by K^2 , and for simplicity we submit for now our HVC term:

$$K^2 \chi_1 = \frac{K_y^2}{4A^2} \left(\frac{4\pi G \rho_0}{k_y^2 (1 + \tau^2)} - c^2 \right) \Theta_1.$$

If, for simplicity, we consider $C_1 = 0$, then we have:

$$\begin{aligned}
 \frac{\partial}{\partial \tau} \left(\frac{\dot{\Theta}_1}{(1 + \tau^2)} \right) + \left(\frac{\frac{2B}{A}}{(1 + \tau^2)^2} + \frac{\frac{B\Omega}{A^2}}{(1 + \tau^2)} \right) \Theta_1 &= \frac{K_y^2}{4A^2} \left(\frac{4\pi G \rho_0}{k_y^2 (1 + \tau^2)} - c^2 \right) \Theta_1 \\
 \frac{\partial}{\partial \tau} \left(\frac{\dot{\Theta}_1}{(1 + \tau^2)} \right) + \left(\frac{2B}{A(1 + \tau^2)^2} + \frac{\frac{B\Omega}{A^2} - \frac{\pi G \rho_0}{A^2}}{(1 + \tau^2)} + \frac{k_y^2 c^2}{4A^2} \right) \Theta_1 &= 0.
 \end{aligned} \tag{4.61}$$

We can obtain the equation for asymmetric “ring” models by having $k_y = 0$ and applying the limit process $\tau \rightarrow 0$ as follows:

$$\frac{\partial}{\partial \tau} \left(\dot{\Theta}_1 \right) + \left(\frac{B\Omega}{A^2} - \frac{\pi G \rho_0}{A^2} + \frac{k_x^2 c^2}{4A^2} \right) \Theta_1 = 0. \tag{4.62}$$

We now look into the equations with the HVC term.

$$\frac{\partial^2 \Theta_1}{\partial \tau^2} + \left[\frac{B\Omega}{A^2} - \frac{\pi G \rho_0}{A^2} + \frac{K^2 (c^2 \mp \alpha V_{\text{HVC}}^2 / 3dK)}{4A^2} \right] \Theta_1 = 0.$$

This is the equation of a simple harmonic oscillator and it tells us that the “ring” waves are stable or unstable if:

$$\frac{B\Omega}{A^2} - \frac{\pi G\rho_0}{A^2} + \frac{K^2 \left(c^2 \pm \frac{\alpha V_{\text{HVC}}^2 \delta}{3dK} \right)}{4A^2} > 0 \text{ stable}$$

$$\frac{B\Omega}{A^2} - \frac{\pi G\rho_0}{A^2} + \frac{K^2 \left(c^2 \pm \frac{\alpha V_{\text{HVC}}^2 \delta}{3dK} \right)}{4A^2} < 0 \text{ unstable.}$$

The motion equation that includes the HVC term is:

$$\frac{\partial u}{\partial t} + (u \cdot \nabla)u + 2\Omega \times u - \Omega^2 r = \nabla\psi - \frac{\nabla P}{\rho} \pm \frac{\rho_{\text{HVC}} V_{\text{HVC}}^2 \hat{e}}{3d\rho}$$

with \hat{e} pointing towards the z direction. So now we can define an effective potential as done before in Eq 4.30, with $P = \kappa\rho^\gamma$:

$$\frac{\nabla P}{\rho} = \frac{1}{\rho} \kappa \rho^{\gamma-1} \gamma = \gamma \kappa \rho^{\gamma-2} = \nabla \left(\frac{\gamma \kappa \rho^{\gamma-1}}{\gamma-1} \right)$$

And since $\nabla\chi = \nabla\psi - \frac{\nabla P}{\rho} + \frac{\rho_{\text{HVC}} V_{\text{HVC}}^2}{3d\rho}$, we get:

$$\chi = \psi - \frac{\gamma \kappa \rho^{\gamma-1}}{\gamma-1} \pm \frac{\rho_{\text{HVC}} V_{\text{HVC}}^2}{3d} \log \rho.$$

We linearize this term for Eq. 4.32:

$$\delta\chi + \chi = \psi + \delta\psi + \frac{P + \delta P}{\rho} \pm \frac{\rho_{\text{HVC}} V_{\text{HVC}}^2}{3d} \log(\rho + \delta\rho), \quad (4.63)$$

where

$$\begin{aligned} \frac{P + \delta P}{\rho} &= \frac{\kappa}{\rho} (\rho + \delta\rho)^\gamma = \\ &= \frac{1}{\rho} \left(\kappa \rho^\gamma \left(1 + \frac{\delta\rho}{\rho} \right)^\gamma \right) = \\ &= \frac{1}{\rho} \left(\kappa \rho^\gamma \left(1 + \frac{\delta\rho}{\rho} + \dots \right) \right) = \\ &= \frac{\kappa \rho^2}{\rho} + \gamma \kappa \rho^{\gamma-1} \delta\rho = \\ &= \frac{P + c^2 \delta\rho}{\rho} = \frac{P}{\rho} + \frac{c^2 \delta\rho}{\rho} \end{aligned}$$

and expanding in Taylor series for the HVC term as well:

$$\frac{\rho_{\text{HVC}} V_{\text{HVC}}^2}{3d} \log(\rho + \delta\rho) = \frac{\rho_{\text{HVC}} V_{\text{HVC}}^2}{3d} \left[\log \rho + \frac{\delta\rho}{\rho} + \dots \right]$$

so that Eq. 4.63 becomes:

$$\delta\chi + \chi = \psi + \delta\psi + \frac{P}{\rho} - \frac{c^2\delta\rho}{\rho} \pm \frac{\rho_{\text{HVC}}V_{\text{HVC}}^2}{3d} \left[\log \rho + \frac{\delta\rho}{\rho} \right],$$

and, eliminating the non-perturbed terms:

$$\delta\chi = \chi_1 = \psi_1 - \frac{c^2\delta\rho}{\rho} \pm \frac{\rho_{\text{HVC}}V_{\text{HVC}}^2}{3d} \frac{\delta\rho}{\rho}. \quad (4.64)$$

Which is our new linearized form. Now, starting from Eq. 4.57, we can calculate the new χ_1 as follows. Recalling Eq. 4.59:

$$-4\pi G\delta\rho = \left[-k_y^2(1 + \tau^2) + \frac{\partial^2}{\partial z'^2} \right] \left(\chi_1 + \frac{c^2\delta\rho}{\rho_0} \pm \frac{\rho_{\text{HVC}}V_{\text{HVC}}^2\delta\rho}{3d\rho} \right)$$

and solving for χ_1

$$\chi_1 = \frac{-4\pi G\delta\rho - \frac{c^2\delta\rho}{\rho_0}k_y^2(1 + \tau^2) \pm \frac{\rho_{\text{HVC}}V_{\text{HVC}}^2\delta\rho}{3d\rho}k_y^2(1 + \tau^2)}{k_y(1 + \tau^2)}$$

$$\chi_1 = \left[\frac{4\pi G\rho_0}{k_y^2(1 + \tau^2)} - c^2 \pm \frac{\rho_{\text{HVC}}V_{\text{HVC}}^2}{3d} \right] \frac{\delta\rho}{\rho}.$$

If we suppose a mean value of $\rho \sim 1$ and that $\rho \sim 10^{-4}\rho_{\text{HVC}} = \alpha\rho_{\text{HVC}}$, and since we are investigating a box with a length scale of K , we could substitute ρ_{HVC} for $\frac{\alpha}{K}$, and we get:

$$\chi_1 = \left[\frac{4\pi G\rho_0}{k_y^2(1 + \tau^2)} - c^2 \pm \frac{\alpha V_{\text{HVC}}^2}{3dK} \right] \Theta_1,$$

where $\Theta_1 = \frac{\delta\rho}{\rho}$. Again, we use this equation in order to obtain the equation of the simple harmonic oscillator, which becomes:

$$\frac{\partial^2\Theta_1}{\partial\tau^2} + \left[\frac{B\Omega}{A^2} - \frac{\pi G\rho_0}{A^2} + \frac{K^2 \left(c^2 \pm \frac{\alpha V_{\text{HVC}}^2\delta}{3dK} \right)}{4A^2} \right] \Theta_1 = 0, \quad (4.65)$$

where the second term indicates us if the system is stable (where > 0) or unstable (where < 0). Once again we have the classic Jean's criterion $k^2c^2 - \pi G\rho_0$ modified, this time, by the shear, reflected in the use of the Oort constants A and B, and the term for the cloud impact taken from Casuso et al. (2006). This leads us to conclude that the shear does not prevent the system from achieving the conditions for gravitational instability and provides us with a mathematical modification for it when shear is present.

4.4.3 Infinite thickness and a shearing box with magnetic field

The next physical property to be considered in our stability study is the inclusion of magnetic fields. So now we turn to study the infall of the HVC on a disk with infinite thickness in a shearing box, where a magnetic field is included in the disk. For this, we include a magnetic term into our equations (following Chandrasekhar 1954). The movement equations with the magnetic field terms are:

$$\frac{\partial \rho}{\partial t} + \nabla \cdot (\rho u) = 0 \quad (4.66)$$

$$\rho \left(\frac{\partial u}{\partial t} + (u \cdot \nabla) u \right) = -\nabla P + \rho \nabla \Phi + 2\rho(u \times \Omega) \pm \rho \left(0, 0, \frac{\rho V_{\text{HVC}}^2 10^4}{3d} \right) + \frac{1}{4\pi} (B \cdot \nabla) B - \frac{1}{8\pi} \nabla B^2 \quad (4.67)$$

$$\frac{\partial B}{\partial t} = \nabla \times (u \times B) \quad (4.68)$$

$$\nabla^2 \Phi = -4\pi G \rho. \quad (4.69)$$

We can see that we now have an additional equation, the magnetic induction equation, Eq. E.4 (see Appendix E). In order to linearize them we are going to follow the same procedure as always: we are going to perturb the equations with a small term, that is, a given quantity which is perturbed with an infinitesimal amplitude δq such that any term of the order $\delta q/q^2$ and higher will disappear. Since we have already linearized most of the terms in the previous section, we will now only linearize the magnetic terms of the movement and induction equations. Then, we will add these terms to our previously linearized equations in Section 4.4.2. Once we have all the linearized terms of the equations, we will be able to calculate the dispersion equation of the system. Let us remember that once we find an imaginary square root for the dispersion equation, then we know that for that frequency the system is unstable. In this case the instability is of the Jeans type, as we are including Poisson's equation, and it is for that wave longitude that we can say stars are being formed.

The process to linearize these equations, though laborious, is completely analogous to the previous ones, so we will refer the interested reader to Appendix E.

An important thing to note here is that the induction equation is telling us that there is no change over time in the variation of the magnetic field in the z direction. Besides the condition of $\nabla \cdot B = 0$, we can see that $\delta B_z = 0$ so there is no equation for δB_z . Then the set of linearized equations is:

$$\frac{\partial \delta B_x}{\partial t} - \frac{\partial u_x B_z}{\partial z} = 0 \quad (4.70)$$

$$\frac{\partial \delta B_y}{\partial t} - \frac{\partial (u_y B_z - u_z B_y)}{\partial z} = 0 \quad (4.71)$$

$$\frac{\partial u_x}{\partial t} - 2u_y \Omega - \frac{B_z}{4\pi\rho} \frac{\partial}{\partial z} \delta B_x = 0 \quad (4.72)$$

$$\frac{\partial u_y}{\partial t} + 2u_x \Omega - \frac{B_z}{4\pi\rho} \frac{\partial}{\partial z} \delta B_y = 0 \quad (4.73)$$

$$\frac{\partial u_z}{\partial t} + \frac{c^2}{\rho} \frac{\partial \delta \rho}{\partial z} \pm \frac{10^{-4} V_{\text{HVC}}^2 \delta \rho}{3d} - \frac{\partial \delta V}{\partial z} + \frac{B_y}{4\pi\rho} \frac{\partial}{\partial z} \delta B_y = 0 \quad (4.74)$$

$$\frac{\partial \delta \rho}{\partial t} + \rho \frac{\partial u_z}{\partial z} = 0 \quad (4.75)$$

$$\frac{\partial^2 \delta V}{\partial z^2} + 4\pi G \delta \rho = 0. \quad (4.76)$$

In order to analyze the stability of the disk when it is interacting with the HVC, we analyze solutions to these equations in the form of $q = \hat{q}e^{i(kz+\omega t)}$ where q is a generic coefficient that indicates the solutions to the variables δB_x , δB_y , u_x , etc. Under this supposition, the system of the coupled partial differential equations above is reduced to the following system of linear equations:

$$i\omega \delta B_x - ik u_x B_z = 0 \quad (4.77)$$

$$i\omega \delta B_y - ik(u_y B_z - u_z B_y) = 0 \quad (4.78)$$

$$i\omega u_x - 2u_y \Omega - \frac{ik B_z \delta B_x}{4\pi \rho} = 0 \quad (4.79)$$

$$i\omega u_y + 2u_x \Omega - \frac{ik B_z \delta B_y}{4\pi \rho} = 0 \quad (4.80)$$

$$i\omega u_z + \frac{ikc^2 \delta \rho}{\rho} \pm \frac{10^{-4} V_{\text{HVC}}^2 \delta \rho}{3d} - ik \delta V + \frac{ik B_y \delta B_y}{4\pi \rho} = 0 \quad (4.81)$$

$$i\omega \delta \rho + ik \rho u_z = 0 \quad (4.82)$$

$$-k^2 \delta V + 4\pi G \delta \rho = 0. \quad (4.83)$$

A non-trivial solution to this system of equations allows us to derive an equation for w in terms of k . This would be the dispersion equation, and since we supposed that all the quantities were in the form of $q = \hat{q}e^{i(kz+\omega t)}$, when ω becomes imaginary then our variables will be proportional to $q \propto \hat{q}e^{\pm \omega t}$, which means that the perturbations we introduce could disappear or increase exponentially in time. This means that when w becomes imaginary, we will need to carefully analyze the dispersion equation in order to decide if the system is stable or not, and for which values of ω the introduced perturbations to the system increase exponentially in time.

In order to obtain the dispersion equation of this system, we take the determinant of the matrix formed by the coefficients of the system of linearized equations previously described. Such a determinant is then set equal to zero and in this way we can obtain the dispersion equation of the system. To help us write the dispersion equation in a more comprehensible way, we use the definitions of $\Omega_A^2 \equiv k^2 B_z^2 / 4\pi \rho$, and $\Omega_B^2 \equiv k^2 B_y^2 / 4\pi \rho$. $V_A^2 \equiv B_z^2 / 4\pi \rho$ is basically the definition of the Alfvén velocity that is so characteristic in problems that involve magnetic fields. If we multiply this velocity by k^2 then we would be taking of the Alfvén “frequency” of the perturbations that propagate in this magnetized medium.

Another important definition, since our problem includes selfgravity, is the Jeans frequency (which corresponds to the Jeans longitude), such that $\Omega_J^2 \equiv c^2 k^2 - 4\pi G\rho$.

With these definitions, the dispersion equation of the system can be written as:

$$\begin{aligned} \omega^6 + \omega^4(\pm k\rho \frac{10^{-4}V_{\text{HVC}}^2}{3d} - \Omega_J^2 - 4\Omega^2 - 2\Omega_A^2 - \Omega_B^2) + \\ \omega^2[\Omega_A^4 + \Omega_A^2\Omega_B^2 + 4\Omega_B^2\Omega^2 + 4\Omega^2\Omega_J^2 \pm \frac{10^{-4}V_{\text{HVC}}^2 k\rho}{3d}(4\Omega^2 + \Omega_A^2) + \Omega_A^2\Omega_J^2] \\ \pm \frac{10^{-4}V_{\text{HVC}}^2\Omega_A^4 k\rho}{3d} - \Omega_A^4\Omega_J^2 = 0. \end{aligned}$$

From this equation it follows that there are three modes of wave propagation in this medium. If w_1 , w_2 and w_3 represent the frequencies of such modes then we have the following relations (Chandrasekhar 1953):

$$w_1^2 + w_2^2 + w_3^2 = 4\Omega^2 + 2\Omega_A^2 + \Omega_B^2 + \Omega_J^2 \mp k\rho \frac{10^{-4}V_{\text{HVC}}^2}{3d} \quad (4.84)$$

and

$$w_1 w_2 w_3 = \Omega_A^2 \Omega_J \pm \frac{10^{-4}V_{\text{HVC}}^2 k\rho}{3d} \Omega_A^2. \quad (4.85)$$

From this last equation we can observe that if Ω_J is imaginary then one of w_1, w_2 or w_3 must be imaginary. This fact assures that whenever Ω_J becomes imaginary there will be a wave mode propagating on the medium which will become unstable. Therefore we conclude that the condition for gravitational instability is modified according to eq. (4.85). We can deduce from this analysis that the inclusion of magnetic fields on our system can not stop regions on the edge of the Jeans instability to collapse. As we can see from equation (4.85) modifications to the classic Jeans criterion are related to the strength of the field via the Alfvén velocity and, of course, it is also related to the momentum carried by the HVC through the term for momentum exchange that appears in Casuso et al. (2006).

4.4.4 Conclusions

On this chapter we carried an analytical study of the HVC-disk interaction with the purpose of understanding the path it would take and how this interaction changes in response to different phenomena occurring in the ISM. Our first step was to follow a sheet of material ejected from the plane, in the Galactic fountain scenario, reaching the Galactic atmosphere, cooling and then raining down back onto the disk. The trajectory that such material follows on its way towards the disk can also be applied to a HVC of extragalactic origin, whose trajectory is sheared. Next, we devoted our calculations to analyze the stability of the gaseous disk when exposed to the perturbation provided by the exchange of momentum with a HVC. We performed several small perturbation analyses including different physical phenomena, in order to find out whether or not the interaction can lead pieces of the disk into the verge of gravitational instability.

We began by including rotation and then shear to our system of equations. Our perturbation analysis showed that there is always a wavelength that renders the system unstable

and that at the most, rotation and shear only modify the Jeans criterion. In this scenario for the interaction, molecular clouds already on the verge of gravitational instability are not sheared away or disrupted by the impact of the HVC and can be compressed further. Next we moved to tackle the problem including magnetic fields. As a result we found that magnetic fields could not prevent the HVC from compressing the medium to the verge of the gravitational instability.

In all the processes that were considered, there was always a wave propagation mode that lead the system to instability and that provided us with a modified version of the classical Jeans criterion. This interaction in turn can enable the star formation process due to the HVC-disk interaction and enhance the star formation rate on the disk. This leads us to think that HVCs may have wide implications on galactic evolution, as has already been discussed in Chapter 1.

In order to be able to follow in an appropriate way the complex interaction that we have described, we need an appropriate model of the Galactic disk that includes sources that provide the interstellar medium with energy, and which maintain it agitated. With the analytical model at hand, we can now use such a numerical model, like the one created by Avillez & Breitschwerdt (2004, 2005, 2007), a model developed through several years and which is appropriate for following the collision of HVCs with the Galactic disk. Hopefully this will allow us to obtain an appropriate view of the ISM and the galactic evolution in time.

Paper	Grid size	Cell size	HVC density	HVC velocity [kms ⁻¹]	HVC size	HVC initial disk height	Impact angle	Boundary conditions	Type of code	HVC mass [M_{\odot}]	HVC energy
Lepine+ (1994)	?	?	?	?	?	?	0	?	HD	?	?
Quilis+ (2001)	128×128×256	90 (DM) and 1.4 (HI) pc	10 ¹⁹ cm ⁻²	170-400	1 kpc	?	0 and 45	?	HD	?	?
Kudos+ (2004)	1400×2100 pc	1.4 pc	1 cm ⁻³	100 and 50	?	?	0	?	HD	?	?
Comeron+ (1992)	128×128	tens of pc	0.44 cm ⁻³	100	500 pc	?	0 and 45	?	MHD	?	?
Comeron+ (1994)	128×128	tens of pc	0.02 cm ⁻³	100 pc	1700 pc	?	45	?	MHD	3.3 · 10 ⁶	10 ⁵ Jy s km ⁻¹
Rand+ (1996)	64×128×128	?	0.95 cm ⁻³	200	500 pc	?	45	periodic	MHD	1.2×10 ⁷	?
Avillez (1999)	?	5 and 10 pc	?	90 to 139	from tenths to hundredths of pc	4 pc?	?	outflow and periodic	MHD	?	?
Santillan+ (1999)	200×200	15 pc	1 cm ⁻³	0-200	210×105 pc	350-4050 pc	0-60	cyclic and outflow	MHD	3 × 10 ⁵	3.5 × 10 ⁵²
Santillan+ (2001)	128×128×128	?	0.1 cm ⁻³	200	117×117×215 pc	4 pc	30	periodic and reflecting-outflow	MHD	10 ⁴	4 × 10 ⁵¹
Konz+ (2002)	103×153	?	10 ⁻³ cm ⁻³	0	100 pc	$y = 3$	0	?	MHD	?	?
Santillan+ (2004)	128×128×128	?	0.1 cm ⁻³	100	50 × 50 pc	2 kpc	0	periodic and outflow	MHD	4 × 10 ⁶	10 ⁵³
Santillan+ (2007)	$L \times L$ with 1024 ² zones	?	0.1 cm ⁻³	100	50 × 50 pc	2 kpc	0	?	MHD	?	10 ⁵⁰
Peek+ (2008)	–	–	?	?	?	?	0	?	TreeSPH	?	?

Table 4.1: Mass estimates for the HVC candidates, their projected distances with respect to their parent galaxies, and the velocity offset from systemic velocity of their parent galaxies.

5

Summary and Conclusions

On the following pages we will summarize the main results obtained in this work.

–There are several dynamical processes that can be explained with gas accretion in galactic disks, such as the chemical evolution of the Galaxy and galaxies in general, warps, bars and spiral structure, as well as star formation rates. In this work we focus on the in-fall of high velocity clouds (HVCs) on galactic disks, and their subsequent star formation, which would change and explain the chemical evolution of the galaxy that is being observed.

–We first focus on one of the most massive HVC complexes in our own Galaxy, Complex H, which seems to be at the point of interaction with the Galactic Disk.

–New observations of Complex H, taken during 2003-2004 and again in 2008-2009, were reduced and analyzed, which produced the highest-resolution HI observations of Complex H ever. Previous work from JL03 showed the velocity of the complex projected to the LSR in terms of l , b , and θ . We now calculate the velocity projected to the LSR but in terms of ϕ , the orbit angle which increases in a retrograde orbit, and i , the inclination of the orbit angle with respect to the Galactic plane. At the present time ϕ is equal to zero as the complex is crossing the Galactic plane, and $i = 50^\circ$, but it gives us an idea of the angle of the orbit that the complex follows through time if we suppose a circular orbit.

–We conclude that the mass of Complex H is one order of magnitude higher than previously thought ($4.6 \times 10^7 M_\odot$). The reason for this is the higher angular resolution of the observations that has allowed us to make a better separation between the Complex and the disk gas, and thus include more gas of the complex in the analysis which forms part of the tail structure.

–We have confirmed the initial deduction in JL03 that Complex H is moving with an average velocity of -200 km s^{-1} in the southeast direction, but with an angle inclined towards us, leaving a major wake of gas as it interacts with the gas in the disk of the Milky Way. Furthermore, the front of the main cloud is suffering a deceleration as it impinges on the

Galactic disk gas, and the interactive process is leaving zones of obviously enhanced turbulence throughout the cloud, in the main dense zone as well as in the tail.

–The new observations also show what seems to be a hidden part of the tail lying right behind the main body of the complex, and kinematic bridges between the cloud and Galactic emission not observed before, which are likely material stripped from either the cloud or the Milky Way itself. We interpret this as evidence of the interaction between the cloud and the gaseous halo of the Milky Way. Furthermore, the outer part of the Milky Way seems to be perturbed by the interaction with the complex. This all suggests us that the complex plunged into the outer parts of the Milky Way and accelerated previously present material, so the bridges observed belong most likely to Galactic gas.

–The implications of such a massive cloud belong to part of our future plan studies, but we will briefly mention a few. It seems very unlikely that Complex H is part of a fountain, for it is located nearly in the Galactic plane, but with a large negative forbidden velocity. Fountain material that was ejected from the disk only to fall back later, would not have such a large forbidden velocity at $b=0^\circ$. Also, the mass is much too large for a condensation from the fountain (Avillez 1999). The apparent lack of evidence for current star formation or evolved populations inside the complex place it as one of the most massive known neutral hydrogen clouds with no stars, and it has an HI mass and physical extent that are consistent with those of other Local Group galaxies. Therefore, it has been suggested before that Complex H is in fact a dark matter galaxy. But the complex does not seem to have rotation so it is hard to measure how much dark matter it could actually have. Another possible explanation for such a large massive cloud is that it is the sum of several HVCs which have collided. This is unlikely as we do not see strong shocks or any type of interaction. Perhaps Complex H is just another HVC like other HVCs observed in our Galaxy, which for some reason has a very large amount of gas.

–We then searched for HVCs in other galaxies using the THINGS survey, which has unique characteristics that has allowed us to perform for the first time such a deep search in HI. To separate genuine emission from noise in the final integrated HI maps, we consider only regions that show emission in two consecutive channels above a set level of 3σ in the data cubes, or three consecutive channels above a set level of 2σ .

–Among the 33 THINGS galaxies (M81 was excluded from the analysis, because the observed area was hardly free enough from emission to do a search for HVC candidates), we have found one candidate that fits our conditions well, and 3 candidates that fall at the limit of our detection criteria. They all have masses varying from 10^5 to $10^6 M_\odot$.

–One more object was found NGC 3621, which seems to have the properties of a dwarf galaxy. Its velocity map shows galactic kinematics typical of a dwarf galaxy. Its radius and circular velocity (not corrected for any inclination) give us a minimum dynamical mass of $\sim 4.54 \times 10^8 M_\odot$, whereas its flux gives us an estimated mass of $\sim 7.96 \times 10^7 M_\odot$. Both values agree well with the HI mass expected in dwarf spiral galaxies, which have $M_{\text{HI}} \leq 10^9 M_\odot$ (Schombert et al. 1995). Due to the fact that the cloud lies in projection close to (or is

on top of, so along the line of sight to) NGC 3621, it isn't possible to identify in direct optical imaging any optical counterpart. We plan to further study this object in future work.

–The candidate that fits well to our conditions lies at one of the furthest distances of the THINGS survey (14.1 Mpc), and since an object analogous to the Galactic HVC Complex C can probably not be detected at this distance, we might assume that this object has an even bigger size than this complex. Perhaps it could be some kind of tidal debris like the Magellanic Stream.

–If some of the HVCs in the Milky Way are the same as the objects we find here, some guidelines could be used determining the origin of our candidates, as we can see where the THINGS candidates are with respect to their parent galaxies. Candidates with distances larger than 10 kpc above the galactic disk are unlikely to be produced by galactic fountains (de Avillez 2000). The same applies to very massive HVCs, for the biggest shells observed in the largest HII regions are of the order of $10^5 M_{\odot}$. Some of the most massive candidates could be gas streams from satellites that have interacted with their host galaxy. Others could be condensed gas in the halo when close to the disk (Peek et al. 2007). The furthest candidates could be extragalactic clouds of diverse origin, but without a metallicity measurement it is hard to be certain. It must also be noted that in most cases it is not trivial to measure absolute distances between clouds and parent galaxies and only projected distances can be inferred.

–If we only take into account our positive detection, then we have found 1 big HVC out of 33 galaxies, which is what we would have expected from our calculations. But it seems strange that we did not find it in a more local galaxy from our sample. Our lack of detections in the nearest galaxies of the sample could mean that big HVCs like Complex C are not common in other galaxies. It is probable that most of the big HVCs that can be detected are a result of tidal debris interactions. As an example, this is probably the case in M81 where strong tidal interactions are present (Brinks et al. 2008). Most of the galaxies in our sample are isolated galaxies and therefore might lack these interactions. Still, we did find a possible dwarf galaxy in NGC 3621 so this possibility cannot be completely discarded.

–If we take into account our other three detections, then they are higher than the number that we expected to find and the implications would be completely different. We could then say that big and massive HVCs are more common than we thought and maybe our Galaxy is poor in big HVCs after all. Another possibility is that what we detected are not quite HVCs, but maybe bigger systems, perhaps dwarf galaxies of which the Galaxy has none. But this seems unlikely for as we mentioned, most of the galaxies in THINGS seem to be lonely galaxies with hardly any companions. Future studies in our work include testing how a tidal object like the Magellanic Stream would look like in the THINGS galaxies, and how an object like Complex C would look like at a more intermediate distance of our sample, like 7 Mpc for example.

–Even though the masses of our detections are not very large, comparing the structure that could be observed of Complex C if put at the distance of our targets, it is reasonable

to conclude that HI clouds in other galaxies can easily have total masses of the order of $10^6 M_\odot$, and perhaps even $10^7 M_\odot$, as is the case of Complex H. It is evident that having a good linear resolution and a good sensitivity is primordial to be able to make any detections, but with the present telescopes, this is not attainable yet. With the promise of new instruments, like the Square Kilometer Array (known as the SKA), better measurements will be possible and our understanding of the cold gas of galaxies and that in their immediate surroundings will be enhanced.

–The only candidate that we found to have a total mass of $10^7 M_\odot$, as Complex H does, turned out to be a probable dwarf galaxy because of its rotational velocity. We could therefore think that perhaps Complex H is a galaxy after all. Still, Complex H does not show any kind of rotation and that would make it a rarity among galaxies.

–Our results show that HVCs seem to be a common component in many galaxies. We observed one in detail in our own Milky Way and detected one more in another galaxy, with three other possible detections in other galaxies. Still, their total mass and distance to their parent galaxies seems to vary. We found masses ranging from 10^5 to $10^7 M_\odot$, and distances from 6 to 50 kpc in a projected plane on our HVC candidates, and 27 kpc in Complex H as previously proposed by JL03. Candidates with distances larger than 10 kpc above the galactic disk are unlikely to be produced by galactic fountains (de Avillez 2000). The same applies to very massive HVCs, for the biggest shells observed in the largest HII regions are of the order of $10^5 M_\odot$. Some of the most massive candidates could be gas streams from satellites that have interacted with their host galaxy. Others could be condensed gas in the halo when close to the disk (Peek et al. 2007). The furthest candidates could be extragalactic clouds of diverse origin. We find no evidence that our detections could not have an extragalactic origin, especially taking into account the furthest ones from their parent galaxies, as our positive detection shows (52 kpc). But even though our sample of galaxies seem to show no interaction with other galaxies, the possibility that we are looking at tidal interactions still exists. These results are showing us only the tip of the iceberg.

–Our observations agree with the numerical work done by Rand & Stone (1996) and Santillan et al. (2004). They showed that cloud-disk interactions can produce supershells as we have shown with the observations of Complex H, which seems to have swept part of the Galactic material along with it.

–We carried out an analytical study of the HVC-disk interaction with the purpose of learning the effects of such an interaction and how it changes in response to different phenomena occurring in the ISM. Our first step was to follow a sheet of material ejected from the plane, in the Galactic fountain scenario, reaching the Galactic atmosphere, cooling and then raining down on the disk. The trajectory that such material follows on its way towards the disk can also be applied to an HVC of extragalactic origin, whose trajectory is sheared.

–We then analyzed the stability of the gaseous disk when exposed to the perturbation provided by the exchange of momentum with a HVC. We performed several small perturbation analyses including different physical phenomena in order to find out whether or not

the interaction can lead pieces of the disk to the verge of gravitational instability. If so, then obtain a picture on how it happens.

–We included rotation and then shear in our system of equations. Our perturbation analysis showed that there is always a wavelength that renders the system unstable and that at most, rotation and shear only modify the Jeans criterion. In this scenario for the interaction, molecular clouds already on the verge of gravitational instability are not sheared away or disrupted by the impact of the HVC and can be compressed further. We then repeated the analysis but with the inclusion of magnetic fields. As a result we found that magnetic fields cannot prevent the HVC from compressing the medium to the verge of the gravitational instability.

–In all the processes that we considered, there is always a wave propagation mode that can lead the system to instability and that provides us with a modified version of the classical Jeans criterion. This interaction in turn would enable the star formation process due to the HVC-disk interaction and enhance the star formation rate on the disk.

–Due to our results in the analytical model, we believe that HVCs may have wide implications on galactic evolution, in agreement with our primary supposition that gas infall solves the chemical evolution/enrichment problem in the Milky Way.

–In order to be able to follow in an appropriate way the complex interaction that we have described, we need an appropriate model of the Galactic disk that includes sources that provide the ISM with energy, and which maintain it agitated. In future work, we pretend to use the model created by Avillez & Breitschwerdt (2004, 2005, 2007), which seems to be the most appropriate one for following the collision of HVCs with the Galactic disk. This, we hope, will allow us to obtain an appropriate image of the ISM and give us a further understanding about the nature of HVCs.

–With the arrival of new telescopes in the near and not so near future, we hope to perform better HI surveys that will allow us to find more HVC analogues in other galaxies. One of the most awaited instruments is with no doubt the SKA, which will allow us to image the local cosmic web down to $N_{\text{HI}} = 10^{16} \text{ cm}^{-2}$ (Braun 2007). With such powerful detections we will be able to observe a much deeper area around galaxies and gain a better sight of HVCs. Perhaps with more detailed information of their nature in other galaxies, which will allow us to overcome the distance determination problem, we will finally be able to understand their origin, and therefore, the creation and evolution of galaxies.

A

Calculation of HI masses

We briefly describe how to calculate HI masses from a data cube in map units of Jy/beam. We suppose that the Gauss function for the beam area in two dimensions can be represented as $G(x, y) = e^{-\frac{(x^2+y^2)}{2\sigma^2}}$. In one dimension, if we assume that the maximum height of the function is equal to one, or $H_{\max} = 1$, then the height of the full width at half maximum would be $1/2$, or $x_{\text{FWHM}} = 1/2$, so we can rewrite the exponential (again in one dimension) as:

$$e^{-\frac{(x_{\text{FWHM}})^2}{2\sigma^2}} = 1/2. \quad (\text{A.1})$$

and clearing for x_{FWHM} we get

$$-\frac{(x_{\text{FWHM}})^2}{2\sigma^2} = \ln(1/2)$$

$$x_{\text{FWHM}}^2 = -2\sigma^2 \ln(1/2) = 2\sigma^2 \ln(2)$$

$$x_{\text{FWHM}} = \sqrt{2\sigma^2 \ln(2)}. \quad (\text{A.2})$$

But x_{FWHM} is just the half part of the total FWHM, so the total one would be

$$\text{FWHM} = 2x_{\text{FWHM}} = 2\sqrt{2\sigma^2 \ln(2)} = \sqrt{8\sigma^2 \ln(2)} = \sigma\sqrt{8 \ln(2)}. \quad (\text{A.3})$$

and from here we can solve for σ

$$\sigma = \frac{\text{FWHM}}{\sqrt{8 \ln(2)}}. \quad (\text{A.4})$$

Now, back to two dimensions, if we approximate a cylinder to the Gauss, and integrate through it, we obtain the effective area on the sky, which is given by:

$$A_{\text{eff}} = \iint_{-\infty}^{\infty} G(x, y) dx dy = \iint_{-\infty}^{\infty} G(x, y) = e^{-\frac{(x^2+y^2)}{2\sigma^2}} dx dy = 2\pi\sigma^2 = 2\pi\sigma_{\alpha}\sigma_{\delta}, \quad (\text{A.5})$$

where σ_α and σ_δ represent both axis of σ in arcsecs. Combining Eqs. A.4 and A.5 gives us:

$$\begin{aligned}
 A_{\text{eff}} &= 2\pi\sigma_\alpha\sigma_\delta = 2\pi \left[\frac{\text{FWHM}_\alpha}{\sqrt{8\ln(2)}} \right] \left[\frac{\text{FWHM}_\delta}{\sqrt{8\ln(2)}} \right] \\
 &= 2\pi \frac{\Delta\alpha\Delta\delta}{8\ln(2)} = \frac{\pi}{4\ln(2)} \Delta\alpha\Delta\delta \\
 &= 1.133\Delta\alpha\Delta\delta.
 \end{aligned} \tag{A.6}$$

where $\Delta\alpha$ and $\Delta\delta$ are the FWHM along the major and minor axis of the telescope beam in radians, and the integration is made over the main beam.

Now, an integrated HI map is constructed by

$$S_{\text{HI}} = \sum_i S_i \Delta v$$

where S_i is the line emission in Jy/beam and Δv is the line full width at half maximum in km s^{-1} . Note that the sum over all the channels that contain the line emission. But if we want this in terms of the brightness temperature, T_{B} in units of K, we use the following relation:

$$S = \frac{2kT_{\text{B}}}{\lambda^2} A_{\text{eff}}, \tag{A.7}$$

where k is the Boltzman constant, and λ is the wavelength. So using Eq. A.6 this can be written as:

$$S = \frac{2kT_{\text{B}}}{\lambda^2} 1.133\Delta\alpha\Delta\delta. \tag{A.8}$$

Since we are observing in radio, the λ is equal to 0.21 m, and converting the FWHM back again to arcsecs we get:

$$\begin{aligned}
 S &= \frac{2(1.381 \times 10^{-23})T_{\text{B}}}{0.21^2} 1.133\Delta\alpha\Delta\delta \\
 &= 1.65 \times 10^{-3} T_{\text{B}} \sigma_\alpha \sigma_\delta.
 \end{aligned} \tag{A.9}$$

In other words, the ration between flux and temperature only depends on the telescope's instrumentation. Now, to get column densities the following relation is used:

$$N_{\text{HI}} = 1.823 \times 10^{18} \sum T_{\text{B},i} \Delta v \quad [\text{atom cm}^{-2}]. \tag{A.10}$$

We know that in order to convert this to units of $M_\odot \text{pc}^{-2}$ we can use the following relation:

$$1M_{\odot}\text{pc}^{-2} = 1.248 \times 10^{20} \text{ atom cm}^{-2}. \quad (\text{A.11})$$

Using both previous equations, we can calculate the mass as follows:

$$M_{\text{HI}} = \frac{1.823 \times 10^{18}}{1.248 \times 10^{20}} \sum T_{\text{B},i} \Delta v \Delta \alpha \Delta \delta, \quad (\text{A.12})$$

where $\Delta \alpha$ and $\Delta \delta$ are now given in parsecs. In order to calculate the size of an object in kpc, we just multiply the distance to the object times the angular size of the object in degrees with the corresponding transformation to radians:

$$d = D\theta = \theta \left(\frac{\pi}{180} \right) \left(\frac{1}{3600} \right) D \times 10^6. \quad (\text{A.13})$$

Applying this to the mass equation and using Eq. A.9 we get the following:

$$\begin{aligned} M_{\text{HI}} &= \frac{1.823 \times 10^{18}}{1.248 \times 10^{20}} \left[\frac{\pi \times D \times 10^6}{180 \times 3600} \right]^2 \sigma_{\alpha} \sigma_{\delta} \sum T_{\text{B},i} \Delta v \\ &= 1.46 \times 10^{-2} \left[\frac{\pi D \times 10^6}{180 \cdot 3600} \right]^2 \sigma_{\alpha} \sigma_{\delta} \sum T_{\text{B},i} \Delta v \\ &= 0.343 D^2 \sigma_{\alpha} \sigma_{\delta} \sum T_{\text{B},i} \Delta v, \end{aligned} \quad (\text{A.14})$$

where σ_{α} and σ_{δ} are in arcsecs. But from Eq. A.9 we know that

$$\sigma_{\alpha} \sigma_{\delta} \sum T_{\text{B},i} = \frac{\sum S_i \times 1.133}{1.65 \times 10^{-3}}. \quad (\text{A.15})$$

So Eq. A.14 becomes:

$$M_{\text{HI}} = 235 D^2 \sum S_i \Delta v \quad (\text{A.16})$$

and this is the total HI mass that we are looking for, given in M_{\odot} .

B

Python Boxcar

The following python program reads HVC data from a file and plots column densities in a selected celestial area. “Figure” 1 is plotted with the raw data, whereas “Figure 2” plots the same region after subjected the data plotted in “Figure 1” to a boxcar convolution. An example of this can be seen in Fig. 3.14 and Fig. 3.15.

```
# imports
import string
import matplotlib.pyplot as plt
from numpy import *
from matplotlib import *
from matplotlib.mlab import griddata
from numpy.ma import filled

# input parameters
nx=69 # dimensions of the low resolution grid
ny=24 # - grid size should correspond to data point density in observations
nxb=1150 # dimensions of the high resolution grid
nyb=400 # - may have any values, the higher the smoother plot
nlevels=1000 # number of levels to use in contour plotting, should be high
lonlims=[60,137] # limits in longitude of area to plot: min, max
latlims=[27,60] # limits in latitude of area to plot: min, max
breakoff=[2.5e+19,9.82e+19] # limit in column density to measure against
# in area approximation
boxsize=5 # size of the smoothing buffer in the boxcar algorithm
margin=10 # width of additional area around the plotted box, in all
# directions these data points are not shown directly and
# only used to improve interpolation

# definitions
labels=[]
first=[]
```

```

second=[]
third=[]
tmp=[]
tmpb=[]
tmpbcut=[]
over=0
under=0
over2=0
under2=0
arr3ibcut=array([])
box1=[]
box2=[]
box3=[]

# opening and reading of file contents, then splitting them
# into one long sequence of values, all types mixed
f=open('TableComplexC2.txt','r')
unsorted=f.read()
splitup=unsorted.split()

# converting table values from string type to floats
# (skipping the labels in the first row)
for i in range(len(splitup)):
    if i>2:
        splitup[i]=float(splitup[i])

lines=len(splitup)/3

# linewise for the input file, pass each value to an appropriate list,
# one for each column
# the input data is in one long sequence, but the 3*i+x loop
# conditions read the entries like they were
# on different lines in the input file
for i in range(lines):
    if i==0:    # labels line
        labels.append(splitup[i]) # read in column labels to 'labels' list
        labels.append(splitup[i+1])
        labels.append(splitup[i+2])
    elif (splitup[3*i] >= (lonlims[0]-margin) and splitup[3*i]
          <= (lonlims[1]+margin) and splitup[3*i+1] >=
              (latlims[0]-margin) and splitup[3*i+1] <= (latlims[1]+margin)):
# reads in only values in plotting box plus margins
        first.append(splitup[3*i])
# appends value in first column, on row i+1, to 'first' list
        second.append(splitup[3*i+1])

```

```
# appends value in second column, on row i+1, to 'second' list
    third.append(splitup[3*i+2])
# appends value in third column, on row i+1, to 'third' list

# converting lists to arrays, for mathematical treatment
arr1=array(first)
arr2=array(second)
arr3=2*array(third) # factor 2 simulates different HVC

###
### interpolation in the low resolution grid
###
#
# interpolating to create an evenly spaced (low resolution) grid
arr1i=linspace(min(arr1),max(arr1),nx) # "x values", longitude, 1D array
arr2i=linspace(min(arr2),max(arr2),ny) # "y values", latitude, 1D array
arr3i=griddata(arr1,arr2,arr3,arr1i,arr2i) # the interpolation command
# itself, outputs column densities in a 2D array

# uncomment the following line to convert arr3i from a masked array
# to a simple one
# this replaces grid points without data with a given constant value (=0)
#arr3i=filled(arr3i,0)

# reading in all real data values in arr3i (exclude possible artificial
# zeros from the preceding line)
for i in range(len(arr3i)):
    for j in range(len(arr3i)):
        if arr3i[i,j]>1:
            tmp.append(arr3i[i,j])

# finding min and max values in the column density array
minval=min(tmp)
maxval=arr3i.max()

# creating 1D arrays for contour levels to plot, and ticks to show
# in the color bar, respectively
levels=linspace(minval,maxval,nlevels) # contour levels
blevels=linspace(minval,maxval,10) # color bar ticks, "10" is the number
# of ticks desired

###
### interpolation in the high resolution grid
### this procedure is analogous to the low resolution case
###
```

```
#

arr1ib=linspace(min(arr1),max(arr1),nxb)
arr2ib=linspace(min(arr2),max(arr2),nyb)
arr3ib=griddata(arr1,arr2,arr3,arr1ib,arr2ib)

arr3ib=filled(arr3ib,0)

for i in range(len(arr3ib)):
    for j in range(len(arr3ib)):
        if arr3ib[i,j]>1:
            tmpb.append(arr3ib[i,j])

minval=min(tmpb)
maxval=arr3ib.max()

levelsb=linspace(minval,maxval,nlevels)
blevelsb=linspace(minval,maxval,10)

# cutting the margins off the high resolution version to plot only
# the longlimits, latlimits region

arr3ibcut=arr3ib

for i in range(nyb): # marking all values outside of desired region
# by setting to 0
    for j in range(nxb):
        if (arr1ib[j] >= lonlims[0] and arr1ib[j]
<= lonlims[1] and arr2ib[i] >= latlims[0] and
arr2ib[i] <= latlims[1]):
            arr3ibcut[i,j]=arr3ib[i,j]
        else:
            arr3ibcut[i,j]=0

for i in range(len(arr3ibcut)): # reading only relevant (unmarked) values
# into temporary list
    for j in range(len(arr3ibcut)): # to determine min and max column
# densities for desired region
        if arr3ibcut[i,j]>1:
            tmpbcut.append(arr3ibcut[i,j])

# finding min and max values of new, trimmed, region
minval=min(tmpbcut)
maxval=arr3ibcut.max()
```

```
# setting contour plot and color bar levels, as before,
# but for trimmed region
levelsbcut=linspace(minval,maxval,nlevels)
blevelsbcut=linspace(minval,maxval,10)

# uncomment the following line to plot logarithmic column densities
# (may require other changes)
#arr3i=log10(arr3i)

# plot in Figure 1, using appropriate dimensions
plt.figure(1,figsize=(18.0,7.7))
plt.clf()

### uncomment the following three lines to plot the low resolution
### case (instead of high res; this is non-default)
#plt.contourf(arr1i,arr2i,arr3i,levels,cmap=cm.jet)
# create contour plot
#plt.colorbar(format='%.2e',ticks=blevels) # add color bar
#tit1='CompC, original, '+str(nx)+'x'+str(ny)+' grid'
# set title with some information

### uncomment the following three lines to plot the high resolution
### case (instead of low res; this is default)
plt.contourf(arr1ib,arr2ib,arr3ibcut,levelsbcut,cmap=cm.jet)
# create contour plot
plt.colorbar(format='%.2e',ticks=blevelsbcut) # add color bar
tit1='CompC, original, '+str(nxb)+'x'+str(nyb)+' grid'
# set title with some information

### uncomment the following three lines to plot as image instead
### of contour plot (replaces above two blocks)
#plt.imshow(arr3i,extent=(max(arr1i),min(arr1i),min(arr2i),max(arr2i)),
aspect='equal',cmap=cm.jet)
#plt.imshow(arr3i,extent=(min(arr1i),max(arr1i),min(arr2i),max(arr2i)),
aspect='equal',cmap=cm.jet)
#plt.imshow(arr3i,cmap=cm.jet)

# setting plot window to show only the region specified by longlims and latlims
plt.xlim(lonlims[1],lonlims[0]) # reverses the direction of the longitude axis
plt.ylim(latlims[0],latlims[1])

# adding grid, title and labels
plt.grid(color='b') # b = blue, w = white, r = red, etc
plt.title(tit1) # adding previously set title to the plot
plt.xlabel('Galactic Longitude (degrees)') # labelling horizontal axis
```

```

plt.ylabel('Galactic Latitude (degrees)') # labelling vertical axis

### uncomment the following block to apply area approximation to the low
# resolution grid (non-default)
#for i in range(ny):
#    for j in range(nx):
#        if arr3i[i,j]>1:
#            if arr3i[i,j]>breakoff[0]:
#                over+=1
#            else:
#                under+=1

### uncomment the following block to apply area approximation to the high
# resolution grid (default)
# checking for each point in the grid whether it is above or below the limit
# (breakoff variable)
for i in range(nyb):
    for j in range(nxb):
        if (arr3ib[i,j]>1 and arr1ib[j] >= lonlims[0] and arr1ib[j] <= lonlims[1]
and arr2ib[i] >= latlims[0] and arr2ib[i] <= latlims[1]):
            if arr3ib[i,j]>breakoff[0]:
                over+=1
            else:
                under+=1

# presenting area approximation results
print "original image, density limit:", breakoff[0]
print "hits over: ", over, "(",(float(over)/float(over+under))*100,"%)"
print "hits under: ", under, "(",(float(under)/float(over+under))*100,"%)"

# executing boxcar.py file to get access to the boxcar function
execfile('boxcar.py')

# calling the boxcar function to smoothen the column density array
# the boxcar smoothing should always be applied to the low resolution
# grid case,
# the resolution of which is chosen to correspond properly to the raw data
arr3ibox=boxcar(arr3i,boxsize)

# reformatting the smoothened low resolution grid data for the
# second interpolation
# the data is broken apart into three 1D array, like the original input
for i in range(nx):
    for j in range(ny):
        box1.append(arr1i[i])

```

```
        box2.append(arr2i[j])
        box3.append(arr3ibox[j,i])

# interpolation of the smoothened low resolution grid data to higher
# resolution, analogous to above
arr1iboxb=linspace(min(box1),max(box1),nxb)
arr2iboxb=linspace(min(box2),max(box2),nyb)
arr3iboxb=griddata(box1,box2,box3,arr1iboxb,arr2iboxb)

# uncomment to unmask the column density array, as above
#arr3iboxb=filled(arr3iboxb,0)

# plot in Figure 2
plt.figure(2,figsize=(18.0,7.7))
plt.clf()

### uncomment the following block to plot the smoothened low resolution
# case, without second interpolation
#plt.contourf(arr1i,arr2i,arr3ibox,levels,cmap=cm.jet)
#plt.colorbar(format='%.2e',ticks=blevels)
#tit2='CompC, convolved, box size '+str(boxsize)+'',
#      '+str(nx)+'x'+str(ny)+' grid'

### uncomment the following block to plot the smoothened case,
### interpolated to higher resolution
plt.contourf(arr1iboxb,arr2iboxb,arr3iboxb,levelsbcut,cmap=cm.jet)
plt.colorbar(format='%.2e',ticks=blevelsbcut)
tit2='CompC, convolved, box size '+str(boxsize)+'',
'+str(nxb)+'x'+str(nyb)+' grid'

# setting plot window limits
plt.xlim(lonlims[1],lonlims[0]) # reversing horizontal axis
plt.ylim(latlims[0],latlims[1])

# adding grid, title and labels
plt.grid(color='b')
plt.title(tit2)
plt.xlabel('Galactic Longitude (degrees)') # labelling horizontal axis
plt.ylabel('Galactic Latitude (degrees)') # labelling vertical axis

### uncomment the following block to perform area estimate on the
### smoothened low resolution case (with second intrp)
#for i in range(ny):
#    for j in range(nx):
#        if arr3ibox[i,j]>1:
```

```

#         if arr3ibox[i,j]>breakoff[1]:
#             over+=1
#         else:
#             under+=1

### uncomment the following block to perform area estimate on the
### smoothed case with second interpolation
for i in range(nyb):
    for j in range(nxb):
        if arr3iboxb[i,j]>1:
            if (arr3iboxb[i,j]>breakoff[1] and arr1iboxb[j] >= lonlims[0] and arr1iboxb[j]
<= lonlims[1] and arr2iboxb[i] >= latlims[0] and arr2iboxb[i] <= latlims[1]):
                over2+=1
            else:
                under2+=1

# presenting area estimate results
print "convolved image, density limit:", breakoff[1]
print "hits over: ", over2, "(",(float(over2)/float(over2+under2))
*100,"%)"
print "hits under: ", under2, "(",(float(under2)/float(over2+under2))
*100,"%)"

# the below command is probably only needed once per python session (?)
#plt.show()

```

The module needed to do the boxcar, called boxcar.py, is:

```

# importing required module
from numpy import *

def boxcar(nat,boxsize):

    if boxsize%2==1: # testing size of smoothing box
        print "boxsize OK"
    else:
        print "invalid boxsize, must be uneven integer"
        return

    natarr=array(nat) # ensure input is array

    rows=natarr.shape[0] # count number of rows in input
    cols=natarr.shape[1] # count number of columns in input

    natex=zeros([rows+boxsize-1,cols+boxsize-1])

```

```
# define expanded array, including ghost cells

    for i in range(rows):
        for j in range(cols):
            natex[i+boxsize/2,j+boxsize/2]=natarr[i,j]
# copy over non-ghost cells to expanded array

    for j in range(cols+boxsize-1):
        for i in range(boxsize/2):
            natex[i,j]=natex[boxsize/2,j]
# copy top row real values upwards into ghost cells
    for i in range(boxsize/2):
        natex[rows+boxsize/2+i,j]=natex[rows+boxsize/2-1,j]
# copy bottom row real values downwards into ghost cells

    for i in range(rows+boxsize-1):
        for j in range(boxsize/2):
            natex[i,j]=natex[i,boxsize/2]
# copy leftmost column leftwards into ghost cells
    for j in range(boxsize/2):
        natex[i,cols+boxsize/2+j]=natex[i,cols+boxsize/2-1]
# copy rightmost column rightwards into ghost cells

    mask=zeros([boxsize,boxsize]) # define smoothing mask
    boxed=zeros([rows,cols]) # define output array, without ghost cells

    for i in range(rows):
# for each point in the array, calculate average of mask
        for j in range(cols):
# and set this as the new value
            for k in range(boxsize):
# i, j are horizontal and vertical coordinates of the array
                for l in range(boxsize):
# k, l are horizontal and vertical coordinates of the mask
                    mask[k,l]=natex[i+k,j+l]
                    boxed[i,j]=average(mask)

    return boxed # return the smoothed array as output
```

C

Perpendicular Acceleration

We will calculate the perpendicular acceleration of an object falling into the Galactic disk in 1D, being sheared by the differential rotation of the disk. If we apply the Taylor series to $g(z)$ in the disk vicinity, we get

$$g_{\perp} \equiv g(z) \approx g(z + \Delta z) \approx g(z = 0) + \Delta z g'(\Delta z) + \dots$$

So the best approximation to $g(z)$ in the disk vicinity is simply $g_{\perp} = g(z = 0)$, which means that the gravity perpendicular to the disk, when close to it, is that of the disk. So according to the potential for population I there are two contributions, one is given by the logarithm of R_*/ϖ , and the other one is proportional to the inverse of the hyperbolic sine, which is defined as $\sinh(x) = (e^x - e^{-x})/2$. Both contributions are different in the sense that one is proportional to the radius (the one depending only on r), and the other one is proportional to the inverse of an exponential (the one depending on z).

The exponential can be written as

$$e^x = 1 + x + x^2/2\dots$$

and the inverse hyperbolic sine as

$$(e^x - e^{-x})/2.$$

We can see that the hyperbolic sine will be proportional to $\approx e^x/2$ at a low order where we can ignore the negative exponential, which means that if we increase the potential as $\Delta\varpi$, at a very low order the contribution in z will increase as much as that in the radial direction, but divided by two, so we can write the equation for the centrifugal equilibrium in the radial direction, as

$$-g_{\perp} = \frac{V^2}{2\varpi} \tag{C.1}$$

which can also be written as

$$-g_{\perp} = \frac{V^2}{2R_*}, \tag{C.2}$$

where R_* is the distance from the Sun to the Galactic center.

D

Small Perturbations Analysis For An Infinite Thick Disk With Uniform Rotation

We will now calculate a linear analysis of small perturbations which will give us the dispersion equation for the case of a thick disk with uniform rotation. If we introduce small perturbations on the system of equations and we retain only perturbed quantities, we end up with the following relations

$$\frac{\partial \delta \rho}{\partial t} + \rho_0 \nabla \cdot \delta v = 0 \quad (\text{D.1})$$

$$\rho_0 \frac{\partial \delta v}{\partial t} = 2\rho_0 (\delta v \times \Omega) - \nabla \delta P - \rho_0 \nabla \delta \psi \pm (0, 0, \frac{\delta \rho V_{HVC}^2 10^{-10}}{3d}) \quad (\text{D.2})$$

$$\nabla^2 \delta \psi = -4\pi G \delta \rho. \quad (\text{D.3})$$

We now suppose that the medium rotates at a constant speed around the z axis, that is, $\Omega = (0, 0, \Omega)$. Since we are interested in wave solutions that only propagate in the vertical direction, we then consider $\frac{\partial}{\partial z} \neq 0$.

We now need to obtain the perturbed equations in the x, y, z components for the first term in Eq. D.2:

$$\begin{aligned} 2\rho_0 (\delta v \times \Omega) &= 2\rho \begin{bmatrix} i & j & k \\ \delta v_x & \delta v_y & \delta v_z \\ 0 & 0 & \Omega \end{bmatrix} \\ &= 2\rho_0 [\hat{i}(\Omega \delta v_y) - \hat{j}(\Omega \delta v_x) - \hat{k}(0)]. \end{aligned}$$

The components of Eq. D.2 then become:

$$\rho_0 \frac{\partial \delta v_x}{\partial t} = 2\rho_0 \Omega \delta v_y \Rightarrow \frac{\partial \delta v_x}{\partial t} - 2\Omega \delta v_y = 0 \quad (\text{D.4})$$

$$\rho_0 \frac{\partial \delta v_y}{\partial t} = 2\rho_0 \Omega \delta v_x \Rightarrow \frac{\partial \delta v_y}{\partial t} - 2\Omega \delta v_x = 0 \quad (\text{D.5})$$

$$\rho_0 \frac{\partial \delta v_z}{\partial t} = -\frac{\partial \delta P}{\partial z} - \rho_0 \frac{\partial \delta \psi}{\partial z} \pm \frac{\delta \rho V_{HVC}^2}{3d} 10^{-4}$$

and taking into account that $\delta P = c^2 \delta \rho$, the equations become:

$$\frac{\partial \delta \rho}{\partial t} + \rho_0 \frac{\partial \delta v_z}{\partial z} = 0 \quad (D.6)$$

$$\frac{\partial \delta v_z}{\partial t} + \frac{c^2}{\rho_0} \frac{\partial \delta \rho}{\partial z} \pm \frac{\delta \rho V_{HVC}^2 10^{-4}}{3d \rho_0} + \frac{\partial \delta \psi}{\partial z} = 0 \quad (D.7)$$

$$\frac{\partial^2 \delta \psi}{\partial z^2} + 4\pi G \delta \rho = 0. \quad (D.8)$$

In order to analyze the wave propagation through the medium and find when it becomes unstable, we assume that the perturbations $\delta v_x, \delta v_y, \delta v_z, \delta \rho, \delta \psi$ are of the form $f(z, t) = e^{i(kz+wt)}$, so that $\frac{\partial}{\partial z} = ik$ and $\frac{\partial}{\partial t} = iw$. The system of equations D.4 -D.8 is reduced to:

$$iw\delta v_x - 2\Omega\delta v_y = 0$$

$$iw\delta v_y + 2\Omega\delta v_x = 0$$

$$iw\delta v_z + ik \frac{c^2}{\rho_0} \delta \rho \pm \frac{\delta \rho V_{HVC}^2 10^{-4}}{3d} + ik\delta \psi = 0$$

$$iw\delta \rho + ik\rho_0\delta v_z = 0$$

$$-k^2\delta \psi - 4\pi G\delta \rho = 0.$$

In order to find the solution of this system of equations we have to calculate the determinant of the system and equal it to 0, thus

$$|A| = 0 \longrightarrow (-w^2 + 4\Omega^2)(-w^2 + k^2c^2 - 4\pi G)ik^2 = 0, \quad (D.9)$$

whose solution gives us the propagation wave modes

$$w_1 = \pm 2\Omega$$

$$w_2 = \pm \left(k^2c^2 - 4\pi G \mp \frac{V_{HVC}^2 10^{-4} k}{3d} \right)^{1/2} = 0.$$

E

Small Perturbations Analysis For A Thick Disk With Magnetic Fields

We do here an analysis of linear perturbations for the case of a magnetized disk, which will give us the respective dispersion equation. The first term to be linearized is the magnetic tension:

$$\frac{1}{4\pi}(B \cdot \nabla)B. \quad (\text{E.1})$$

If we perturb this equation we end up with the expression:

$$\frac{1}{4\pi}((B + \delta B) \cdot \nabla)(B + \delta B). \quad (\text{E.2})$$

If we rewrite this equation in components we have:

$$\begin{aligned} \frac{1}{4\pi}((B + \delta B) \cdot \nabla)(B + \delta B) &= \frac{1}{4\pi} \left((B_x + \delta B_x) \frac{\partial}{\partial x} (B_x + \delta B_x) + \right. \\ &(B_y + \delta B_y) \frac{\partial}{\partial y} (B_x + \delta B_x) + (B_z + \delta B_z) \frac{\partial}{\partial z} (B_x + \delta B_x) \Big) \hat{i} + \\ &\left((B_x + \delta B_x) \frac{\partial}{\partial x} (B_y + \delta B_y) + (B_y + \delta B_y) \frac{\partial}{\partial y} (B_y + \delta B_y) + (B_z + \delta B_z) \frac{\partial}{\partial z} (B_y + \delta B_y) \right) \hat{j} \\ &\left((B_x + \delta B_x) \frac{\partial}{\partial x} (B_z + \delta B_z) + (B_y + \delta B_y) \frac{\partial}{\partial y} (B_z + \delta B_z) + (B_z + \delta B_z) \frac{\partial}{\partial z} (B_z + \delta B_z) \right) \hat{k}. \end{aligned}$$

We will now suppose that $B = (0, B_y, B_z)$. What we want with this supposition is to think that we are standing in a three-dimensional slice of the Galaxy, away from the center, and that the “y” axis represents the azimuthal coordinate, so saying that $B_x = 0$ is the same as saying that the field in the radial direction is zero. We can make this supposition to simplify our calculations without losing generality. We will also suppose that $B_y = \text{constant}$ and $B_z = \text{constant}$, which actually means that the scale of the box in which we are studying the field does not change in magnitude, or changes very slowly. This implies

that any derivative in B_y and B_z will be zero. If we linearize the previous equation and take into account the suppositions made, we obtain:

$$\begin{aligned} \frac{1}{4\pi}((B + \delta B) \cdot \nabla)(B + \delta B) &= \frac{1}{4\pi}((B_y \frac{\partial}{\partial y} \delta B_x + B_z \frac{\partial}{\partial z} \delta B_x) \hat{i} + \\ &(B_y \frac{\partial}{\partial y} \delta B_y + B_z \frac{\partial}{\partial z} \delta B_y) \hat{j} + (B_y \frac{\partial}{\partial y} \delta B_z + B_z \frac{\partial}{\partial z} \delta B_z) \hat{k}). \end{aligned}$$

Now we will linearize the magnetic pressure term

$$\frac{1}{8\pi} \nabla B^2. \quad (\text{E.3})$$

When we perturbate this term we end up with

$$\begin{aligned} \frac{1}{8\pi}(\nabla(B + \delta B)^2) &= \frac{1}{8\pi}(\frac{\partial}{\partial x}((B_x + \delta B_x)^2 + (B_y + \delta B_y)^2 + (B_z + \delta B_z)^2), \frac{\partial}{\partial y}((B_x + \delta B_x)^2 \\ &+ (B_y + \delta B_y)^2 + (B_z + \delta B_z)^2), \frac{\partial}{\partial z}((B_x + \delta B_x)^2 + (B_y + \delta B_y)^2 + (B_z + \delta B_z)^2)) = \\ &\frac{1}{8\pi}(\frac{\partial}{\partial x}(2B_x \delta B_x + 2B_y \delta B_y + 2B_z \delta B_z), \frac{\partial}{\partial y}(2B_x \delta B_x + 2B_y \delta B_y + 2B_z \delta B_z), \\ &\frac{\partial}{\partial z}(2B_x \delta B_x + 2B_y \delta B_y + 2B_z \delta B_z)). \end{aligned}$$

Recalling that we imposed $B_x = 0$ and that the derivative $B_y = B_z = 0$, the equation above can be reduced to:

$$\begin{aligned} \frac{1}{8\pi}(\nabla(B + \delta B)^2) &= \frac{1}{8\pi}(2B_y \frac{\partial}{\partial x} \delta B_y + 2B_z \frac{\partial}{\partial x} \delta B_z, \\ &2B_y \frac{\partial}{\partial y} \delta B_y + 2B_z \frac{\partial}{\partial y} \delta B_z, 2B_y \frac{\partial}{\partial z} \delta B_y + 2B_z \frac{\partial}{\partial z} \delta B_z). \end{aligned}$$

We can obtain the perturbed magnetic terms of the moment equation from subtracting these two equations, which would give us:

$$\begin{aligned} \frac{1}{4\pi}((B + \delta B) \cdot \nabla)(B + \delta B) - \frac{1}{8\pi}(\nabla(B + \delta B)^2) &= \\ \frac{1}{4\pi}(B_y(\frac{\partial}{\partial y} \delta B_x - \frac{\partial}{\partial x} \delta B_y) + B_z(\frac{\partial}{\partial z} \delta B_x - \frac{\partial}{\partial x} \delta B_z), \\ B_z(\frac{\partial}{\partial z} \delta B_y - \frac{\partial}{\partial y} \delta B_z), B_y(\frac{\partial}{\partial y} \delta B_z - \frac{\partial}{\partial z} \delta B_y)). \end{aligned}$$

We derive solutions corresponding to waves that propagate in the z -direction only since the phenomenon that interests us occurs principally in the vertical direction. The magnetic terms of the moment equation are then written as:

$$\begin{aligned} & \frac{1}{4\pi}((B + \delta B) \cdot \nabla)(B + \delta B) - \frac{1}{8\pi}(\nabla(B + \delta B)^2) = \\ & \frac{1}{4\pi} \left(B_z \frac{\partial}{\partial z} \delta B_x, B_z \frac{\partial}{\partial z} \delta B_y, -B_y \frac{\partial}{\partial z} \delta B_y \right). \end{aligned}$$

Now we begin to linearize the induction equation, which tells us that the magnetic field is able to alter the velocity of the fluid and that a change in the fluid's velocity alters the field. The perturbed induction equation, with two coupled variables, would be:

$$\frac{\partial(B + \delta B)}{\partial t} = \nabla \times ((u + \delta u) \times (B + \delta B)). \quad (\text{E.4})$$

Now, we also suppose that initially the velocity of the non-perturbed fluid is zero in its three components, u_x , u_y y u_z , respectively. The left side of this equation is linear, so we end up with just one term $\partial\delta B/\partial t$. Thus we concentrate on the right side now. If the initial velocity of the fluid is zero, we can analyze the cross product and get the rotational of

$$\begin{aligned} & \nabla \times ((\hat{i}(u_y(B_z + \delta B_z) - u_z(B_y + \delta B_y)), \hat{j}(u_z\delta B_x - u_x(B_z + \delta B_z)), \\ & \hat{k}(u_x(B_y + \delta B_y) - u_y\delta B_x))). \end{aligned}$$

Taking away the quadratic terms we get:

$$\nabla \times \left(\hat{i}(u_y B_z - u_z B_y), \hat{j}(-u_x B_z), \hat{k}(u_x B_y) \right). \quad (\text{E.5})$$

Finally, by taking the rotational of this expression we obtain:

$$\hat{i} \left(\frac{\partial}{\partial y} u_x B_y + \frac{\partial}{\partial z} u_x B_z \right), \hat{j} \left(\frac{\partial}{\partial z} (u_y B_z - u_z B_y) - \frac{\partial}{\partial x} u_x B_y \right), \quad (\text{E.6})$$

$$\hat{k} \left(-\frac{\partial}{\partial x} u_x B_z - \frac{\partial}{\partial y} (u_y B_z - u_z B_y) \right) \quad (\text{E.7})$$

and as we already established before, we are only interested in the phenomena that occur in the vertical direction, we only consider the derivative with respect to z to be different from zero, and the above equation can be simplified to:

$$\hat{i} \left(\frac{\partial}{\partial z} u_x B_z \right), \hat{j} \left(\frac{\partial}{\partial z} (u_y B_z - u_z B_y) \right), 0\hat{k}. \quad (\text{E.8})$$

The linearized induction equation can now be written as:

$$\frac{\partial(\delta B_x, \delta B_y, \delta B_z)}{\partial t} = \hat{i} \left(\frac{\partial}{\partial z} u_x B_z \right), \hat{j} \left(\frac{\partial}{\partial z} (u_y B_z - u_z B_y) \right), 0\hat{k}. \quad (\text{E.9})$$

F

Bibliography

References

- Audouze, J., Lequeux, J., & Vigroux, L. 1976, *Memoires of the Societe Royale des Sciences de Liege*, 9, 477
- Asplund, M., Grevesse, N., & Sauval, A. J. 2005, *Cosmic Abundances as Records of Stellar Evolution and Nucleosynthesis*, 336, 25
- de Avillez, M. A. 1999, *Stromlo Workshop on High-Velocity Clouds*, 166, 103
- de Avillez, M. A. 2000, *MNRAS*, 315, 479
- de Avillez, M. A., & Breitschwerdt, D. 2004, *A&A*, 425, 899
- de Avillez, M. A., & Breitschwerdt, D. 2005, *A&A*, 436, 585
- Balsara, D. S. 2001, *Journal of Computational Physics*, 174, 614
- Barry, D. C. 1988, *ApJ*, 334, 436
- Binney, J., & May, A. 1986, *MNRAS*, 218, 743
- Binney, J., Jiang, I.-G., & Dutta, S. 1998, *MNRAS*, 297, 1237
- Binney, J., Dehnen, W., & Bertelli, G. 2000, *MNRAS*, 318, 658
- Binney, J. J. 2000, *Dynamics of Galaxies: from the Early Universe to the Present*, 197, 107
- Bland-Hawthorn, J. 2009, *IAU Symposium*, 254, 241
- Blitz, L., Spergel, D. N., Teuben, P. J., Hartmann, D., & Burton, W. B. 1999, *ApJ*, 514, 818
- Boomsma, R., Oosterloo, T. A., Fraternali, F., van der Hulst, J. M., & Sancisi, R. 2005a, *Extra-Planar Gas*, 331, 247
- Boomsma, R., Oosterloo, T. A., Fraternali, F., van der Hulst, J. M., & Sancisi, R. 2005b, *A&A*, 431, 65
- Boomsma, R., Oosterloo, T. A., Fraternali, F., van der Hulst, J. M., & Sancisi, R. 2008, *A&A*, 490, 555
- Bond, J. R., Cole, S., Efstathiou, G., & Kaiser, N. 1991, *ApJ*, 379, 440
- Bournaud, F., & Combes, F. 2002, *A&A*, 392, 83
- Braun, R., & Burton, W. B. 1999, *A&A*, 341, 437

- Braun, R. 2007, arXiv:astro-ph/0703746
- Bregman, J. N. 1980, ApJ, 236, 577
- Briggs, F. H. 1990, ApJ, 352, 15
- Brinks, E., & Burton, W. B. 1984, A&A, 141, 195
- Brinks, E., Walter, F., & Skillman, E. D. 2008, IAU Symposium, 244, 120
- Brüns, C., Kerp, J., Kalberla, P. M. W., & Mebold, U. 2000, A&A, 357, 120
- Cappellaro, E., Evans, R., & Turatto, M. 1999, A&A, 351, 459
- Carney, B. W., Latham, D. W., & Laird, J. B. 1990, AJ, 99, 572
- Casuso, E., & Beckman, J. E. 1997, ApJ, 475, 155
- Casuso, E., & Beckman, J. E. 1999, AJ, 118, 1907
- Casuso, E., & Beckman, J. E. 2000, PASP, 112, 942
- Casuso, E., & Beckman, J. E. 2001, ApJ, 557, 681
- Casuso, E., & Beckman, J. E. 2003, PASJ, 55, 247
- Casuso, E., & Beckman, J. E. 2006, Ap&SS, 306, 139
- Casuso, E., Beckman, J. E., & Buenrostro, V. 2006, PASP, 118, 833
- Chandrasekhar, S. 1953, ApJ, 195, 119
- Comeron, F., & Torra, J. 1992, A&A, 261, 94
- Comeron, F., & Torra, J. 1994, A&A, 281, 35
- Colella, P., Woodward, P. 1984, J.Comp.Phys., 54, 174
- Dai W., & Woodward, P. R. 1994, J. Comput. Phys., 115, 485
- Dai W., & Woodward, P. R. 1998, J. Comput. Phys., 142, 331
- Dalcanton, J. 2006, Bulletin of the American Astronomical Society, 38, 1063
- Dalcanton, J. J. 2007, ApJ, 658, 941
- Dalgarno, A., & McCray, R. A. 1972, ARA&A, 10, 375
- Danly, L., Albert, C. E., & Kuntz, K. D. 1993, ApJ, 416, L29
- de Boer, K. S., Altan, A. Z., Bomans, D. J., Lilienthal, D., Moehler, S., van Woerden, H., Wakker
- Dekel, A., & Birnboim, Y. 2006, MNRAS, 368, 2
- Dieter, N. H. 1971, A&A, 12, 59
- Drake, J. J., & Testa, P. 2005, Nature, 436, 525
- Elmegreen, B. G. 2007, Island Universes - Structure and Evolution of Disk Galaxies, 163
- Favata, F., Micela, G., & Sciortino, S. 1997, A&A, 323, 809
- Feltzing, S., Holmberg, J., & Hurley, J. R. 2001, A&A, 377, 911
- Flynn, C., & Morell, O. 1997, MNRAS, 286, 617

- Ferrière, K. M. 2001, *Reviews of Modern Physics*, 73, 1031
- Fraternali, F., Oosterloo, T., Sancisi, R., & van Moorsel, G. 2001, *ApJ*, 562, L47
- Fraternali, F., van Moorsel, G., Sancisi, R., & Oosterloo, T. 2002, *AJ*, 123, 3124
- Fraternali, F., & Binney, J. J. 2006, *MNRAS*, 366, 449
- Freeman, K. C. 1987, *ARA&A*, 25, 603
- Friedman, S. D., et al. 2002, *ApJS*, 140, 37
- Fukugita, M., & Peebles, P. J. E. 2004, *ApJ*, 616, 643
- García López, R. J., Israelian, G., Rebolo, R., Bonifacio, P., Molaro, P., Basri, G., & Shchukina, N. 2001, *New Astronomy Review*, 45, 519
- Gardiner, L. T., & Noguchi, M. 1996, *MNRAS*, 278, 191
- Grossi, M., Giovanardi, C., Corbelli, E., Giovanelli, R., Haynes, M. P., Martin, A. M., Saintonge, A., & Dowell, J. D. 2008, *A&A*, 487, 161
- Hébrard, G., et al. 2002, *Planet. Space Sci.*, 50, 1169
- Heiles, C. 1979, *ApJ*, 229, 533
- Huang, R. Q., & Weigert, A. 1982, *A&A*, 112, 281
- Hulsbosch, A. N. M. 1971, *A&A*, 14, 489
- Hulsbosch, A. N. M., & Wakker, B. P. 1988, *A&AS*, 75, 191
- Hunt, R., & Sciama, D. W. 1972, *MNRAS*, 157, 335
- Ibata, R. A., Gilmore, G., & Irwin, M. J. 1994, *Nature*, 370, 194
- Israelian, G., García López, R. J., & Rebolo, R. 1998, *ApJ*, 507, 805
- Jacq, T., Baudry, A., Walmsley, C. M., & Caselli, P. 1999, *A&A*, 347, 957
- Jiang, I.-G., & Binney, J. 1999, *MNRAS*, 303, L7
- Jiang, I., Dutta, S., & Binney, J. 1998, *Galactic Halos*, 136, 382
- Kaelble, A., de Boer, K. S., & Grewing, M. 1985, *A&A*, 143, 408
- Kahn, F. D., & Woltjer, L. 1959, *ApJ*, 130, 705
- Kahn, F.D & Brett, L. 1993, *MNRAS*, 263, 37
- Kennicutt, R. C., Jr. 1983, *ApJ*, 272, 54
- Kennicutt, R. C., Jr., Tamblyn, P., & Congdon, C. E. 1994, *ApJ*, 435, 22
- Konz, C., Brüns, C., & Birk, G. T. 2002, *A&A*, 391, 713
- Kotoneva, E., Flynn, C., Chiappini, C., & Matteucci, F. 2002, *MNRAS*, 336, 879
- Kruk, J. W., et al. 2002, *ApJS*, 140, 19
- Kudoh, T., & Basu, S. 2004, *A&A*, 423, 183
- Kuijken, K., & Gilmore, G. 1989, *MNRAS*, 239, 605
- Lacey, C., & Cole, S. 1993, *MNRAS*, 262, 627

- Lehner, N., Gry, C., Sembach, K. R., Hébrard, G., Chayer, P., Moos, H. W., Howk, J. C., & Désert, J.-M. 2002, *ApJS*, 140, 81
- Lemoine, M., et al. 2002, *ApJS*, 140, 67
- Lepine, J. R. D., & Duvert, G. 1994, *A&A*, 286, 60
- Lin, D. N. C., & Lynden-Bell, D. 1977, *MNRAS*, 181, 59
- Lockman, F. J. 2003, *ApJ*, 591, L33
- Lockman, F. J., Benjamin, R. A., Heroux, A. J., & Langston, G. I. 2008, *ApJ*, 679, L21
- López-Corredoira, M., Beckman, J. E., & Casuso, E. 1999, *A&A*, 351, 920
- López-Corredoira, M., Betancort-Rijo, J., & Beckman, J. E. 2002, *A&A*, 386, 169
- López-Corredoira, M., Betancort-Rijo, J., & Beckman, J. E. 2008, *Pathways Through an Eclectic Universe*, 390, 359
- Lubowich, D. A., Pasachoff, J. M., Galloway, R. P., Balonek, T. J., Tremonti, C., Millar, T., & Roberts, H. 2000, *The Light Elements and their Evolution*, 198, 167
- Maller, A. H., & Bullock, J. S. 2004, *MNRAS*, 355, 694
- Meyer, D. M., Jura, M., Hawkins, I., & Cardelli, J. A. 1994, *ApJ*, 437, L59
- Meusinger, H., Stecklum, B., & Reimann, H.-G. 1991, *A&A*, 245, 57
- Miller, E. D., & Bregman, J. N. 2005, *Extra-Planar Gas*, 331, 261
- Miller, E. D., Bregman, J. N., & Wakker, B. P. 2009, *ApJ*, 692, 470
- Mirabel, I. F. 1981, *Revista Mexicana de Astronomia y Astrofisica*, vol. 6, 6, 245
- Mirabel, I. F. 1981, *ApJ*, 250, 528
- Moos, H. W., et al. 2002, *ApJS*, 140, 3
- Morras, R., Bajaja, E., & Arnal, E. M. 1998, *A&A*, 334, 659
- Muller, C. A., Oort, J. H., & Raimond, E. 1963, *Academie des Sciences Paris Comptes Rendus*, 257, 1661
- Navarro, J. F., Frenk, C. S., & White, S. D. M. 1995, *MNRAS*, 275, 56
- Nissen, P. E., Gustafsson, B., Edvardsson, B., & Gilmore, G. 1994, *A&A*, 285, 440
- Oort, J. H. 1966, *Bull. Astron. Inst. Netherlands*, 18, 421
- Ostriker, E. C., & Binney, J. J. 1989, *MNRAS*, 237, 785
- Peek, J. E. G., Putman, M. E., McKee, C. F., Heiles, C., & Stanimirović, S. 2007, *ApJ*, 656, 907
- Peek, J. E. G., Putman, M. E., & Sommer-Larsen, J. 2008, *ApJ*, 674, 227
- Phookun, B., Vogel, S. N., & Mundy, L. G. 1993, *ApJ*, 418, 113
- Polehampton, E. T., Baluteau, J.-P., Ceccarelli, C., Swinyard, B. M., & Caux, E. 2002, *A&A*, 388, L44
- Putman, M. E., et al. 2002, *AJ*, 123, 873

- Putman, M. E., Thom, C., Gibson, B. K., & Staveley-Smith, L. 2004, *ApJ*, 603, L77
- Quilis, V., & Moore, B. 2001, *ApJ*, 555, L95
- Rana, N. C., & Wilkinson, D. A. 1986, *MNRAS*, 218, 497
- Rand, R. J., & Stone, J. M. 1996, *AJ*, 111, 190
- Rebolo, R., García López, R. J., & Pérez de Taoro, M. R. 1995, *The Light Element Abundances*, 420
- Relaño, M., Beckman, J. E., Daigle, O., & Carignan, C. 2007, *A&A*, 467, 1117
- Reshetnikov, V., & Combes, F. 1998, *A&A*, 337, 9
- Rocha-Pinto, H. J., & Maciel, W. J. 1996, *MNRAS*, 279, 447
- Rocha-Pinto, H. J., Maciel, W. J., Scalo, J., & Flynn, C. 2000, *A&A*, 358, 850
- Ryden, B. S., & Gunn, J. E. 1987, *Dark matter in the universe*, 117, 364
- Sancisi, R. 1983, *Internal Kinematics and Dynamics of Galaxies*, 100, 55
- Sancisi, R., Fraternali, F., Oosterloo, T., & van der Hulst, T. 2008, *A&A Rev.*, 15, 189
- Sanchez-Saavedra, M. L., Battaner, E., & Florido, E. 1990, *MNRAS*, 246, 458
- Shapiro, P. R., & Field, G. B. 1976, *ApJ*, 205, 762
- Schombert, J. M., Pildis, R. A., Eder, J. A., & Oemler, A. J. 1995, *AJ*, 110, 2067
- Stothers, R. 1972, *ApJ*, 175, 431
- Simon, J. D., Blitz, L., Cole, A. A., Weinberg, M. D., & Cohen, M. 2006, *ApJ*, 640, 270
- Sommer-Larsen, J. 2006, *ApJ*, 644, L1
- Sonneborn, G., et al. 2002, *ApJS*, 140, 51
- Thilker, D. A., Braun, R., & Westmeier, T. 2005, *Extra-Planar Gas*, 331, 113
- Tinsley, B. M. 1977, *ApJ*, 211, 621
- Tremaine, S. D. 1976, *ApJ*, 203, 72
- Tripp, T. M., et al. 2003, *AJ*, 125, 3122
- Thom, C., Peek, J. E. G., Putman, M. E., Heiles, C., Peek, K. M. G., & Wilhelm, R. 2008, *ApJ*, 684, 364
- Twarog, B. A. 1986, *Instrumentation and Research Programmes for Small Telescopes*, 118, 135
- van Woerden, H., Wakker, B. P., Schwarz, U. J., & de Boer, K. S. 2004, *High Velocity Clouds*, 312,
- Wada, K. 2001, *ApJ*, 559, L41
- Wada, K., & Norman, C. A. 2001, *ApJ*, 547, 172
- Wakker, B. P., & van Woerden, H. 1991, *A&A*, 250, 509
- Wakker, B., van Woerden, H., de Boer, K. S., & Kalberla, P. 1998, *ApJ*, 493, 762

-
- Wakker, B. P., van Woerden, H., & Gibson, B. K. 1999, *Stromlo Workshop on High-Velocity Clouds*, 166, 311
- Wakker, B. P. 2004, *High Velocity Clouds*, 312, 25
- Walter, F., Brinks, E., de Blok, W. J. G., Thornley, M. D., & Kennicutt, R. C. 2005, *ASP Conf. Proc. 331, Extra-Planar Gas*, ed. R. Braun (San Francisco: ASP), 269
- Walter, F., et al. 2007, *ApJ*, 661, 102
- Walter, F., Brinks, E., de Blok, W. J. G., Bigiel, F., Kennicutt, R. C., Thornley, M. D., & Leroy, A. 2008, *AJ*, 136, 2563
- Westmeier, T., Braun, R., & Thilker, D. 2005, *A&A*, 436, 101
- Westmeier, T., & Koribalski, B. S. 2008, *MNRAS*, 388, L29
- Westmeier, T., Brüns, C., & Kerp, J. 2008, *MNRAS*, 390, 1691
- White, S. D. M., & Frenk, C. S. 1991, *ApJ*, 379, 52
- Wood, B. E., Müller, H.-R., Zank, G. P., & Linsky, J. L. 2002, *ApJ*, 574, 412
- Wolfire, M. G., Hollenbach, D., McKee, C. F., Tielens, A. G. G. M., & Bakes, E. L. O. 1995, *ApJ*, 443, 152